

HIGH RESOLUTION X-RAY SPECTROSCOPY OF FOUR NON-MAGNETIC
CATAclySMIC VARIABLES USING XMM-NEWTON AND CHANDRA
OBSERVATORY DATA

A THESIS SUBMITTED TO
THE GRADUATE SCHOOL OF NATURAL AND APPLIED SCIENCES
OF
MIDDLE EAST TECHNICAL UNIVERSITY

BY

ÇİĞDEM GAMSIZKAN

IN PARTIAL FULFILLMENT OF THE REQUIREMENTS
FOR
THE DEGREE OF DOCTOR OF PHILOSOPHY
IN
PHYSICS

SEPTEMBER 2019

Approval of the thesis:

**HIGH RESOLUTION X-RAY SPECTROSCOPY OF FOUR
NON-MAGNETIC CATAclysmic VARIABLES USING XMM-NEWTON
AND CHANDRA OBSERVATORY DATA**

submitted by **ÇİĞDEM GAMSIZKAN** in partial fulfillment of the requirements for
the degree of **Doctor of Philosophy in Physics Department, Middle East Techni-
cal University** by,

Prof. Dr. Halil Kalıpçılar
Dean, Graduate School of **Natural and Applied Sciences**

Prof. Dr. Altuğ Özpineci
Head of Department, **Physics**

Prof. Dr. Altuğ Özpineci
Supervisor, **Physics, METU**

Prof. Dr. Sıtkı Çağdaş İnam
Co-supervisor, **E. and E. Eng., Başkent University**

Examining Committee Members:

Prof. Dr. Tansel Ak
Astronomy and Space Sciences, İstanbul University

Prof. Dr. Altuğ Özpineci
Physics, METU

Assoc. Prof. Dr. Sinan Kaan Yerli
Physics, METU

Assoc. Prof. Dr. Atakan Gürkan
Physics, METU

Assoc. Prof. Dr. Mesut Yılmaz
Astronomy and Space Sciences, Ankara University

Date: 06.09.2019

I hereby declare that all information in this document has been obtained and presented in accordance with academic rules and ethical conduct. I also declare that, as required by these rules and conduct, I have fully cited and referenced all material and results that are not original to this work.

Name, Surname: iđdem Gamsızkan

Signature :

ABSTRACT

HIGH RESOLUTION X-RAY SPECTROSCOPY OF FOUR NON-MAGNETIC CATAclySMIC VARIABLES USING XMM-NEWTON AND CHANDRA OBSERVATORY DATA

Gamsızkan, Çiğdem

Ph.D., Department of Physics

Supervisor: Prof. Dr. Altuğ Özpineci

Co-Supervisor: Prof. Dr. Sıtkı Çağdaş İnam

September 2019, 89 pages

This thesis presents an analysis of high-resolution X-ray spectra of four non-magnetic cataclysmic variables based on archival data of *XMM-Newton* and *Chandra* observatories. The analysis focuses on the classical novae data in outburst; V2491 Cyg, V4743 Sgr and V407 Lupi taken by *XMM-Newton* RGS, and KT Eridani taken by *Chandra* HRC-S+LETG. All these novae have super-soft-source (SSS) type spectra with the broad and blueshifted absorption lines. As an alternative to the static or expanding stellar atmospheric models used in the modeling of the X-ray data, composite models including warm and hot absorbers are constructed and investigated in detail. The continuum is modeled by a blackbody emission, besides a collisionally ionized emission model for V2491 Cyg. The presence of different components of absorption from a warm photoionized and a hot collisionally ionized plasma is detected and included in the models. The absorption lines corresponding to the interstellar medium and dust absorption are modeled in all four sources with slightly different column densities and elemental abundances. The difference in the absorbers, in their column densities, ionizations and temperatures indicate the inhomogeneities in the ejecta and

complex morphology of the outflow. We show that the variations within the absorbers in addition to the changes in the central emitting source cause the variations on time scales of hours in the X-ray count rates. The composite model with the absorber components gives a good description of the SSS spectra of all four sources and indicates the necessity of the consideration of the absorptions from the fast-moving and highly ionized plasma in these cases.

Keywords: V2491 Cyg, V4743 Sgr, KT Eridani, V407 Lupi, cataclysmic variables, novae, X-ray spectra

ÖZ

XMM-NEWTON VE CHANDRA GÖZLEMEVLERİNİN VERİLERİNE DAYALI DÖRT AMANYETİK KATAKLİSMİK DEĞİŞKENİN YÜKSEK ÇÖZÜNÜRLÜKLÜ X-IŞINI SPEKTROSKOPİLERİ

Gamsızkan, Çiğdem

Doktora, Fizik Bölümü

Tez Yöneticisi: Prof. Dr. Altuğ Özpineci

Ortak Tez Yöneticisi: Prof. Dr. Sıtkı Çağdaş İnam

Eylül 2019 , 89 sayfa

Bu tez, *XMM-Newton* ve *Chandra* gözlemevlerinin arşiv verilerine dayanarak dört amanyetik kataklismik değişkenin yüksek çözünürlüklü X-ışını tayflarının bir analizini sunmaktadır. Analiz, patlamadaki klasik nova verilerine odaklanmaktadır; *XMM-Newton* RGS tarafından alınan V2491 Cyg, V4743 Sgr ve V407 Lupi verileri ve *Chandra* HRC-S+LETG tarafından alınan KT Eridani verileri. Bütün bu novalar, geniş ve maviye kayan soğurma çizgileri bulunan süper yumuşak kaynaklı (SSS) tip tayfa sahiptir. X-ışını verilerinin modellenmesinde kullanılan statik veya genişleyen yıldız atmosferi modellerine bir alternatif olarak, ılık ve sıcak emiciler içeren bileşik modeller oluşturulmuş ve detaylı olarak incelenmiştir. Sürey salım, V2491 Cyg için çarpışmalı iyonize salım modelinin eklenmesinin yanı sıra bir kara cisim salımı ile modellenmiştir. Ilık fotoiyonize ve sıcak çarpışmalı iyonize plazmadan kaynaklanan farklı soğurma bileşenlerinin varlığı tespit edilmiş ve modellere dahil edilmiştir. Yıldızlararası madde ve toz soğurmalarına karşılık gelen soğurma çizgileri dört kaynağın hepsinde biraz farklı yoğunluklar ve element bolluğu ile birlikte modellenmiştir.

Soğurma bileşenlerindeki, onların yoğunluklarındaki, iyonlaşma ve sıcaklıklarındaki farklar, atılan maddelerin homojen olmadıklarını ve madde akışının karmaşık morfolojisini gösterir. Merkezi salım kaynağındaki değişikliklere ek olarak soğurma bileşenlerindeki değişikliklerin, X-ışını sayım oranlarındaki saatlik değişimlere neden olduğu gösterilmiştir. Soğurma bileşenlerine sahip olan bileşik model, dört kaynağın hepsinin SSS tayfının iyi bir tanımını verir ve hızlı hareket eden ve yüksek oranda iyonize edilmiş plazmadan gelen soğurmaların bu durumlarda dikkate alınması gerektiğini belirtir.

Anahtar Kelimeler: V2491 Cyg, V4743 Sgr, KT Eridani, V407 Lupi, kataklismik değişkenler, novalar, X-ışını spektroskopisi

To my family, each and everyone.

ACKNOWLEDGMENTS

I wish to express my gratitude to Prof. Dr. Şölen Balman for her guidance, advice, criticism, encouragements and understanding throughout the research. Additionally, I would like to thank Prof. Dr. Altuğ Özpineci for being my supervisor and giving me a chance to finish this thesis. But most importantly, this thesis would not exist without the help and support of Prof. Dr. Sıtkı Çağdaş İnam, my deepest gratitude is for him.

I would also like to thank every family members for their implacable support, especially to my husband, Halil Gamsızkan, for being by my side throughout my journey.

This work was supported by The Scientific and Technological Research Council of Turkey, TÜBİTAK through project 114F351.

TABLE OF CONTENTS

ABSTRACT	v
ÖZ	vii
ACKNOWLEDGMENTS	x
TABLE OF CONTENTS	xi
LIST OF TABLES	xiv
LIST OF FIGURES	xvi
CHAPTERS	
1 INTRODUCTION	1
1.1 Motivation and Problem Definition	1
1.2 Proposed Methods and Models	2
1.3 Contributions and Novelties	3
1.4 The Outline of the Thesis	3
2 OVERVIEW OF CATAclySMIC VARIABLES	5
2.1 Mass transfer	7
2.2 Classification and Eruptive Behavior of CVs	8
2.2.1 Classical Novae	8
2.2.2 Dwarf Novae	9
3 DATA ANALYSIS	11

3.1	<i>XMM-Newton</i> Observatory	11
3.2	Chandra	13
3.3	SPEX	14
3.4	Emission models	15
3.5	Absorber models	16
4	V2491 CYG	19
4.1	Observations and the data	20
4.2	Analysis and Results	21
4.3	Discussion	25
5	V4743 SGR	35
5.1	Observations and the data	36
5.2	Analysis and Results	37
5.3	Discussion	39
6	KT ERIDANI	49
6.1	Observations and data	50
6.2	Analysis and Results	51
6.3	Discussion	58
7	V407 LUPI	63
7.1	Observations and the data	64
7.2	Analysis and Results	65
7.3	Discussion	66
8	SUMMARY AND COMMENTS	71
	REFERENCES	77

CURRICULUM VITAE 89

LIST OF TABLES

TABLES

Table 4.1	Elemental abundances obtained with a composite model includes two hot absorber in the first column and with a composite model includes two hot and one warm absorber in the second column	29
Table 4.2	RGS best fit spectral parameters of the four time intervals derived from the composite model constructed with two Hot absorber models. . . .	31
Table 4.3	RGS best fit spectral parameters of the four time intervals derived from the composite model constructed with two Hot absorber and one warm absorber models.	32
Table 5.1	Best fit elemental abundances of the V4743 Sgr given in solar units. The below spectra are given in ascending time order.	40
Table 5.2	Spectral parameters obtained from best fitted composite model of V4743 Sgr RGS spectra from the blue region. The errors are calculated with 90% confidence level for one degree of freedom. The below spectra are given in ascending time order.	46
Table 5.3	Spectral parameters obtained from best fitted composite model of V4743 Sgr RGS spectra from the red, green and yellow region. The errors are calculated with 90% confidence level for one degree of freedom. The below spectra are given in ascending time order.	47
Table 6.1	<i>Chandra</i> HRC-S+LETG observations of KT Eridani	50

Table 6.2 *Chandra* HRC-S+LETG KT Eri best model fit parameters. The errors are calculated with %90 confidence level for one degree of freedom. 55

Table 6.3 Elemental abundances obtained with a composite model includes one hot and one warm absorber. The values are given relative to the solar abundances that are explained in the text. 58

Table 7.1 *XMM-Newton* RGS best fit parameters of V407 Lupi are in the left. Elemental abundances obtained with a composite model includes two hot absorber are on the right. The abundances are given according to the solar abundances. The errors are calculated with %90 confidence level for one degree of freedom. 67

LIST OF FIGURES

FIGURES

- Figure 2.1 The theoretical model of cataclysmic variable. G is the center of mass. (a) accretion disk and the bright spot where the material flow hits, nonmagnetic system; (b) mass transfer through magnetic field lines on to the magnetic poles of the WD, magnetic system. Reprinted from [1]. 6
- Figure 2.2 The Roche lobe representation of a double star. The larger lobe includes the more massive star while the smaller lobe includes lighter mass star. In the case of CVs the companion will fill its Roche lobe and the WD will be in the center of its with accretion disk. The point where the lobes are connected represents the L_1 point. Reprinted from [1]. . . 7
- Figure 4.1 The light curves of V2491 Cyg obtained from *XMM-Newton* RGS1 data 39.9 days after outburst, on the left, and 49.6 days after outburst, on the right. The variation in the first observation count rate and corresponding time intervals that are taken into account for the analysis can be seen on the left. The corresponding time intervals labelled as 1, 2 and 3 as discussed in the text. 21
- Figure 4.2 V2491 Cyg combined RGS1 and RGS2 flux spectrum in the wavelength range 7-14.4Å. The spectrum is of the era3 is on the left and the spectrum of the second observation is on the right. The model spectrum is represented by the red line and is composed of the plasma emission *cie* and the cold *hot* absorption model for the ISM. An additive blackbody model is used for the continuum emission for the second observation. 24

Figure 4.3 The RGS flux spectrum of V2491 Cyg era1 on the top and era2 on the bottom panel. The fitted composite model is represented by the red line. It is constructed by two *hot* models. Several identified blueshifted absorption lines are given in the plots. 26

Figure 4.4 The RGS flux spectrum of V2491 Cyg era3 on the top and second observation on the bottom panel. The composite model is constructed with two hot absorption models. 27

Figure 5.1 The left panel shows light curve (LC) of V4743 Sgr XMM-Newton RGS1 data averaged with 100s for clarity. The spectra used in the analysis are obtained from the indicated regions that are shown in the right panel. The first region on the left shown in blue is considered as the time interval where the periodic variability is clearly visible. We obtained consecutive six spectra from this region where the crests are labeled as p1, p2, p3 and troughs as b1, b2, b3 respectively. The second region from the left in red is considered as low region where the variability is not well defined as in first region. We divided the region into three time intervals, two troughs and one peak, and obtained three spectra b11, p1, b12 . The second one from the right in green is labeled as valley. Here, the periodicity subdues and the prominence of the peaks disappears. The last region in yellow considered as high region and two spectra are obtained called as high-peak (hp) and high-bottom (hb) respectively. 38

Figure 5.2 RGS1 flux spectra of V4743 Sgr fitted with the composite model. From top to bottom panel, plots show b1, b2 and b3 spectra respectively as indicated in the LC. The red line shows the best fitted composite model. 41

Figure 5.3 RGS1 flux spectra of V4743 Sgr fitted with the composite model. From top to bottom panel, plots show p1, p2 and p3 spectra respectively as indicated in the LC. 42

Figure 5.4	RGS1 flux spectra of V4743 Sgr low region fitted with the composite model. Top panels show the plots bl1 on top, pl in the middle and bl2 spectra at the bottom.	43
Figure 5.5	RGS1 flux spectra of V4743 Sgr valley and high region fitted with the composite model. The top panel shows the valley while the high-peak is in the middle and high-bottom is at the bottom.	44
Figure 6.1	The background subtracted light curves of KT Eri on days 71.3, 79.3, 84.6 and 158.8. The data are measured with HRC-S camera as zero-order and are binned with 50 s in all observations. The x-axis shows the on time of the detector.	52
Figure 6.2	KT Eri <i>Chandra</i> HRC-S+LETG spectra of 71.3, 79.3, 84.6 and 158.8 days after the outburst from top to bottom respectively. All panels show the flux spectrum between 19Å and 60Å in the units of counts $s^{-1} m^{-2} Å^{-1}$. The flux in day 71.3 is lower than the other three observations, hence the flux range is different than the rest.	53
Figure 6.3	The HRC-S+LETG flux spectra of KT Eri on 71.3 and 79.3 days. The best fit model is indicated with the red line.	56
Figure 6.4	The HRC-S+LETG flux spectra of KT Eri on 84.6 and 158.8 days. The best fit model is indicated with the red line.	57
Figure 7.1	<i>XMM-Newton</i> RGS1 background subtracted light curve of V407 Lupi 168 days after the outburst. The time bin size is 50 s.	65
Figure 7.2	V407 Lupi <i>XMM-Newton</i> RGS high-resolution spectrum 168 days after the outburst. The red line show the best fitted composite model. The bottom panel shows the deviations from the model.	68

CHAPTER 1

INTRODUCTION

1.1 Motivation and Problem Definition

This thesis is about high-resolution X-ray spectroscopy of cataclysmic variables (CVs) which is a class of X-ray binaries transferring mass from a donor star to a white dwarf (WD), a compact star accretor. The most striking characteristics of the CVs are their outbursts. The CV outbursts occur as a consequence of the hydrogen-rich mass transfer that leads to nuclear explosions on the surface of WD when the ignition conditions are reached. The resulting eruption is ejecting some portion of the matter of the envelope. The outburst is initially observed as an increase in the optical brightness. Then, in the post-nova phase, the observed wavelength of maximum energy goes from larger wavelengths, optical, to shorter wavelengths, X-ray. The source of X-ray emission in cataclysmic variables might be circumstellar matter shocked by the nova wind, nebula ejected in the outburst or the thermal emission of the WD atmosphere. X-ray observations of these sources enable us to improve our understanding of accretion physics; such as its mechanism and interactions with their surroundings. To be able to infer physical parameters, spectral modeling of data can be used. The temperatures and the density of the emitting region, emitting radius or abundances can be determined with the proper modeling of the actual physical processes.

One of the challenges for spectral modeling is the absorption lines. From Super Soft X-ray Sources (SSS) to novae, numerous sources had been observed by ROSAT and BeppoSAX. However, the spectral resolution of the resulting data was low, and physics interpreted from the spectra were limited. By introducing high-resolution X-ray spectra with observatories such as *XMM-Newton* and *Chandra*, a rich array

of absorption features have been revealed. As a result, high-resolution X-ray spectroscopy can now disclose more detailed information; the properties of the gas flow in the disk, the characteristics of the plasma originating from the wind and ejecta, the intrinsic properties of the interstellar medium along the line of sight with the features of the stellar emission. However, the detailed features of the spectra make it harder to find the correct physical models.

The environment of a nova atmosphere, unlike any low-density plasma, exhibits a significant absorption from excited states that are difficult to identify compared to resonance lines of C, N, O. The strong line absorptions modify continuum emission of the source along with the absorptions from interstellar medium and circumstellar material. In most of the cases, these lines are blueshifted to some extent indicating there is a moving environment that alters the spectrum. Variety in the origin of absorption and its effects on the spectra requires more realistic complex modeling.

1.2 Proposed Methods and Models

The static and expanding stellar atmospheric models can be used to model the continuum emission, emission and absorption lines. They are studied in details in the literature; however, they are insufficient to explain observed complex absorption features in the spectrum [2, 3]. We now know that the interstellar medium absorbs some of the emission coming from the source and modifies the spectrum. Besides, emission or absorption from the plasma originating from wind or ejecta alters the observed spectrum and can explain the blueshifts. Hence, we construct a new approach alternative to stellar atmospheric models. We model the continuum with a simple blackbody emission. We know that a simple blackbody emission is not accurate and cause some overestimation of some parameters. But, it is convenient to construct more complex models, including plasma absorptions with currently available analysis packages. We consider using absorption models of collisionally ionized hot plasma and photoionized warm plasma originating from wind or ejecta upon blackbody model. The effect of the interstellar medium is also included. We aim to show that the observed complex absorption features can be modeled by using these plasma components; hence, consideration of these absorbers are a necessity. For these purposes, we reanalyzed a

selection of archival *XMM-Newton* RGS data of the three classical novae V2491 Cyg, V4743 Sgr and V407 Lupi and *Chandra* HRC-S+LETG data of KT Eridani.

1.3 Contributions and Novelties

Our contributions are as follows:

- We provided an alternative approach to stellar atmospheric models to explain observed X-ray spectra of some cataclysmic variables.
- We showed the necessity of constructing complex models, including absorptions from the wind and ejecta surrounding the source and the interstellar medium.
- We provided complementary results of the *XMM-Newton* RGS data of V2491 Cyg, V4743 Sgr and V407 Lupi.
- The study on V2491 Cyg is published under the title of "*Reanalysis of high-resolution XMM-Newton data of V2491 Cygni using models of collisionally ionized hot absorbers*" in A&A journal.
- We provided a detailed X-ray spectral analysis of *Chandra* HRC-S+LETG data of KT Eridani and some of its physical parameters such as stellar abundances and column densities.

1.4 The Outline of the Thesis

The thesis reports the *XMM-Newton* high-resolution X-ray spectroscopy analysis of V2491 Cyg in Chapter 4, V4743 Sgr in Chapter 5 and V407 Lupi in Chapter 7. *Chandra* observatory analysis of KT Eridani is in Chapter 6. For a better understanding, a brief discussion on the cataclysmic variables and classical novae is given in the following sections of Chapter 2. The properties of the observatories, data production and the details of the data reduction and process are given in Chapter 3. The final section, Chapter 8, covers summary and comments.

CHAPTER 2

OVERVIEW OF CATAclySMIC VARIABLES

Cataclysmic variables (CVs) are considered to be fascinating objects due to their variations that are never repeating themselves, unpredictabilities and chaotic outbursts. CVs are a subclass of variable double star systems with binary separations less than a few solar radii and orbital periods less than half a day [1]. In the canonical model of cataclysmic variables, the more massive main sequence star becomes a giant and creates an envelope surrounding the binary system. The separation between the stars decreases while they orbit inside this common envelope, and the orbital period drops from days to hours. When the envelope dissipates, a compact star, a white dwarf is emerged with a companion, a red giant or in some cases brown dwarf. The system evolves due to loss of angular momentum by a braking wind of the giant star until the companion starts to transfer mass to the WD. At this point, the companion is tidally and rotationally distorted, due to the extreme conditions, into a teardrop shape called Roche lobe [1, 4, 5, 6].

The magnetic field strength of the WD determines how the mass is transferred to its surface. When there is negligible or no magnetic field exists ($B < 1$ MG), the transferred mass builds up an accretion disk around the WD. In this non-magnetic case, the material spiral inwards to the WD surface via the disk. If the magnetic field strength is high, the mass follows the magnetic field lines ($B > 10$ MG) and falls on to the magnetic poles of the WD directly, polar case (see Figure-2.1) [1]. When the magnetic field strength lies between those two ranges, semi-disk forms where the inner disk is disrupted by the magnetic field lines of the WD and the material drops on to the surface via accretion curtains, intermediate polar (IP) case [4].

For the accretion case, the mass transfer rate depends on the viscosity of the material

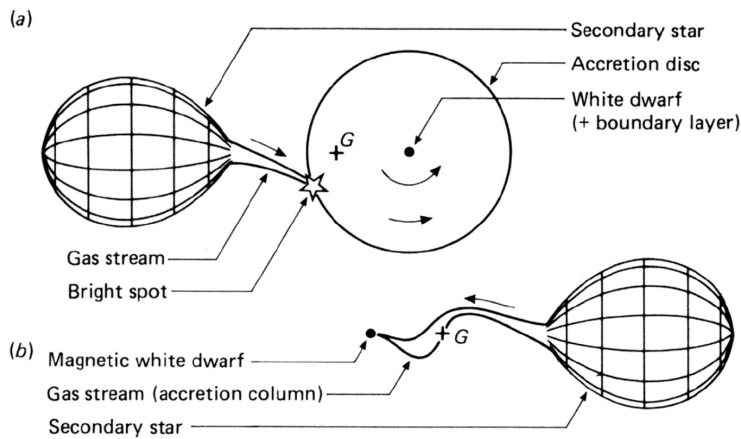


Figure 2.1: The theoretical model of cataclysmic variable. G is the center of mass. (a) accretion disk and the bright spot where the material flow hits, nonmagnetic system; (b) mass transfer through magnetic field lines on to the magnetic poles of the WD, magnetic system. Reprinted from [1].

affected by the mass transfer from the companion to the outer edge of the disk. If the mass transfer rate is high, the disk will be in high viscosity but stable state and hot. There will be no large-amplitude outbursts, and their spectra will lack the common emission lines of most typical CVs. Such systems are called *Nova-like*. If the mass transfer rate is low, the disk will have low viscosity, be cool and unable to sustain the flow of material provided by the companion. The material will accumulate in the disk heats it and turns the disk into the high-viscosity state. As a result, the material will be flushed on the WD surface rapidly and caused the quasi-regular outburst known as a *dwarf nova*. *Dwarf nova* is the most common type of eruption seen in CVs. The increase in brightness by two orders of magnitudes occurs less than a half a day. Then, it fades slowly within one or two weeks [7, 5].

The mass transfer of the material to the surface of the WD in any case of CV creates a layer of hydrogen-rich material. If the proper conditions for the ignition are provided there will be a violent explosion of this material, thermonuclear runaway, that is called *classical nova*. All CVs are considered to undergo a number of classical novae phases, with recurrence timescales varying from hundreds to thousands of years. For some

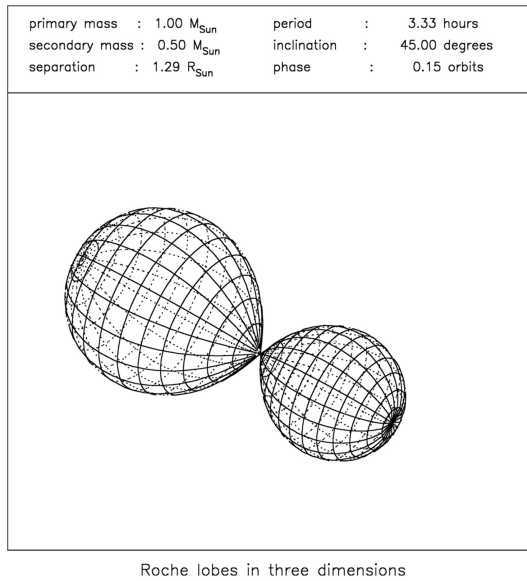


Figure 2.2: The Roche lobe representation of a double star. The larger lobe includes the more massive star while the smaller lobe includes lighter mass star. In the case of CVs the companion will fill its Roche lobe and the WD will be in the center of its with accretion disk. The point where the lobes are connected represents the L_1 point. Reprinted from [1].

CVs, these recurrence times can be as short as a few decades, and these specially observed cases are called a *recurrent nova* [7, 5].

In the following sections, brief information on the mass transfer, the types of cataclysmic variables, their outburst mechanisms and the observations in X-ray band will be discussed.

2.1 Mass transfer

In close star systems as in the case of cataclysmic variables, tidal interactions become important beyond star's mutual gravitational attraction and centrifugal force seen in a frame rotating with orbital angular velocity. These tidal effects can lead to circularization of the orbits and increase their rotation speeds such that they are synchronous with the orbital motion. Additionally, low mass companion is distorted by the gravity of compact star such that its outer layers are pulled out. At a critical distance point

gravitational attraction towards the WD becomes greater than the star itself, thus, material closest to the WD flows between the two stars [1, 4].

The stars can be represented as point masses and the total force on the test particle in close binary system can be represented by the total potential that is known as the *Roche potential*. The points where the total force on the test particle are zero is called *Lagrangian points* and the one between the center line of two stars, inner Lagrangian point L_1 , is the critical point. The potential surface through L_1 resembles the shape of a dumbbell and the two tear shaped lobes are called the *Roche lobes* (see Figure-2.2). If there is no disturbance the material at the point L_1 will be in equilibrium. A slightest change in the state will cause the material to flow from one Roche lobe to the other [1, 4].

There are three types of binary systems related to the states of their Roche lobe fillings. If each of the star radii is much smaller than the Roche lobe radius, the binary system is called *detached binaries*. If both of the stars fill their Roche lobes, the system is defined as *contact binary*. The companion of the cataclysmic system fills its Roche lobe while the white dwarf stays well within its Roche lobe radius. Such systems are called *semi-detached binaries*, and here, the accreted mass from the companion to WD does not fall directly on to the WD surface but spirals inwards since the matter has non-zero angular momentum relative to WD. Due to dissipation, the matter forms a disk and the accreted material moves within the disk. While the incoming material spiral inwards to the WD surface, a small amount of material moves outwards to the larger radius through the disk to conserve angular momentum. The disk can grow until 90% of the WD Roche lobe radius where the tidal forces of the companion set the limits [1, 4].

2.2 Classification and Eruptive Behavior of CVs

2.2.1 Classical Novae

Classical nova explosions are thermonuclear explosions. If the WD mass is less than $0.5M_{\odot}$, it is mostly composed of helium. If the mass is between $(0.5-1.2)M_{\odot}$, it is a

mixture of carbon and oxygen. The WDs having masses greater than $1M_{\odot}$ can have oxygen-neon cores. Matter accreted from the companion is mostly hydrogen, and this material accumulates gradually on the WD surface. As the material builds up, the density of the layer increases; and the electrons in the ionized hydrogen become degenerate. Except for the layer near the surface, the dominant pressure becomes the pressure of the degenerate electrons. The temperature of the layer increases as the layer becomes thicker and allows hydrogen fusion to occur. The pressure is independent of the temperature of the degenerate gas, hence burning causes a thermal runaway instead of a moderate thermal expansion, and there will be an explosive ignition of hydrogen burning. The strength of the explosion is high enough to eject the hydrogen layer. The remaining WD is free of hydrogen. The whole process repeats itself on a time scale of around 10,000 to 100,000 years. In recurrent novae, the timescales become decades or centuries [7, 5, 6].

Novae show similar behaviors, but they have different rise and decay rates. The term that describes the decay rate is t_3 . It is the time interval required for the visual brightness to drop by 3 magnitudes from its maximum observed value. For a fast nova, t_3 may be as fast as a few days, and for a slower one, it can take several months. In some cases, the mass is transferred too fast. The accreting layer is compressed and heated. It prevents the onset of degeneracy and ejection of outer layers. Therefore, it causes an increase in the WD mass over the critical Chandrasekhar mass. If the WD mass passes this critical limit, a Type Ia supernova explosion is triggered. In general, successive nova explosions are assumed to cause a decrease in the WD mass hence prevents the trigger of a supernova explosion [7, 5].

The post-nova of a CV settles down with a high mass-transfer rate. The systems seem like a post-nova of a CV not observed to have outburst are called nova-like variables.

2.2.2 Dwarf Novae

The dwarf nova outbursts are considered to be much simpler explosions and the source for these explosions is gravitational field of the WD. However, the instabilities that lead to the outburst are complex, namely the instabilities in the accretion disk. In the accretion disk mass accumulates on the disk and when the critical density

is reached, accumulated mass moves rapidly on to the white dwarf releasing significant amount of energy causing the outbursts. These resulted in semi-regular outbursts with various shapes, durations and magnitudes. The recurrence timescale can range between weeks to years and the amplitudes can change between 4-5 magnitudes.

There are two subclasses of dwarf novae. The first one is the Z Camelopardalis (*Z Cam*) stars that alternate between normal outbursts to inactive states. The periods of inactivity are called as 'standstills', during when brightness of the star remains static at the one third of the maximum brightness value. The timescales for these inactive states may be many months and their durations vary. *Z Cam* stars in standstills resemble the nova-like systems with lower luminosity values.

The second subclass is the SU Ursae Majoris *SU UMa* stars. These stars undergo the super outbursts that last longer than the regular outbursts and have larger amplitudes. In these cases, in every outburst cycle, the disk is grown in size. There is a resonant radius where the orbital frequencies of the particles are third times the orbital period. When the disk radius reaches the resonant radius, the tidal forces are dominant on the disk so that the disk precesses. The eccentric disk can then lose enough angular momentum through spreading out the excess mass and shrink back to a small symmetrical disk. Thus the super-outbursts occur. The orbital light curve during the super outbursts is characterized by superhumps that are synchronized with the orbital phase. It is believed to be seen due to the asymmetry in the disk structure [1, 4].

CHAPTER 3

DATA ANALYSIS

We work on astronomical spectroscopy in the X-ray band. X-ray wavelengths generally range between 0.025\AA and 100\AA . Soft X-rays cover 5\AA to 100\AA band, and hard X-rays range between 0.025\AA and 5\AA . The absorption probability of high energy photons is very high. Normal refractive or reflective optical techniques are hard to use in the observations; hence, special instruments are designed. Besides, the Earth's atmosphere is opaque to the short wavelengths ($<3000\text{\AA}$). The observations should be carried out from outer space. For these purposes, specially designed observatories such as *XMM-Newton* operated by European Space Agency (ESA) and *Chandra* operated by National Aeronautics and Space Administration (NASA) are built.

In this chapter, we focus on data analysis. We briefly discuss the general properties of the observatories *XMM-Newton* and *Chandra*, the data processes and the models that are used. The source and the results will be discussed in the following chapters.

3.1 *XMM-Newton* Observatory

The *XMM-Newton* Observatory is operated by ESA for the purpose of obtaining the high sensitivity and high resolution in X-ray observations¹. The observatory consists of three telescopes and three instruments in operation [8]. European Photon Imaging Camera (EPIC) is at the prime focus of all telescopes, Reflecting Grating Spectrometer (RGS) are on two of the three telescopes. The third telescope is for the optical/UV observations with Optical Monitor (OM) [9].

Three EPIC cameras are designed for imaging and spectroscopy to perform in the

¹ <http://sci.esa.int/xmm-newton/>

energy range between 0.15 and 15 keV. Metal-oxide semiconductor (MOS) CCDs are used in two of them [10] and Pn CCDs on the last one [11]. The Reflecting Grating Spectrometers, RGS1 and RGS2, are located behind the two telescopes with their associated cameras [12]. The energy range for the RGS is between 0.33-2.5 keV. In the cameras, eight of nine MOS CCDs, arranged in a strip, record the coming dispersed photons. The ninth CCD is closest to the optical telescope and generally used for the determination of the background. Each spectrometer has a failed chip causing a gap in the observed spectra. Fortunately, the missing spectral regions are different for RGS1 and RGS2. The lost information can be obtained from the spectra of the other spectrometer. The most common approach is to use the combination of each RGS1 and RGS2 spectra. Again this approach allow users also to fill the gaps due to bad pixels, the spectral bins contain no information [13].

XMM-Newton provides Science Analysis Software (SAS) to work on raw data, generate RGS event files and extract the spectra². For the analysis, we used versions 14.0.0 in MacOS and 17.0.0 in Linux based virtual machine with their latest calibration files available on the time of analysis. The XMM-SAS routine *rgsproc* is used to reprocess the data. Initially, standard filters, source position and wavelength zero point are used to extract source and background count spectra. Then, we made all the necessary data checks to obtain good results. All *XMM-Newton* sources worked in this thesis do not need any correction for the flares or sporadic high background. They were bright during the observations. One can also use *rgsfluxer* to obtain flux spectra of each spectrometer and order.

In the analysis, *rgsproc* allows us to apply any time filters to extract spectra over any given time interval. We applied additional time filters to obtained corresponding time specific spectra, such as in the V2491 Cyg first region case and the V4743 Sgr. For each and every time filtered region, *rgsproc* and *rgsfluxer* routines are re-used to produce appropriate response matrices and flux spectra.

² <https://www.cosmos.esa.int/web/xmm-newton>

3.2 Chandra

The *Chandra* X-ray Observatory is operated by NASA³. The mission aims to improve sensitivity between 0.1 to 10 keV and the spatial resolution along with the spectral resolution in the observations relative to earlier X-ray missions such as *Einstein*. All these improvements allow the study of faint sources even in crowded fields. The observatory contains one high-resolution mirror, two imaging detectors and two sets of transmission gratings [14].

The High Resolution Camera (HRC) [15] and the Advanced CCD Imaging Spectrometer (ACIS) are the two focal plane detectors. The instruments are behind the four iridium coated reflecting surfaces arranged in Wolter type 1 geometry with small reflection angles. The resolution obtained from the mirrors is 0.5 letg. HRC is designed for high-resolution imaging (HRC-I) and fast timing measurements and spectroscopy (HRC-S). The HRC-S energy range is 0.06-10 keV but energy resolution is low. As a result, HRC-S can not resolve overlapped spectral orders. ACIS is used for the simultaneous imaging (ACIS-I) and spectroscopy (ACIS-S) with its two-dimensional array of charged coupled devices. It provides an advantage in the observation of extended objects and can measure the energy of each incoming X-ray so it can resolve higher orders.

The transmission grating optimized for the low energies is LETG [16] and for the high energies is HETG. Either ASIC or HRC can be used with the gratings to record the data. The HRC-S is well suited with LETG while ASIC-S can be used with both LETG and HETG.

All the *Chandra* data can be processed with CIAO software provided by the Chandra X-ray Center (CXC) [17]. We used the software version 4.11 with its most recent calibration package CALDB 4.8.2. The main routine is *chandra-repro* to extract event files, source and background spectra, ancillary response files, and redistribution matrix files. More detailed analysis can be done specific to the observation by following the science analysis threads⁴. The HRC-S+LETG observations provide +1 and -1 order spectra. The spectra can be either analyzed simultaneously or combined by using

³ <http://cxc.harvard.edu>

⁴ <http://cxc.harvard.edu/ciao/>

a *combine-grating-spectra* routine.

3.3 SPEX

SRON (HEA Division, Netherlands Institute for Space Research) produces a software package SPEX optimized for the analysis and interpretation of high-resolution cosmic X-ray spectra [18]. It is specialized for modeling the spectra obtained by current X-ray observatories like *XMM-Newton* and *Chandra*. We used two version of this program version 2.05.04 for the analysis of V2491 Cyg and version 3.03.00 for the all other sources.

SPEX normally work with a specific defined files in the fitting analysis. The resulting count rate spectra and response matrixes obtained from *XMM-Newton* or *Chandra* should be converted to its specific file format, but, fortunately, it can directly work with the fluxed spectra obtained from *XMM-Newton rgsfluxer* if it is specifically produced in the wavelength range 5-38Å with 3400 bins in earlier version and 4-40Å with 3600 bins with the later version. By using *RGS-fluxcombine* routine in the SPEX, one can combined the fluxed spectra of the RGS1, RGS2, first and second order data files and obtained one combined flux spectra compatible with the SPEX. Then, *RGS-fmat* can produce corresponding response matrix for the combined flux spectra. The combination of the RGS1 and RGS2 data files is necessary since as it is explained previously, such combination completes the missing spectral information due to failures in the chips. In addition the combination of the first and second order spectra increases the signal to noise ratio.

One exception to combination in the orders is the case of V4743 Sgr. During the *XMM-Newton* observation of V4743 Sgr the CCD chips are overloaded and the events are piled-up. Due to this pile-up effect the PN and EPIC data were not suitable to used in the analysis. The RGS data in most of the cases are not affected by the pile-up as much as the EPIC and PN data. However, the pile-up effect in the V4743 Sgr observation was moderate and it can be seen in the second order RGS1 and RGS2 spectra. Therefore, we considered to use only first order spectra by assuming the piled-up photons seen in the second order spectra only affects the depth of the absorption lines

in the higher wavelengths insignificantly.

3.4 Emission models

The composite model for spectral analysis based on the continuum emission. The spectra of novae in outburst have a soft X-ray component resembling a blackbody-like stellar continuum emission with complex absorption lines. It originated from the underlying WD. Previously, static and expanding stellar atmospheric models are used for the spectral analysis of X-ray data of these novae. For the investigation of the warm or hot plasma absorbers, we assumed a simple blackbody emission.

Several novae having super-soft-source type spectra contain emission lines. In the case of V2491 Cyg, the emission lines for Mg and Ne between 7-14Å are visible. These emission features can be modeled by considering emission from plasma in collisionally ionized equilibrium. SPEX provides a model *cie* for the collisionally ionized plasma. In the model, the important parameters determining the spectral shape and flux are electron temperature T_e and emission measure Y . The electron temperature is considered to be the plasma temperature, and it determines the resulting spectrum. The emission measure can be simply put as

$$Y = \int n_H n_e V \quad (31)$$

where n_e is the electron density and the n_H is the hydrogen density.

The elemental abundances of the plasma are also important. They determine the emission lines and the overall shape of the continuum emission. In the high-resolution X-ray spectroscopy, ion temperatures and the turbulent velocity can be important. If the plasma is in a non-equilibrium state, the electron temperatures and the ion temperatures are not the same. When the plasma is in equilibrium, the ion temperatures and the electron temperatures are coupled. The turbulent velocity for the analysis of V2491 Cyg is included since it affects the width of the emission lines.

3.5 Absorber models

In spectral analysis, we need to take into account the absorption of photons between the observer and the emitting source. Depending on the dynamics of the plasma absorptions, models can vary. SPEX provides some absorption models based on its atomic database. For each absorption mechanism it offers a dynamical model that is calculating the column densities and their transmission. The main assumption in all the absorption models is that there is no re-emission. It can be considered in this way if the X-ray source sees the absorbing medium with a small solid angle. When we look through such an absorbing medium the transmission can be recalculated as $e^{-\tau(E)}$ with $\tau(E)$ is the optical depth.

In more details, the optical depth can be considered with two parts. The first contribution comes from the the total continuum $\tau_c(\lambda)$ and the second contribution is from the line optical depth. Then, the transmission $T(\lambda)$ of the slab can be given as

$$T(\lambda) = e^{-\tau_c(\lambda) - \tau_l(\lambda)} \quad (32)$$

This basic approach allows a fast computation of the spectrum if the thickness of the slab is considered to be small.

In some cases, absorption line is split into different velocity components. The difference can not be fully resolved in X-ray, so one can use

$$\tau_l(v) = \sum_i \tau_i e^{-(v-v_i)^2/2\sigma_v^2} \quad (33)$$

to define line optical depth. The velocity components can be taken as $v_i = v_0 + i\Delta v$, where v_0 is the average velocity of the blend (a negative value associated with outflow or a blueshift) and Δv is the separation between the velocity components. And, τ_i is taken as

$$\tau_i = K e^{-v_i^2/2\sigma_b^2} \quad (34)$$

with the consideration of the r.m.s. width of the blend σ_b is in general larger than the intrinsic width σ_v of the components. Here, $\sum \tau_i = \tau_0$ is used to define the normalization K. As a result, the total optical depth τ_0 is defined as

$$\tau_0 = 0.106 f N_{20} \lambda / \sigma_{v,100} \quad (35)$$

N_{20} defines the total column density of the ion in units of $10^{20} m^{-2}$, f the oscillator strength. $\sigma_{v,100}$ is the velocity dispersion in units of 100 km/s and λ wavelength should be taken in Å.

Two main absorption models *hot* and *xabs* that can be used to model different ionized intrinsic absorber components in the system. The collisionally ionized (in equilibrium) plasma is modeled with *hot* and photoionized plasma is modeled with *xabs*.

The transmission of a plasma in collisional equilibrium can be estimated by *hot* model with its relative solar abundances. By using a collisional ionization plasma, different ionic column densities can be correlated. This model can be used if the medium has a non-negligible optical depth and a negligible photoionization effects. The parameters defining the model are temperature, hydrogen column density and abundances of the ionized elements. The abundances are actually calculated relative to the standard abundance values that are given by proto-solar abundances of Lodders & Palme (2009) [19]. The model calculates the ionization balance for the given temperature and abundances. Then, it determines all ionic column densities by scaling to the pre-assumed hydrogen column density. The total transmission of the plasma is estimated by using these column densities and by multiplying the transmission of the individual ions. The transmission as described above can be defined by continuum and line opacity. The continuum opacities are taken from [20]. The wavelengths for the ions and line opacities are taken from [21]. The absorption due to neutral gas can also be modeled by *hot* with very low temperatures around 0.5 eV. We used this property to model interstellar absorption along the line of sight.

The *xabs* model can be used when a plasma composed of different ions is located between the ionizing source and the observer. It calculates the warm, photoionized absorption from this plasma. The ionic column densities are correlated through a set of values obtained from a photo ionization code. The *xabs* model assumes only absorption by the ions and no re-emission as discussed earlier. It also includes scattering out of the line-of-sight by the free electrons in the slab. The transmission, $T(\lambda)$, of the slab is given as

$$T(\lambda) = e^{-\tau_c - \tau_l - \tau_e} \quad (36)$$

here τ_e is the electron scattering optical depth. For τ_e the classical Thomson approx-

imation is valid below 10 keV. Similarly, τ_1 is a function of v and σ_v which are free parameters of *xabs*.

The photoionisation model calculates the relative column densities of the ions with two free parameters; the equivalent hydrogen column density N_H of the ionized absorber in units of atoms cm^{-2} and ξ the ionization parameter of the absorber. ξ is defined as $\xi = L/n_g r^2$, where L is the luminosity of the ionizing source, n_g the density of the plasma and r the distance between the slab and the ionizing source and is given in units of erg cm s^{-1} .

To use the *xabs* model in SPEX the ionic column densities of a photoionized slab is needed to be pre-calculated for different values of ξ . For this purposes we used a software called CLOUDY [22] version C08.00 and version C13.00 as expected from SPEX. For a given spectral energy distribution (SED), the code computes the ionic column densities for each ionization parameter ξ . A good determination of the energy distribution is important for each source. The ionization equilibrium is different for a soft irradiating spectrum than a hard irradiating spectrum with the same luminosity.

We calculated the model SED by using the software XSPEC (v12.9.0) [23]. We assumed an ionizing continuum of a blackbody model with temperature 65 eV for the V2491 Cyg, 70 eV for V4743 Sgr, 60 eV for KT Eridani and 50 eV for V407 Lupi. SPEX uses the ionic column densities obtained from CLOUDY in the model analysis and gives the best-fit values for N_H and ξ .

CHAPTER 4

V2491 CYG

On April 10, 2008, a possible nova was spotted [24] on unfiltered CCD frames with visual magnitude 7.7 mag. The source was assigned as a variable star V2491 Cyg [25]. The subsequent studies showed that the optical and infrared spectra of the nova had complex and broad emission lines. The lines had expansion velocities around 3900-6400 km s⁻¹ [26, 27]. It is classified as He/N nova [28, 27, 29] with ONe WD [30], or a possible CO WD [31, 32]. The decline time t_2 , a time required for the visual maximum magnitude to drop by 2 mag, was 4.6 days (4.8 days from the exact maximum [33]). Hence, it is considered as a fast nova similar to V2487 Oph and V838 Her [34].

Extensive analyses in X-ray were carried out on the pre-nova, outburst and post-nova stages of V2491 Cyg [35, 30, 36, 37, 32, 38]. Earlier X-ray observations revealed that it has been seen before outburst and was a persistent X-ray source, that makes it the second fastest nova observed in pre-nova in X-ray after V2487 Oph [35, 34]. The decline time t_3 , 3 mag drop, can not be used since the optical spectrum exhibits a secondary peak around day 15 [33, 39]. Such re-brightening is explained by the highly magnetic characteristic of the source, that creates the debate that V2491 Cyg might be a Polar [39, 40, 38]. Furthermore, non-thermal emission identified in X-rays throughout the outburst and a distinct blackbody-like component with effective temperature 77 eV seen in X-rays (an indication of being Soft IP) at post-nova quiescent phase favors magnetic scenario [39, 40, 38].

The distance to the source is estimated as 10.5 kpc [29] by using the reddening $E(B-V)=0.43$ calculated via OI line ratios [41]. Meanwhile, Munari et. al (2011) estimation was 14 kpc based on the reddening $E(B-V)=0.24$ [33]. A recent distance estimate

is 2.1 ± 1.4 kpc for V2491 Cyg [42]. Additionally, GAIA observations yielded a distance of ~ 6.5 kpc [43] which creates a discrepancy in the results. The mass of the white dwarf is estimated as $(1.30 \pm 0.02)M_{\odot}$ [39]. The prominent characteristics of the V2491 Cyg are that it hosts a massive WD, has high expansion velocities and rapid decline in optical magnitude. When pre-nova detections that imply the source has a high accretion rate also taken into account, V2491 Cyg is argued to be recurrent nova [32, 44].

The interstellar medium (ISM) absorbs some of the radiation coming from the source especially photons with the higher wavelengths. Such absorption affects the observed spectrum hence one should consider the absorbing column density of hydrogen N_H of ISM. Along the line of sight to the source V2491 Cyg, the estimations for the column densities are in the range $N_H = 1.9 - 2.9 \times 10^{21}$ atoms cm^{-2} as indicated in [45, 13] and $N_H = 3.8 \times 10^{21}$ atoms cm^{-2} derived from *Swift* data [32]. One can also use interactive programs such as *nhtot*¹ to calculate the column density of the hydrogen that uses the database from [46]. *nhtot* yields the value $N_H = 4.35 \times 10^{21}$ atoms cm^{-2}

4.1 Observations and the data

The *XMM-Newton* observations form part of the X-ray data on V2491 Cyg. The first observation was done 39.9 days after the outburst on May 20, 2008, and followed by the second observation 9.7 days after on May 30, 2008 (49.9 days after outburst) [30, 36]. We used these two observations in our analysis. We focused on the Reflection Grating Spectrometer (RGS) data to obtain high-resolution spectra. The exposure on the RGS of the first set was 39.2 ks, and the second was 29.8 ks.

The data are processed with XMM-SAS *rgsproc* routine as discussed in Chapter 2. We extract the RGS1-RGS2 first and second order source and background count spectra by using standard spatial and energy filters, then obtained the flux spectra as described in the second chapter between 5-38Å with 3400 bins. For an adequate analysis, all of the RGS1-RGS2 first and second order flux spectra are combined and obtained one flux spectra for further processes. The resultant spectra are binned by

¹ <http://www.swift.ac.uk/analysis/nhtot/>

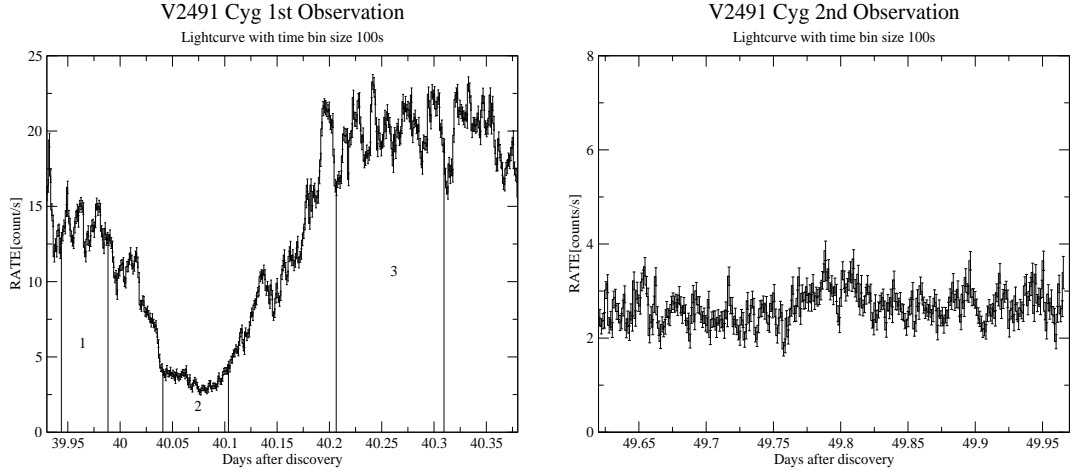


Figure 4.1: The light curves of V2491 Cyg obtained from *XMM-Newton* RGS1 data 39.9 days after outburst, on the left, and 49.6 days after outburst, on the right. The variation in the first observation count rate and corresponding time intervals that are taken into account for the analysis can be seen on the left. The corresponding time intervals labelled as 1, 2 and 3 as discussed in the text.

factor 2 for the correct statistical analysis and to ensure a minimum of 10 counts/bin the range 7-14Å is re-binned by factor 4. The similar data process is followed for both observations.

4.2 Analysis and Results

The light curves (LC) of both observations were obtained from RGS data. The LCs were extracted from the RGS1 first order count rate and binned with 100s, Figure-4.1. It is clear that the count rate is highly variable within a short time scale in the first observation. The prominent feature is the extended dip in count rate after day 40.01 lasting 0.12 days with 3.5 count s^{-1} . Initially, the mean count rate is $13.2 \text{ count s}^{-1}$ and after the dip, it rises to $20.1 \text{ count s}^{-1}$. Such a variation is not observed after day 49.6 that has the mean count rate of $2.6 \text{ counts s}^{-1}$.

The spectrum resembles a bright super soft source SSS. Continuous emission ranges between 7-38Å and the range 15-35Å embedded with very broad and complex ab-

sorption features that profiled an absorbed blackbody. The continuous emission peaks around 24\AA and the prominent absorption lines are around 19\AA and 24.5\AA with an addition around $\sim 23\text{\AA}$ corresponding to OI absorption edge. The first two absorption lines are photospheric origin while the third one, with $1s-2p$ absorption line at 23.5\AA is an interstellar line [13]. Previous, studies showed that most of the lines are blueshifted by -3000 to -3400 km s^{-1} and are broadened by $\sim 1200 \text{ km s}^{-1}$. The range $7-14\text{\AA}$ shows some emission lines of Mg and Ne and are analyzed separately. These main features appeared in both observations while the differences lie in the height of the peak and the other observed absorption lines and/or their depths.

Model descriptions range from static atmospheric models to wind type atmospheric models to fit the observed nova spectrum. In general, static atmospheric models, non-local thermal equilibrium models (NLTE) are enough to explain the complex absorbed spectrum. In the case of the observed blueshifts, one can consider wind type atmospheric models. However, high-resolution X-ray observations bring out more complex absorbed features to be explained. Such complexity cannot be well fitted by the above models hence one should consider different model descriptions. Absorption from ionized plasma that is surrounding the source can cause the observed complex features. The properties of ionized plasma, density, temperature, ionization level and the element abundances can affect the spectrum. We obtained a composite model that includes ionized absorber plasma models to fit both nova data. A software package SPEX optimized for the analysis of the high-resolution X-ray spectra presents two main ionized absorber models *xabs* and *hot* that can be used to interpret intrinsic absorption from the warm photoionized or hot collisionally ionized plasma. Such plasma models are previously used (such as *xabs*) [45]. To compare the different ionized absorber components in the system, we used a similar model approach .

The composite model is constructed by the two continuum models overlapped by the absorber components. Blackbody *bb* is used to fit the main continuum emission. Even if the *bb* is not an efficient model for the continuum as the atmospheric ones, and some of the atmospheric absorption lines will be missing, it still provides a good approximation under these circumstances. For the harder X-ray band where the emission lines appear, an additive collisional equilibrium emission plasma model *cie* is used. There are three groups of absorber components we consider in the analysis. The first

one is the absorption in the line of sight due to ISM between the observer and the source. Cold gas absorption in the ISM can be represented by using the *hot* model in the SPEX software with a very low temperature around 1 eV. Additionally, the absorption due to dust along the line of sight can be included by using the *amol* model. These two components are applied both *bb* and *cie*. However, the last and the main absorber components, that are collisionally hot plasma (*hot* model) and the photoionized warm plasma (*xabs* model) only affect the *bb* component where the complex absorption lines exist. To summarize, the composite model is obtain as [amol x ISM x (cie + (hot₂ x hot₁) x bb)].

Full-time spectral analysis on first observation does not yield an adequate result due to high-variation on the count rate. Therefore, three different time zones were determined and spectral extractions have been made accordingly as discussed in [13, 45]. The time intervals are marked in the left panel of Figure-4.1. The first time interval is labelled as era1 and the dip seen in the LC is labelled as era2. The time interval with the highest mean count rate is labelled as era3. As a result, four spectra are analyzed in total. The complexity of the composite model makes it hard to work with full free parameter space; hence, some of the parameters should be kept fixed during the fitting procedure. Due to the high signal to noise ratio and to fix some of the parameters, the spectral analysis is first applied to the spectrum of era3 for the first observation. A similar procedure is followed for the second observation spectrum.

Initially, hard X-ray wavelengths (7-14 Å) is fitted with [ISM x *cie*] model, where only neon and magnesium contribute to the emission, to follow a similar approach to Pinto et. al [45]. The abundances of these elements and v_{mic} are obtained from the best fits and used in the full model fitting for both observations. The values obtained for era3 are used in the first and second time interval as well. The corresponding flux fits to the two data set is shown in Figure-4.2 and the abundances are listed in the Table-4.2 (and Table-4.3). An additional *bb* model is used in the second observation data fitting. Such inclusion is necessary to account for the long wavelength excess since without it, χ^2_ν of the fit becomes 2.15 which is not acceptable. The second *bb* spectral parameters are different from the main *bb* model that accounts for the stellar emission. Its temperature is 120-131 eV, the normalization is $2-4 \times 10^{15}$ cm² hence the emitting radius is $1.26-1.78 \times 10^7$ cm and the luminosity is 6×10^{35} erg s⁻¹. We

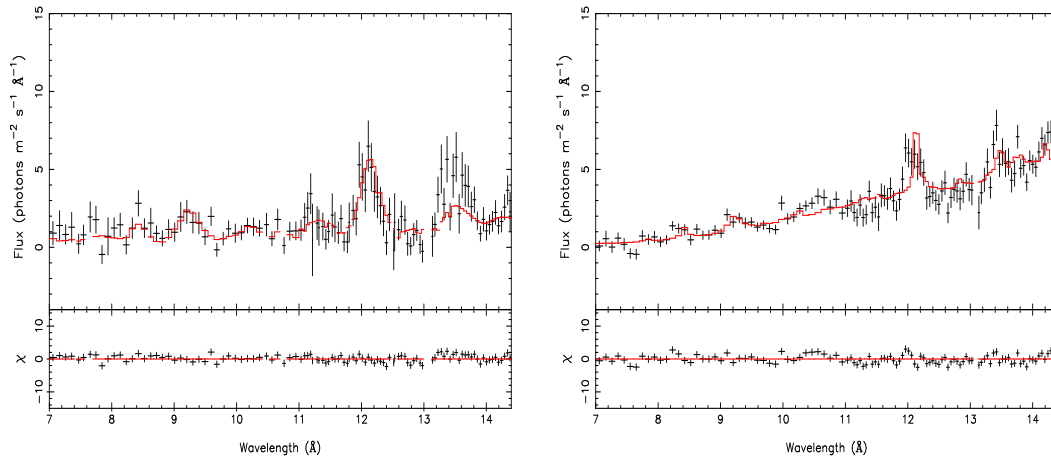


Figure 4.2: V2491 Cyg combined RGS1 and RGS2 flux spectrum in the wavelength range 7-14.4Å. The spectrum is of the era3 is on the left and the spectrum of the second observation is on the right. The model spectrum is represented by the red line and is composed of the plasma emission *cie* and the cold *hot* absorption model for the ISM. An additive blackbody model is used for the continuum emission for the second observation.

also included the second *bb* model in the total RGS band fitting between 7Å and 38Å. However, the spectral parameters, especially the stellar emission did not affected.

Following the initial fitting in hard X-ray band, the determined parameters, abundances of Ne, Mg and v_{mic} , are fixed and full flux fitting is processed for era3. As mentioned before, the high count rate enables us to determine some of the parameters with higher accuracy. The abundances obtained from this iterative fitting is used in era1, era2 and the second observation as well. The abundances are kept fix during both observations since in such a short duration time, 10 days, it is assumed that the elemental abundances in the ejected material or in the wind will be the same. The model fits can be seen in Figure-4.3 and Figure-4.4 and the resulting spectral parameters from the best fits are listed in the Table-4.2. Hydrogen is taken as the reference element in all abundance calculations and the units are given in solar units. The confidence level is 90% for a single parameter in the error calculation. The number of degrees of freedom is around 1400.

For further investigation, we extended the composite model and added a photoionized plasma model *xabs* to see if there will be any improvements in the χ^2_ν . The composite model takes the form [amol x ISM x (cie + (hot₂ x hot₁ x xabs) x bb)]. The existence of a third absorber with photoionized plasma characteristic between the emitting source and the collisionally ionized absorbers improves the fits and the results are given in the Table-4.3.

4.3 Discussion

The X-ray spectroscopy with the help of observatories such as *XMM-Newton* and *Chandra* reached the high-resolution spectra era. Such improvements brought out more complex emission or absorption features that should be examined. Interpretation from these spectra will help to understand the physics that lies beneath. In the case of a nova explosion, ejected material forms optically thick or thin shells surrounding the emitting source. The high energy photons produced from the emitting source had to travel through these shells. The resulting spectrum seen in the high-resolution X-ray grating data is a blackbody-like continuum originating from the photosphere with the combination of absorption lines.

We discussed previously that to derive spectral parameters in X-ray spectroscopy, the first attempt is to use local thermodynamic equilibrium (LTE) and hydrostatic non-local thermodynamic equilibrium models (NLTE) [47]. These models provide a good description for the absorption edges and lines seen in a static atmosphere. However, some of the observed blueshifts in the lines could not be modeled with these models hence to compensate these inadequacies, expanding atmosphere models such as PHOENIX [3] are created. Such expanding models yield better estimated spectral parameters but still far from covering the whole interpretations for the complex absorption features. We aim to model the absorption components that are considered to surround the emitting source. This approach is independent of the choice of the continuum whether it is static or expanding but aims to investigate the effects of an absorber to the spectra. We assume existing absorbers components give rise more complicated profile over the photospheric origin.

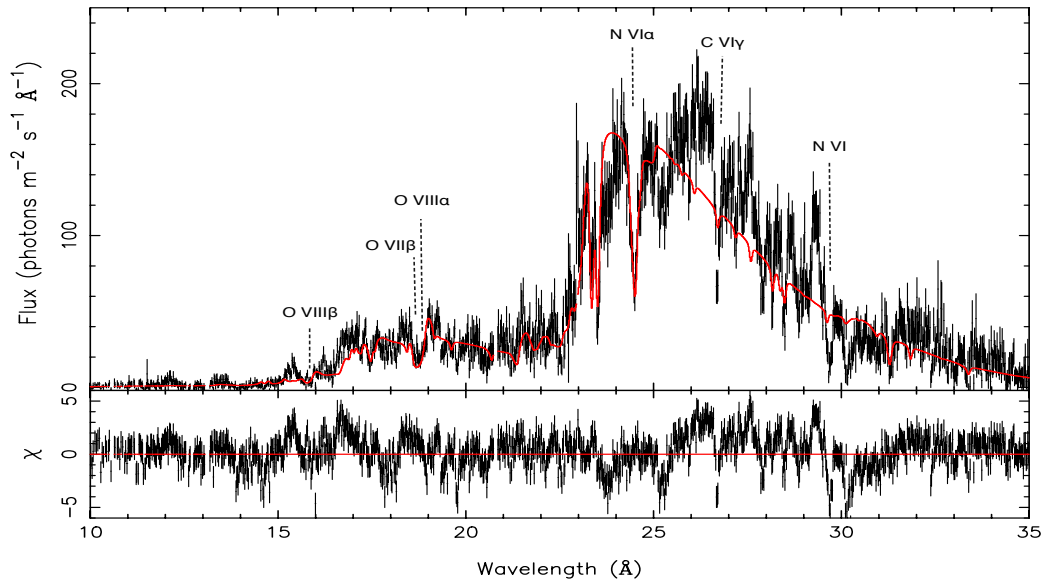
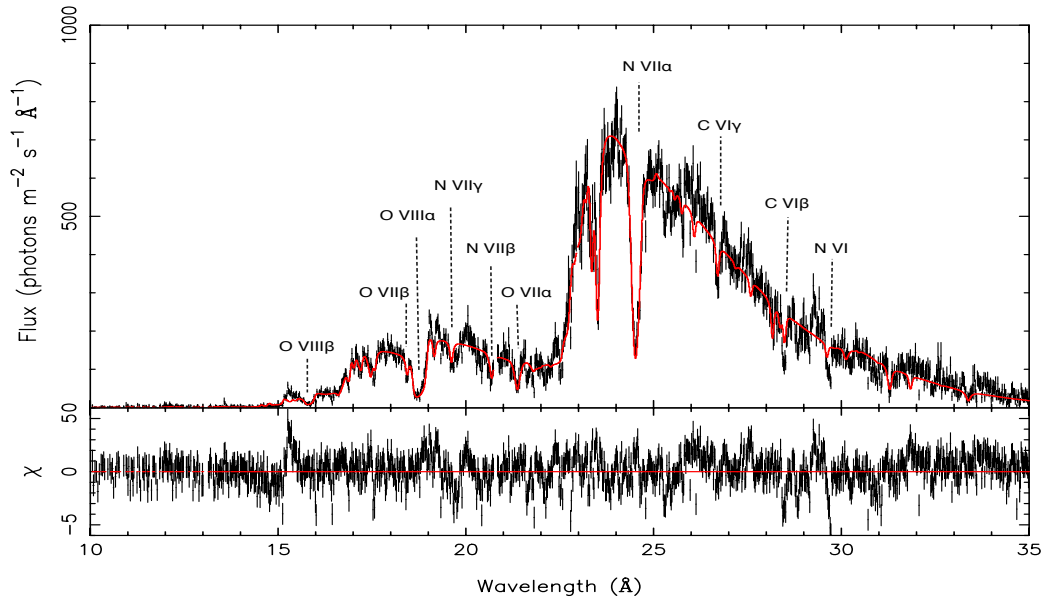


Figure 4.3: The RGS flux spectrum of V2491 Cyg era1 on the top and era2 on the bottom panel. The fitted composite model is represented by the red line. It is constructed by two *hot* models. Several identified blueshifted absorption lines are given in the plots.

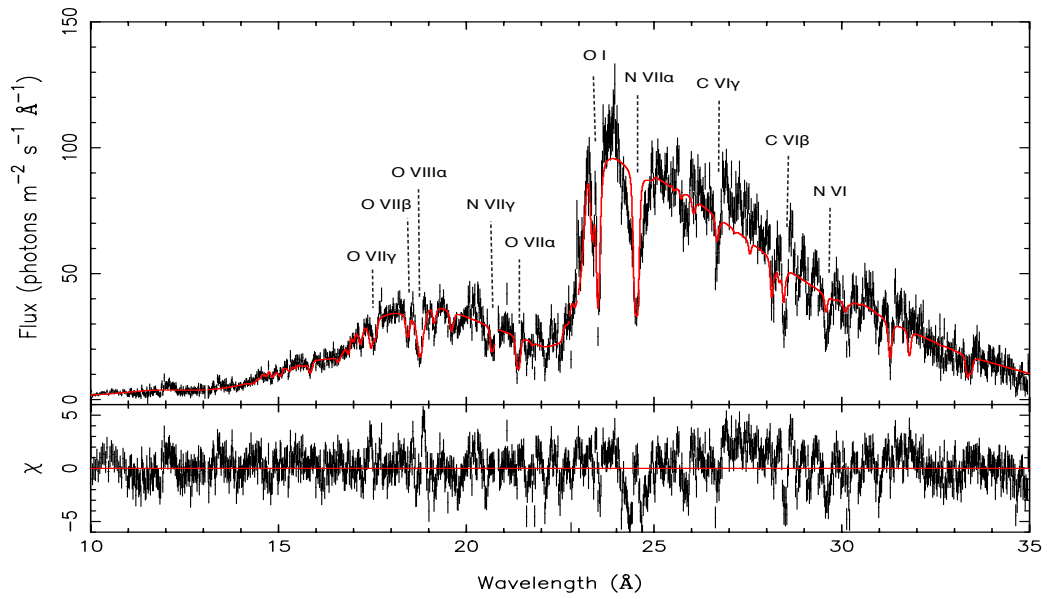
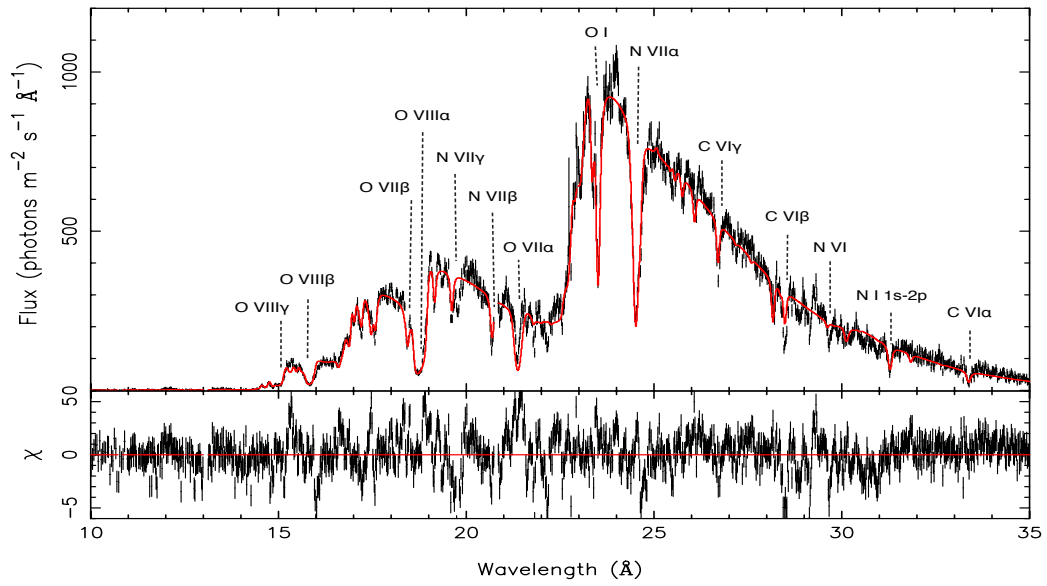


Figure 4.4: The RGS flux spectrum of V2491 Cyg era3 on the top and second observation on the bottom panel. The composite model is constructed with two hot absorption models.

We modeled the continuum emission with a blackbody besides a plasma emission model in collisional equilibrium. The blackbody model is simple. It does not include the absorptions that could exist in the stellar atmospheric emission thus some of the photospheric features would be missing in our analysis. Besides, the blackbody assumption could give Super-Eddington luminosities. However, the choice for the model depends on firstly to reducing the free parameters used in the fitting procedure and then to the impossibility of including a user-defined model to SPEX v 2.05.04 utilized for the analysis. We aim to model the absorber components, hence the blackbody assumption provides a good approximation.

We obtained the blackbody temperature of 61-91 eV ($7.3-10.1 \times 10^5$ K) and 69-85 eV ($8.3-10.0 \times 10^5$ K) from the first and second observation. When an additional warm absorber model *xabs* included, the range narrowed down slightly to 62-85 eV and 78-82 eV respectively. The blackbody temperature for the first observation is larger than the value obtained from *Swift* on day 40, but for the second it is in good agreement with the *Swift* value obtained for day 53 [32]. The effective temperatures with expanding NLTE atmosphere models [39] are lower than our best-fit values, but the ones obtained from fits with photoionized absorbers are higher [45]. The *bb* temperature can also be used to infer the WD mass. It is in the range 1.15-1.3 M_{\odot} consistent with the fast nature of the nova [31].

The normalization parameter of the *bb* is equal to $4\pi R^2$, thus we can calculate the effective radius of the blackbody emitting region and deduce the WD radius. The effective radius are calculated as $32-39 \times 10^8$ cm for the era1, $12-29 \times 10^8$ cm for the era2, era3 and $(2.8-7.5) \times 10^8$ cm for second observation. The consideration of *xabs* as a third absorber slightly changes these limits to $27-30 \times 10^8$ cm, $17-20 \times 10^8$ cm and $2.8-4.9 \times 10^8$ cm respectively. There is a notable change of radius by a factor of 5-10 within 10 days, it is getting smaller. A fast decrease by about a factor of 2-3 in radius within a week was detected earlier for V1974 Cyg [48]. It is also noted that radii above 1×10^9 cm implies a bloated WD. Note that the derived radius for the emission region, on second observation, gives the expected range for the WD radius with CO core [31].

Best fit luminosities are Super-Eddington as discussed previously, see Table-4.2 and

Table 4.1: Elemental abundances obtained with a composite model includes two hot absorber in the first column and with a composite model includes two hot and one warm absorber in the second column

Abundances	Two hot model	Two hot - one warm model
C	$0.43^{+0.07}_{-0.07}$	$0.38^{+0.07}_{-0.07}$
N	$5.9^{+0.5}_{-0.9}$	$5.8^{+0.2}_{-0.2}$
O	$37.9^{+5.8}_{-10.0}$	$15.9^{+0.5}_{-0.5}$
Si	< 0.02	< 0.06
S	$0.02^{+0.01}_{-0.01}$	$0.02^{+0.02}_{-0.01}$
Ar	$1.6^{+3.9}_{-1.2}$	< 0.5
Ca	< 0.01	< 0.02
Fe	$8.9^{+3.8}_{-2.1}$	$8.9^{+3.8}_{-2.1}$

Table-4.3. However, the distance to the source also affects the luminosity calculations. The estimations for the distance to the source V2491 Cyg is 2.1-3.5 kpc to 10.5 kpc and 14 kpc. In our analysis, for the comparison reasons, we assume 10.5 kpc distance to the source; however, a smaller distance will decrease these luminosity values further, by a factor of 10-25, and reducing the values to Eddington limit.

The hard X-ray part of the spectra is modeled with collisional equilibrium emission model *cie* for the derivation of the Ne and Mg abundances. The elemental abundances are around 2.4 and 1.3 in solar units respectively for both observations within the error range, see Table-4.2 and Table-4.3. The temperature derived from the best fits is around 0.2 keV consistent with shock temperatures for stellar winds. But, the luminosities are high due to the simultaneous fit with the *bb* and its inefficiency to model hard X-ray tail [31].

The composite model consists of two collisionally ionized hot absorber components. The first hot component hot_1 show equivalent column density of hydrogen in a range $0.6-4.3 \times 10^{23} \text{ cm}^{-2}$ for first and $1.7-2.9 \times 10^{23} \text{ cm}^{-2}$ for second observation. The absorption drops successively from era1 to era3. Once we include the additional *xabs* model, the ranges of the column density of hot_1 component becomes $0.5-3.9 \times 10^{23} \text{ cm}^{-2}$ for first and $1.4-8.5 \times 10^{23} \text{ cm}^{-2}$ for second observation. In the meanwhile,

hot₂ component is $1.6-18 \times 10^{23} \text{ cm}^{-2}$ to $4.6-5.3 \times 10^{23} \text{ cm}^{-2}$ for first and second observation. The absorption pattern is a little different than the first, here the lowest absorption is in the era2 and then second observation. The values for the column density for hot₂ in Table-4.3 is $2.0-16.2 \times 10^{23} \text{ cm}^{-2}$ and $5.7-7.2 \times 10^{23} \text{ cm}^{-2}$ respectively. There does not seem to be a strong variation in the H column density parameters over the four time intervals, only hot₂ components have higher values than hot₁.

The plasma temperatures can indicate the origin of X-ray emission. The temperature values obtain from the *Swift* observations are 1.0-2.5 keV and 1.8-4.0 keV on day 30 and 53 [32]. These values hint that X-ray emission comes from shocked, fast-moving ejecta. The temperatures we obtained, 1.1-3.6 keV (1st obs.), 1.3-2.0 keV (2nd obs.) for hot₁ and 0.5-1.0 keV (1st obs.), 0.4-0.9 keV (2nd obs.) for hot₂, resemble the *Swift* temperatures. The values on Table-4.2 and Table-4.3 overlaps.

Our best fit results with the composite model of two collisionally ionized absorbers for abundances are $C/C_{\odot}=0.3-0.5$, $N/N_{\odot}=5-7$ and $O/O_{\odot}=28-43$. When the third photoionized absorber component is taken into account, the oxygen abundance becomes $O/O_{\odot}=15-17$ while the abundance of the carbon and nitrogen remain the same. We find that C is underabundant while N is overabundant as expected from H-burning process. The overabundance of oxygen implies the existence of an WD with CO core. The abundances for the other nova elements are also listed in Table-4.1.

The additional warm absorber component improves the overall model fitting. This indicates a variety in the absorption components and their origins. It also indicates that photoionized absorption is present in the expanding nova shell. The hydrogen column density of the photoionized absorption is $1.3-4.3 \times 10^{20} \text{ cm}^{-2}$ for first and $0.5-0.7 \times 10^{20} \text{ cm}^{-2}$ for the second observation, as can be seen in Table-4.3. The same parameter for interstellar material in the line of sight is higher than these values and they are made of 1-0.1% absorption of the collisionally ionized gas [31].

The absorption due to interstellar material is imitated by using the hot model with low temperature, 1 eV and the neutral hydrogen column density derived as about $3.2-4.2 \times 10^{21} \text{ cm}^{-2}$ for first and $2.2-2.7 \times 10^{21} \text{ cm}^{-2}$ for second observations from the best fits. The estimated value derived from *Swift* data and the resulting value from nhtot along the line of sight, $(3.8-5.5) \times 10^{21} \text{ cm}^{-2}$, is in very good agreement with

Table 4.2: RGS best fit spectral parameters of the four time intervals derived from the composite model constructed with two Hot absorber models.

Model	Parameters	Era1	Era2	Era3	2 nd Obs.
BB	Norm (10^{20}cm^2)	$1.53^{+0.39}_{-0.25}$	$0.23^{+0.86}_{-0.04}$	$0.40^{+0.47}_{-0.21}$	$0.02^{+0.05}_{-0.01}$
	kT (eV)	$68.5^{+0.9}_{-0.9}$	$64.5^{+0.6}_{-3.6}$	$88.4^{+2.7}_{-1.8}$	$75.7^{+9.1}_{-6.5}$
	L(10^{39}erg s^{-1})	2.18	0.23	1.92	0.05
CIE	Norm (10^{58}cm^{-3})	$0.40^{+0.11}_{-0.09}$	$0.72^{+0.79}_{-0.32}$	$0.42^{+0.13}_{-0.05}$	$0.27^{+0.06}_{-0.1}$
	kT (keV)	$0.20^{+0.01}_{-0.01}$	$0.16^{+0.03}_{-0.02}$	$0.20^{+0.01}_{-0.01}$	$0.30^{+0.13}_{-0.03}$
	v_{mic} (km s^{-1})	2791	2791	2791^{+333}_{-288}	25068^{+1383}_{-951}
	Ne	2.45	2.45	$2.45^{+1.36}_{-0.92}$	$2.4^{+0.9}_{-0.9}$
	Mg	1.2	1.2	$1.2^{+1.0}_{-0.6}$	$1.98^{+0.70}_{-0.70}$
	L(10^{36}erg s^{-1})	1.31	1.78	1.38	0.77
	HOT-1	N_H (10^{23}cm^{-2})	$4.0^{+0.3}_{-0.3}$	$0.9^{+0.3}_{-0.1}$	$0.7^{+0.1}_{-0.1}$
kT (keV)		$2.63^{+0.96}_{-0.56}$	$1.77^{+0.17}_{-0.12}$	$1.06^{+0.03}_{-0.03}$	$1.38^{+0.58}_{-0.12}$
σ_v (km s^{-1})		872^{+25}_{-24}	827^{+61}_{-86}	879^{+12}_{-12}	114^{+18}_{-15}
z_v (km s^{-1})		-3186^{+51}_{-50}	-3699^{+113}_{-173}	-3128^{+30}_{-31}	-2636^{+47}_{-45}
HOT-2	N_H (10^{23}cm^{-2})	$8.6^{+0.3}_{-0.3}$	$1.8^{+0.1}_{-0.2}$	$18.0^{+0.2}_{-0.2}$	$5.1^{+0.2}_{-0.5}$
	kT (keV)	$0.81^{+0.03}_{-0.03}$	$0.58^{+0.07}_{-0.11}$	$0.99^{+0.03}_{-0.03}$	$0.82^{+0.05}_{-0.45}$
	σ_v (km s^{-1})	54^{+8}_{-9}	< 9	56^{+4}_{-5}	60^{+7}_{-8}
	z_v (km s^{-1})	-3180^{+71}_{-58}	-3038^{+6}_{-183}	-3194^{+30}_{-31}	-3550^{+36}_{-33}
ISM	N_H (10^{21}cm^{-2})	$3.89^{+0.06}_{-0.06}$	$3.84^{+0.06}_{-0.19}$	$3.26^{+0.05}_{-0.09}$	$2.4^{+0.3}_{-0.2}$
	kT (eV)	$1.11^{+0.03}_{-0.04}$	$1.20^{+0.02}_{-0.04}$	$1.01^{+0.02}_{-0.02}$	$0.8^{+0.3}_{-0.3}$
	N	1.16	1.16	$1.16^{+0.12}_{-0.12}$	1.16
	O	1.75	1.75	$1.75^{+0.04}_{-0.02}$	1.75
	Fe	0.95	0.95	$0.95^{+0.13}_{-0.12}$	0.95
AMOL	O_2 (10^{17}cm^{-2})	$0.34^{+0.13}_{-0.13}$	$2.3^{+0.2}_{-0.2}$	< 0.1	$1.3^{+0.1}_{-0.1}$
	H_2O (10^{17}cm^{-2})	$5.5^{+0.3}_{-0.3}$	$7.8^{+0.5}_{-0.5}$	$4.77^{+0.13}_{-0.13}$	$7.2^{+0.2}_{-0.2}$
	CO (10^{17}cm^{-2})	$1.28^{+0.13}_{-0.13}$	$0.27^{+0.2}_{-0.2}$	$0.1^{+0.07}_{-0.06}$	< 0.1
	χ^2_ν	1.80	2.4	2.86	2.3
	(d.o.f.)	(1415)	(1439)	(1440)	(1465)

Table 4.3: RGS best fit spectral parameters of the four time intervals derived from the composite model constructed with two Hot absorber and one warm absorber models.

Model	Parameters	Era1	Era2	Era3	2 nd Obs.
BB	Norm (10^{20}cm^2)	$0.99^{+0.06}_{-0.06}$	$0.46^{+0.05}_{-0.05}$	$0.40^{+0.01}_{-0.01}$	$0.02^{+0.01}_{-0.01}$
	kT (eV)	$68.1^{+0.5}_{-0.5}$	$63.1^{+1}_{-0.8}$	$84.6^{+0.4}_{-0.4}$	$79.9^{+1.2}_{-1.2}$
	L(10^{39}erg/s)	1.37	0.43	1.57	0.06
CIE	Norm (10^{58}cm^{-3})	$0.97^{+0.47}_{-0.37}$	$1.14^{+0.71}_{-0.40}$	$0.42^{+0.13}_{-0.05}$	$0.55^{+0.04}_{-0.04}$
	kT (keV)	$0.18^{+0.02}_{-0.01}$	$0.17^{+0.02}_{-0.02}$	$0.19^{+0.01}_{-0.01}$	$0.26^{+0.01}_{-0.01}$
	v_{mic} (km s^{-1})	2914	2914	2914^{+612}_{-510}	22410^{+1688}_{-1466}
	Ne	2.45	2.45	$2.45^{+1.36}_{-0.92}$	$2.4^{+0.9}_{-0.9}$
	Mg	1.2	1.2	$1.2^{+1.0}_{-0.6}$	$1.98^{+0.70}_{-0.70}$
	L(10^{36}erg s^{-1})	1.34	1.49	1.18	0.88
	N_H (10^{23}cm^{-2})	$0.8^{+0.1}_{-0.1}$	$1.3^{+2.6}_{-0.5}$	$0.6^{+0.1}_{-0.1}$	$1.6^{+6.9}_{-0.2}$
HOT-1	kT (keV)	$0.95^{+0.04}_{-0.04}$	$2.48^{+0.52}_{-0.35}$	$0.94^{+0.02}_{-0.02}$	$1.19^{+0.86}_{-0.20}$
	σ_v (km s^{-1})	892^{+43}_{-41}	634^{+131}_{-156}	932^{+23}_{-23}	133^{+31}_{-28}
	z_v (km s^{-1})	-3304^{+83}_{-83}	-3805^{+229}_{-278}	-3250^{+51}_{-51}	-2826^{+88}_{-97}
	N_H (10^{23}cm^{-2})	$7.6^{+0.2}_{-0.2}$	$4.4^{+0.5}_{-2.4}$	$16.1^{+0.1}_{-0.1}$	$7.1^{+0.1}_{-1.4}$
HOT-2	kT (keV)	$0.89^{+0.05}_{-0.04}$	$0.59^{+0.02}_{-0.1}$	$1.06^{+0.02}_{-0.02}$	$0.68^{+0.01}_{-0.19}$
	σ_v (km s^{-1})	< 37	< 20	35^{+14}_{-18}	< 17
	z_v (km s^{-1})	-3309^{+84}_{-103}	-3073^{+161}_{-191}	-3334^{+38}_{-36}	-3660^{+75}_{-65}
XABS	N_H (10^{20}cm^{-2})	$2.68^{+0.4}_{-0.3}$	$3.85^{+40}_{-2.56}$	$2.79^{+0.1}_{-0.1}$	$0.56^{+0.06}_{-0.06}$
	Log ξ (erg cm s^{-1})	$2.04^{+0.14}_{-0.16}$	$3.64^{+1.35}_{-0.2}$	$2.18^{+0.05}_{-0.05}$	$0.41^{+0.08}_{-0.07}$
	σ_v (km s^{-1})	49^{+126}_{-18}	< 15831	53^{+10}_{-9}	195^{+78}_{-58}
	z_v (km s^{-1})	-3013^{+100}_{-368}	-1093^{+1294}_{-343}	-2968^{+47}_{-44}	-3127^{+127}_{-118}
ISM	N_H (10^{21}cm^{-2})	$3.81^{+0.05}_{-0.05}$	$4.15^{+0.05}_{-0.06}$	$3.31^{+0.02}_{-0.02}$	$2.4^{+0.1}_{-0.1}$
	kT (eV)	$1.09^{+0.07}_{-0.3}$	$1.20^{+0.03}_{-0.05}$	$1.01^{+0.04}_{-0.04}$	$0.8^{+0.1}_{-0.1}$
	N	1.12	1.12	$1.12^{+0.13}_{-0.14}$	1.12
	O	1.68	1.68	$1.68^{+0.02}_{-0.02}$	1.68
	Fe	0.81	0.81	$0.81^{+0.13}_{-0.12}$	0.81
AMOL	O_2 (10^{17}cm^{-2})	$0.47^{+0.61}_{-0.03}$	$1.48^{+0.23}_{-0.24}$	< 0.4	$0.9^{+0.1}_{-0.1}$
	H_2O (10^{17}cm^{-2})	$5.1^{+1.2}_{-0.1}$	$7.4^{+0.5}_{-0.5}$	$4.65^{+0.3}_{-0.7}$	$6.4^{+0.2}_{-0.2}$
	CO (10^{17}cm^{-2})	$1.34^{+0.53}_{-0.03}$	$0.29^{+0.2}_{-0.2}$	$0.16^{+0.07}_{-0.06}$	< 0.2
	χ^2_ν	1.73	2.38	2.46	2.06
	(d.o.f.)	1411	1435	1436	1463

our findings.

We need to note that in the line of sight there is also dust molecules that should be considered. Related to the dust content some absorption features seen in the spectra are affected. Especially, the spectral regions between 22.5-23.2Å and 17.2-17.7 Å suffer from dust and molecular effects. To be able to fit the features in these regions we use *amol* model including the oxygen molecule, carbon monoxide and water ice. The dust content we obtained is $0.1-2.5 \times 10^{17} \text{ cm}^{-2}$ for the O_2 and $4.64-8.3 \times 10^{17} \text{ cm}^{-2}$ for the H_2O_{ice} . The variation seen in the light curve of first observation seems to correlate with the amount of the dust absorption as far as O_2 and H_2O_{ice} are concerned. The more the dust absorption is the less the count rate in the LC. The second observation has similar dust absorption to era2.

We derived the blueshifts seen in the absorbed lines from absorber velocities. The values are in a range, hot_1 , 3097-3812 km s^{-1} and, hot_2 , 2845-3250 km s^{-1} for the first observation. The similar values are obtained with the composite model including warm absorber, see Table-4.3. Second observation fits yield velocities, hot_1 , 3517-3586 km s^{-1} and, hot_2 , 2590-2683 km s^{-1} . When the third model is added these ranges are slightly altered to 2730-2914 km s^{-1} and 3660-3735 km s^{-1} respectively. These velocities are in good agreement with the nova shell expansion velocities and the ones obtained in the previous studies, see the introduction. The additional warm absorber velocities are initially in a range 750-3113 km s^{-1} , then 10 days after in the range 3009-3254 km s^{-1} . Assuming Eddington luminosities, ionization parameter is $\xi = L/n r^2$ and using the equivalent hydrogen densities in Table-4.3, the location of the warm absorber can be determined as in the expanding nova shell for all the fits.

We can also estimate the spectral parameter, turbulent velocity broadening from the absorber components. In the case of hot_1 , it is in a range 740-897 km s^{-1} and 100-132 km s^{-1} for the first and second observations. These values are 9-62 km s^{-1} and 52-67 km s^{-1} for hot_2 . One could get similar results for hot components by using the additional warm absorber, as listed in Table-4.3. Here, the turbulent velocity broadening for the *xabs* ranges 31-174 km s^{-1} and 137-273 km s^{-1} . The turbulent velocity broadening indicates the locations of the absorbers. The differences in the velocities of the first and the second collisionally hot absorbers suggest the locations

also differ. It shows that with locations of different densities, turbulent characteristics and temperatures, the flow of the ejecta/wind is inhomogeneous.

The χ^2_ν values obtained from the best fits are listed in Table-4.2. They are 1.8, 2.4, 2.9 and 2.3 from era1 to era3 and finally second observations with approximately 1400 degrees of freedom. The achieved χ^2_ν values are improved compared to the previous studies in the literature [45, 13]. We tested the possibility of having third warm absorber and give the details of the fits in Table-4.3. The inclusion gives a significant improvement in the era3, 2.5 which has the highest χ^2_ν value and the details can be seen in [31].

The particular change is seen in the blackbody component parameters hence inside the emitting region. The large scale variation of the light curve of the first observation could be the result of variation in these parameters. However, the changes in the hydrogen column density and the temperatures of the hot components should also be noted. The change in such parameters can be caused by rekindled irregular accretion onto the surface of the H-burning WD and that contributes to the change in the count rates. Previously mentioned additional blackbody component has the effective radius that is consistent with structures on an accretion disk. It also corresponds to 10% of the size of the WD calculated from the second observation that can be explained with accretion hot spots in intermediate polar CVs [31]. The results suggest that the accretion could have been established on the time of second observation; besides, the blackbody radius and temperature supports the magnetic nature of the source [38].

CHAPTER 5

V4743 SGR

Katsumi Haseda, Japan, reported the discovery of a possible nova with a visual magnitude ~ 5 mag on September 20, 2002 [49]. It was a very bright and fast nova, and the source is assigned as V4743 Sgr [50]. The decline time t_3 was within 15 days (around 9 days) [51].

V4743 Sgr was observed by *Chandra* HRC-S+LETG on March 19, 2003, for 7 hours before any observation done by *XMM-Newton* [52]. The main feature in the light curve is the slow decay in count rate almost halfway through the total exposure. It took 1.5 hours to count rate to drop near zero and remained the same for another 1.5 hours. Such a decrement could not be seen in any other observations. It is considered to be due to an eclipse of the system, however during almost 10-hour observation of *XMM-Newton* such an eclipse had not been observed. This could be either due to another mechanism that obscures the X-ray emission or the fact that the orbital period is higher than the exposure time of the *XMM-Newton*.

The photometric studies suggested that the source is Fe_{II} nova and FWHM of the H_α emission line is 2400 km/s [53]. They also revealed two periods 6.7 hours and ~ 24 min [54]. The longer period considered as the orbital period of the binary system. The orbital variation with 6.7 hours can be observed in the *XMM-Newton* data. Hence, the decrement seen in the *Chandra* is not due to a considerable high inclination that cause an eclipse but rather due to another mechanism that obscures the X-ray emission.

In the X-ray analysis also a 22-minute signal is found and considered to be a rotation period of the central WD [55]. Hence, the 24-minute signal seen in the optics can be the beat period between the orbital period of the binary and the rotation period of

WD. Observation of binary period and the probable WD rotation suggests the source V4743 Sgr is an intermediate polar [56]. The interpretation of the intermediate polar scenario is also supported by the latest X-ray observations [57]. The more complex timing analysis revealed that there could be two close frequencies that modulate the outburst [58, 59]. On the other hand, it is shown that such two signal characteristics can be modeled by a single signal with constant frequency but variable modulation amplitude [56]. There is an ongoing debate about the multifrequency nature of the oscillations and their origin whether it is due to the rotation of the WD or the pulsations. The interpretation of the case of nova V4743 Sgr is a challenge.

The millimeter emission studies of V4743 Sgr gave an estimation for the distance to the source, (1200 ± 300) pc. However, the distance estimations are not viable since the extinction along the line of sight depends on the choice of the assumptions. Despite these inadequacies, one can calculate the maximum distance to the source with given distance modulus and it is estimated as 6 kpc [51].

The interstellar matter absorption should be considered in the spectral analyses as discussed in Chapter 4. The Interstellar column density in our observation direction is given by NASA's heasarc $N(\text{H})$ ftool¹ as $1.05 \times 10^{21} \text{cm}^{-2}$. It is also estimated in several earlier X-ray analysis in a range $1.36\text{-}1.41 \times 10^{21} \text{cm}^{-2}$ [57].

5.1 Observations and the data

A classical nova V4743 Sgr was observed by XMM-Newton RGS in April 2003, for an exposure of 35 ks. We use this observation and obtain high-resolution X-ray spectra of the source. As discussed in the Chapter-2, this observation affected by the pile-up causing the EPIC or PN data to be unusable. Hence, the analysis focused on RGS data that is processed with SAS *rgsproc* routine.

RGS1 and RGS2 first and second order source and background count spectra are extracted. Then, RGS1 and RGS2 only first order flux spectra obtained and combined for the further analysis. Here, the flux spectra are obtained between 5-40 Å with 3600 bins. The resultant spectra are binned by a factor of two. We utilize SRON soft-

¹ <http://heasarc.gsfc.nasa.gov/ftools>

ware SPEX 3.03.00 that consists of absorption models mimicking a hot collisionally ionized plasma and a warm photoionized plasma to see if we can able to compose a well-fitted model.

5.2 Analysis and Results

The RGS spectra of V4743 Sgr show complex absorption features and a blueshift in the spectra that could not be well explained by the stellar atmospheric models [60, 2, 3, 57]. The main motivation for the analysis was to look for hot and warm plasma absorbers originating either from wind or ejecta that affect the resulting spectra as in the case of V2491 Cyg.

The light curve of V4743 Sgr obtained from RGS1 first order data is shown in Figure-5.1 on the left panel. The data is averaged with 100s for clarity. The count rate is very high and it varies between 40 - 63 counts s^{-1} during the observation. Apart from the large variation, a smaller oscillation can be clearly seen. This modulation is around ~ 1300 s and can vary the count rate in some places almost as large as 10 counts.

The spectrum has similarities with the super soft sources SSS and the continuum emission ranges between 18-38 Å. The smaller wavelengths are inadequate for the analysis. The signal for these wavelengths is dominated by the background. The spectra peaked around 31 Å and the dominant absorption lines are NVI around 24.9 and 28.8 Å, NVII 24.8 and 20.9 Å and OVII around 21.60. There is also sulfur SXIV line at 32.5 and carbon line CV at 33.5 Å.

The best fitted composite model has a similar structure the ones used in V2491 Cyg analysis. Only, here there is one continuum model, blackbody that is overlapped by the absorber components. *Amol* is used for the dust absorption, interstellar absorption is modeled by *hot* with low temperature and there is one *hot* for collisionally ionized hot absorber component and two warm photoionized absorbers. The resultant composite model is [amol x ISM x hot x xabs₂ x xabs₁ x bb]. The spectral analysis of the full exposure indicates that the models are inadequate. Therefore, we investigate the light curve of V4743 Sgr, showing periodic variability during the observation in addition to variability in the long term as discussed in [56]. The variability can be seen in

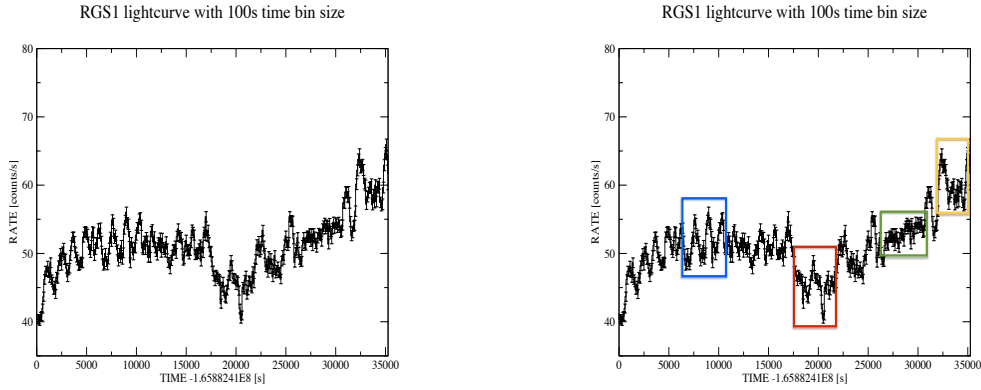


Figure 5.1: The left panel shows light curve (LC) of V4743 Sgr XMM-Newton RGS1 data averaged with 100s for clarity. The spectra used in the analysis are obtained from the indicated regions that are shown in the right panel. The first region on the left shown in blue is considered as the time interval where the periodic variability is clearly visible. We obtained consecutive six spectra from this region where the crests are labeled as p1, p2, p3 and troughs as b1, b2, b3 respectively. The second region from the left in red is considered as low region where the variability is not well defined as in first region. We divided the region into three time intervals, two troughs and one peak, and obtained three spectra b11, p1, b12. The second one from the right in green is labeled as valley. Here, the periodicity subdues and the prominence of the peaks disappears. The last region in yellow considered as high region and two spectra are obtained called as high-peak (hp) and high-bottom (hb) respectively.

the left panel of Figure-5.1. We consider that the variability in the light curve may be caused by different physical environments hence resulted in different characteristics in the spectra. As a result, we work on several time-resolved spectra that are taken from the regions shown in the right panel of Figure-5.1. There are four main regions where the count rate and the periodicity differs and the details are given in the caption of Figure-5.1.

The aim is to divide the observations to smaller ordered time intervals to obtain spectra is that we would like to investigate the origins of the modulation and the reasons behind the inadequacies of the full spectral fitting. If there is pulsation of WD due to the instability of the surrounding environment, there should be differences in the

spectral parameters or even in the composite model in some cases. For this purpose, we obtained twelve flux spectra processed with SAS *rgsproc* and combined as previously discussed.

All twelve spectra are fitted with the composite model separately and simultaneously. The model fits of RGS1 flux spectra of V4743 Sgr are given in Figure-5.2, 5.3, 5.4, 5.5. Spectral parameters obtained from a best fitted composite model of V4743 Sgr RGS spectra are given in Table-5.2 and Table-5.3. In the V4743 Sgr analysis, we consider the abundances may also be affected by the modulation hence the parameters are kept free and the corresponding results can be seen in Table-5.1. Hydrogen is taken as the reference element in all abundance calculations and the units are given in solar units. The confidence level is 90% for a single parameter in the error calculation. The degrees of freedom are taken around 950.

5.3 Discussion

The normalizations for the blackbody in the first region where we obtained six spectra are in the range $0.99-1.92 \times 10^{20}$ cm, while in the high-region it is $3.09-4.62 \times 10^{20}$ cm. These give an effective radius of $R=28-39 \times 10^8$ cm and $R=49-60 \times 10^8$ cm. The effective temperatures are in a range of 40-46 eV. Low-region spectra show similar results with an exception of peak spectra that resembles the valley spectra. The normalization lower bound drops to 0.51×10^{20} cm that gives $R=20 \times 10^8$ cm with an effective temperature 48-45 eV.

The first resulting warm absorption model has various hydrogen column density N_H values among the spectra. It ranges from $N_{H1} \simeq 0.45-27.88 \times 10^{21}$ cm⁻² in the first region spectra to $83.3-67.3 \times 10^{21}$ cm⁻² in another. Ionization parameter is $\text{Log}(\xi_1) \simeq 3.4-4.4$ erg cm s⁻¹ and it tends to increase after the first region. The rms velocities are in the range 2218-3370 km s⁻¹ and blueshifts are in 2727-3486 km s⁻¹. Second warm absorber shows more consistent results and has $N_{H2} \simeq 0.12-0.42 \times 10^{20}$ cm⁻² with ionization parameter $\text{Log}(\xi_2) \simeq 1.3-2.3$ erg cm s⁻¹. The rms velocities are in the range 166-53 km s⁻¹ and blueshifts are in 2190-2669 km s⁻¹.

The hot component has $N_H \simeq 1.0-73.8 \times 10^{21}$ cm⁻² and temperature deviating between

Table 5.1: Best fit elemental abundances of the V4743 Sgr given in solar units. The below spectra are given in ascending time order.

Abundances	b1	p1	b2	p2	b3	p3
C	$0.4^{+0.3}_{-0.2}$	$0.2^{+0.1}_{-0.1}$	$0.5^{+0.2}_{-0.2}$	$0.2^{+0.1}_{-0.1}$	$0.3^{+0.2}_{-0.1}$	$0.1^{+0.1}_{-0.07}$
N	$67.1^{+3.9}_{-3.3}$	$54.9^{+3.6}_{-3.4}$	$50.6^{+2.9}_{-2.2}$	$85.1^{+4.2}_{-3.7}$	$68.2^{+3.0}_{-3.0}$	$81.2^{+3.7}_{-3.6}$
O	$1.4^{+0.7}_{-0.5}$	$1.6^{+0.6}_{-0.5}$	$1.6^{+0.5}_{-0.4}$	$1.7^{+0.6}_{-0.5}$	$2.0^{+0.6}_{-0.5}$	$2.8^{+0.8}_{-0.6}$
Ne	0.01^{+3}_{-}	0.01^{+3}_{-}	0.01^{+3}_{-}	$0.8^{+2.1}_{-0.7}$	0.01^{+3}_{-}	$0.1^{+2.9}_{-0.09}$
Mg	0.01^{+3}_{-}	$0.01^{+2.6}_{-}$	0.01^{+3}_{-}	$0.01^{+1.8}_{-}$	$0.01^{+2.1}_{-}$	$0.01^{+1.4}_{-}$
Si	0.01^{+1}_{-}	$0.01^{+0.1}_{-}$	$0.01^{+0.4}_{-}$	$0.01^{+0.17}_{-}$	$0.01^{+0.09}_{-}$	$0.01^{+0.09}_{-}$
S	$0.01^{+0.05}_{-}$	$0.01^{+0.01}_{-}$	$0.01^{+0.1}_{-}$	$0.01^{+0.03}_{-}$	$0.02^{+0.26}_{-0.15}$	$0.01^{+0.03}_{-}$
Ar	$3^{+}_{-1.2}$	$0.01^{+0.04}_{-}$	$1.2^{+1.2}_{-1.1}$	$0.01^{+0.13}_{-}$	$0.01^{+0.03}_{-}$	$0.01^{+0.06}_{-}$
Fe	$0.25^{+0.79}_{-0.24}$	$0.01^{+0.03}_{-}$	$0.01^{+0.03}_{-}$	$0.01^{+0.03}_{-}$	$0.01^{+0.05}_{-}$	$0.01^{+0.02}_{-}$

Abundances	bl1	pl	bl2	valley	hp	hb
C	$0.6^{+0.2}_{-0.1}$	$0.8^{+0.9}_{-0.6}$	$0.7^{+0.2}_{-0.1}$	$0.5^{+0.1}_{-0.1}$	$0.13^{+0.05}_{-0.04}$	$0.12^{+0.04}_{-0.04}$
N	70.3^{+2}_{-2}	$60.0^{+3.7}_{-8.3}$	$61.3^{+2.3}_{-2.1}$	$124.8^{+2.2}_{-2.1}$	$46.4^{+2.5}_{-1.6}$	$74.1^{+3.1}_{-2.7}$
O	$3.3^{+0.1}_{-0.5}$	$9.0^{+4.7}_{-2.3}$	$37.9^{+7.2}_{-6.4}$	$45.8^{+5.5}_{-4.4}$	$1.6^{+0.4}_{-0.3}$	$7.6^{+1.0}_{-1.7}$
Ne	$2.3^{+0.7}_{-2.2}$	3^{+}_{-3}	$0.8^{+2.2}_{-0.7}$	3^{+}_{-}	$0.6^{+2.4}_{-0.5}$	0.01^{+3}_{-}
Mg	$3^{+}_{-0.8}$	$2.1^{+0.9}_{-0.8}$	$3^{+}_{-1.2}$	$3^{+}_{-0.5}$	$2.0^{+1.0}_{-1.9}$	0.01^{+3}_{-}
Si	$0.9^{+0.6}_{-0.4}$	$0.9^{+2.1}_{-0.3}$	$1.4^{+0.7}_{-0.5}$	$0.38^{+0.18}_{-0.12}$	$0.01^{+0.06}_{-}$	$0.01^{+0.04}_{-}$
S	$2.7^{+0.3}_{-0.6}$	$3^{+}_{-1.9}$	$3^{+}_{-0.4}$	$2.53^{+0.46}_{-0.6}$	$0.02^{+0.02}_{-0.01}$	$0.01^{+0.02}_{-}$
Ar	$0.2^{+0.2}_{-0.1}$	$1^{+0.1}_{-0.9}$	$0.4^{+0.1}_{-0.1}$	$0.26^{+0.1}_{-0.07}$	$0.01^{+0.18}_{-}$	$0.01^{+0.33}_{-}$
Fe	$3^{+}_{-0.5}$	$1^{+2}_{-0.1}$	$2.7^{+0.3}_{-0.3}$	$0.85^{+0.21}_{-0.17}$	$0.08^{+0.6}_{-0.07}$	$0.01^{+0.97}_{-}$

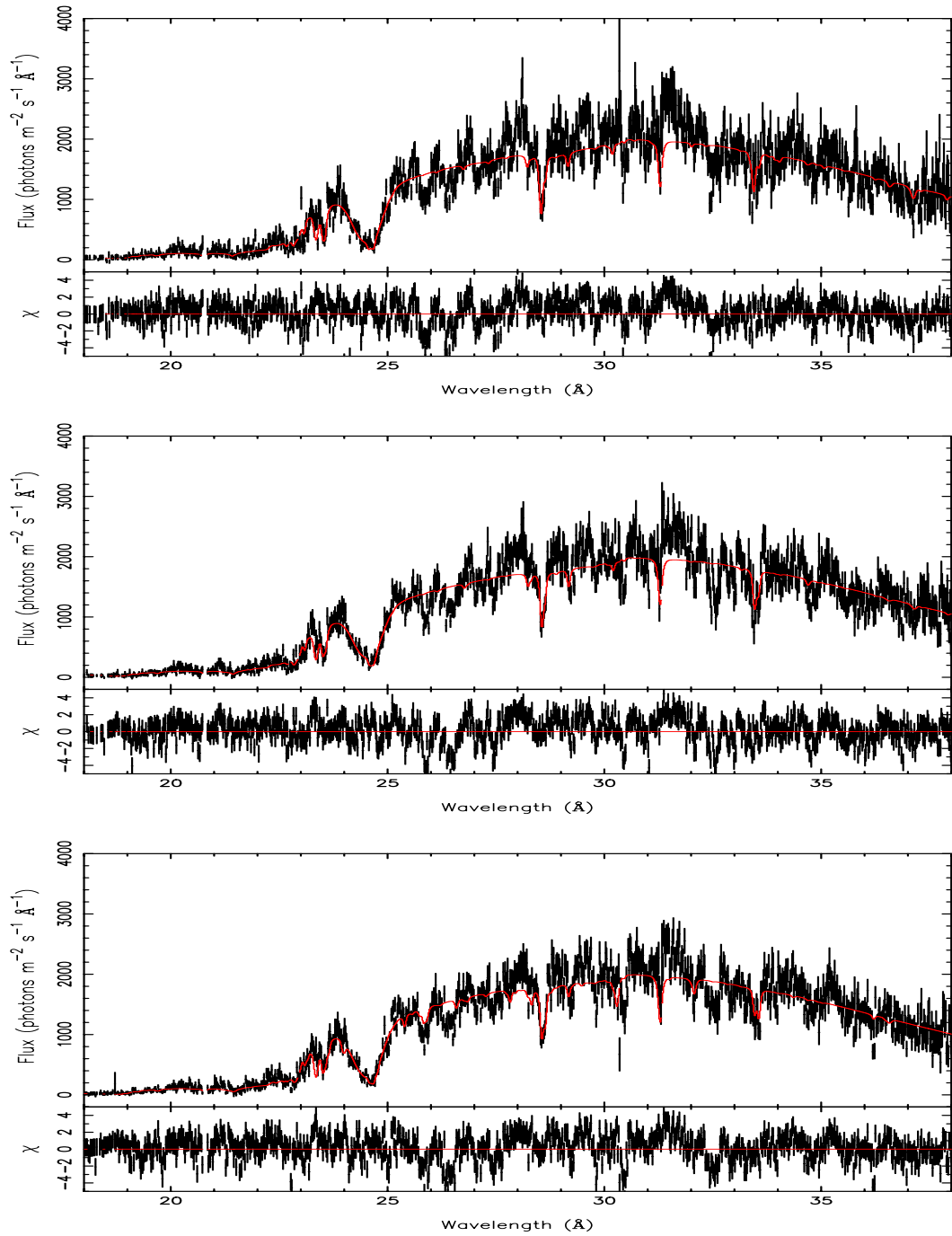


Figure 5.2: RGS1 flux spectra of V4743 Sgr fitted with the composite model. From top to bottom panel, plots show b1, b2 and b3 spectra respectively as indicated in the LC. The red line shows the best fitted composite model.

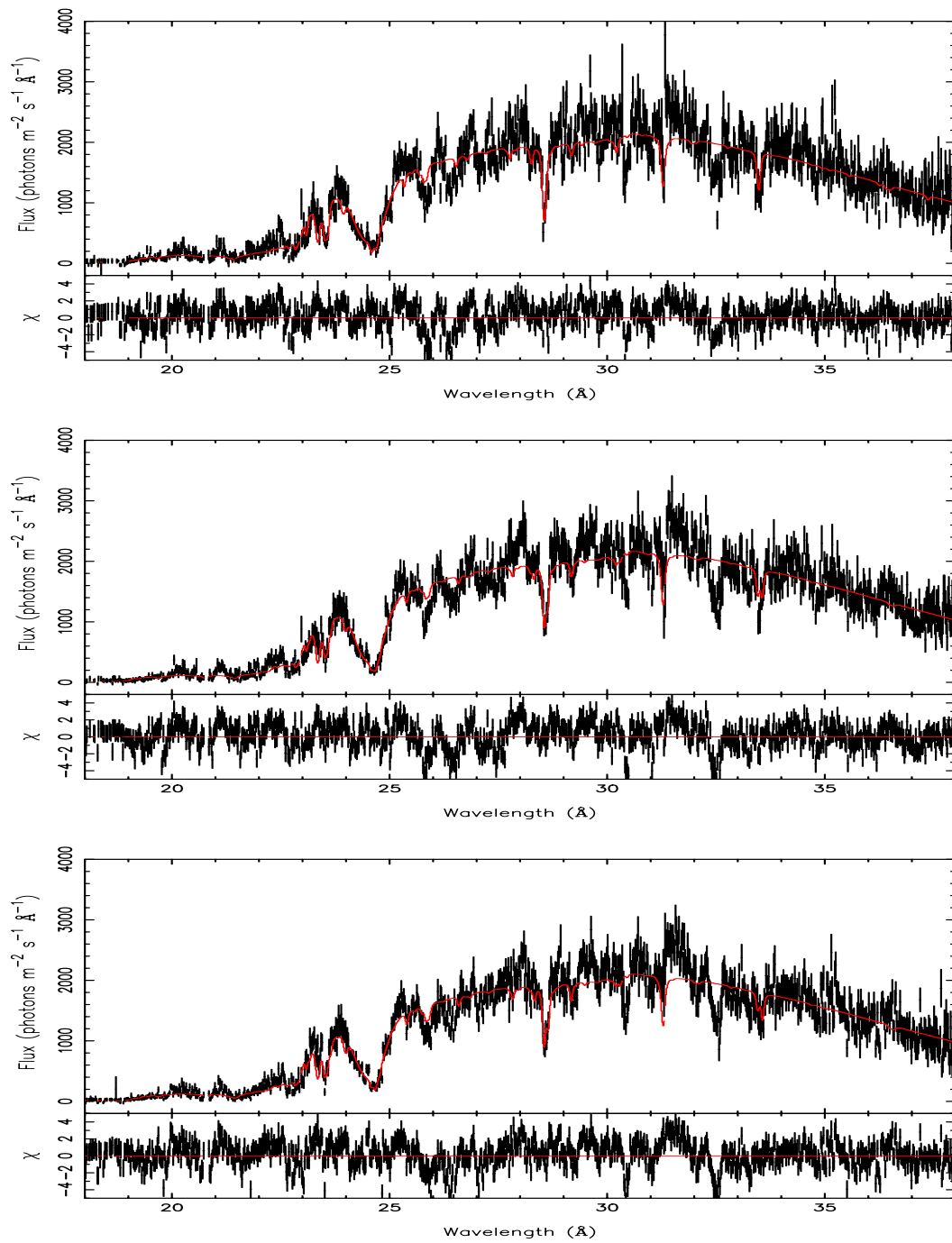


Figure 5.3: RGS1 flux spectra of V4743 Sgr fitted with the composite model. From top to bottom panel, plots show p1, p2 and p3 spectra respectively as indicated in the LC.

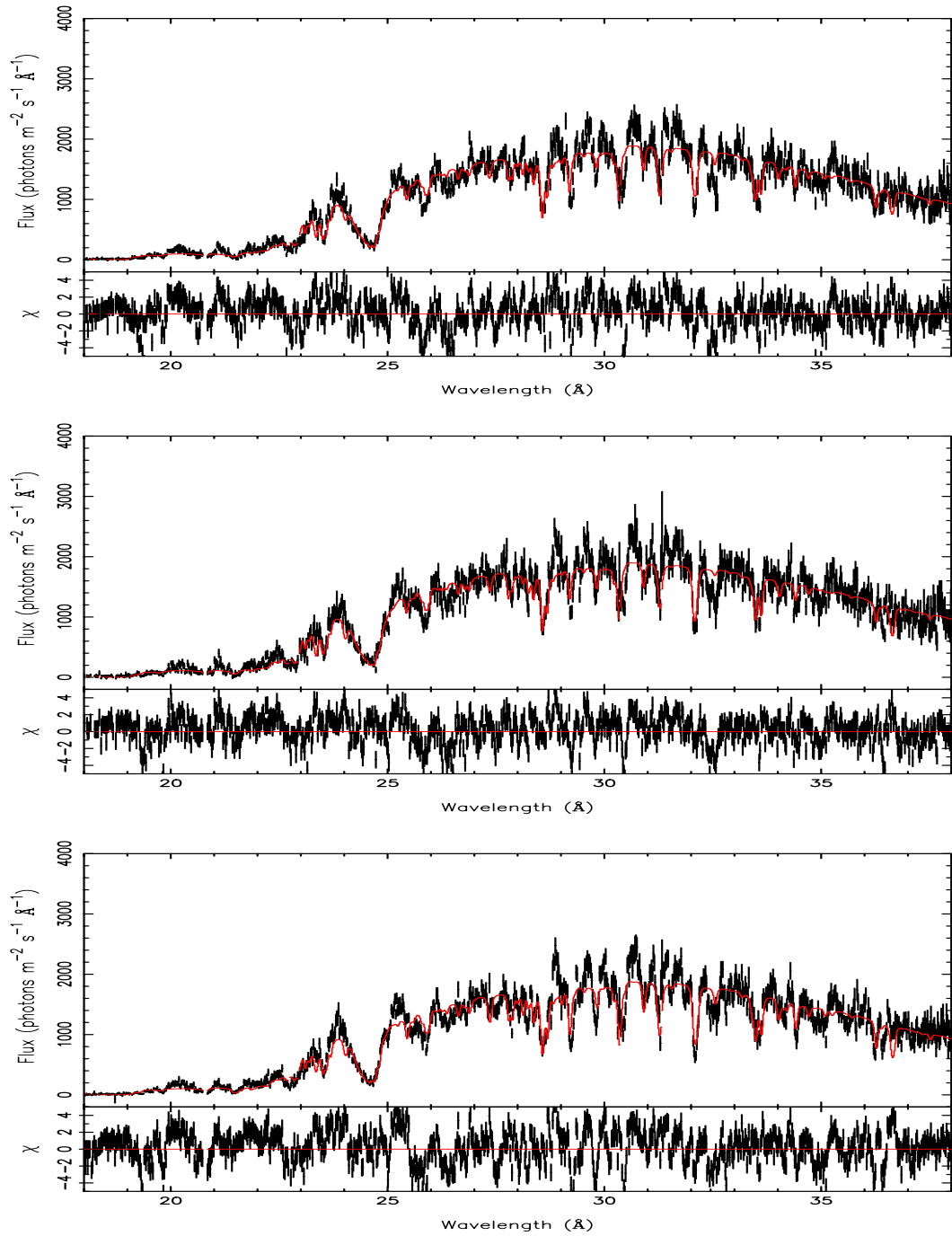


Figure 5.4: RGS1 flux spectra of V4743 Sgr low region fitted with the composite model. Top panels show the plots bl1 on top, pl in the middle and bl2 spectra at the bottom.

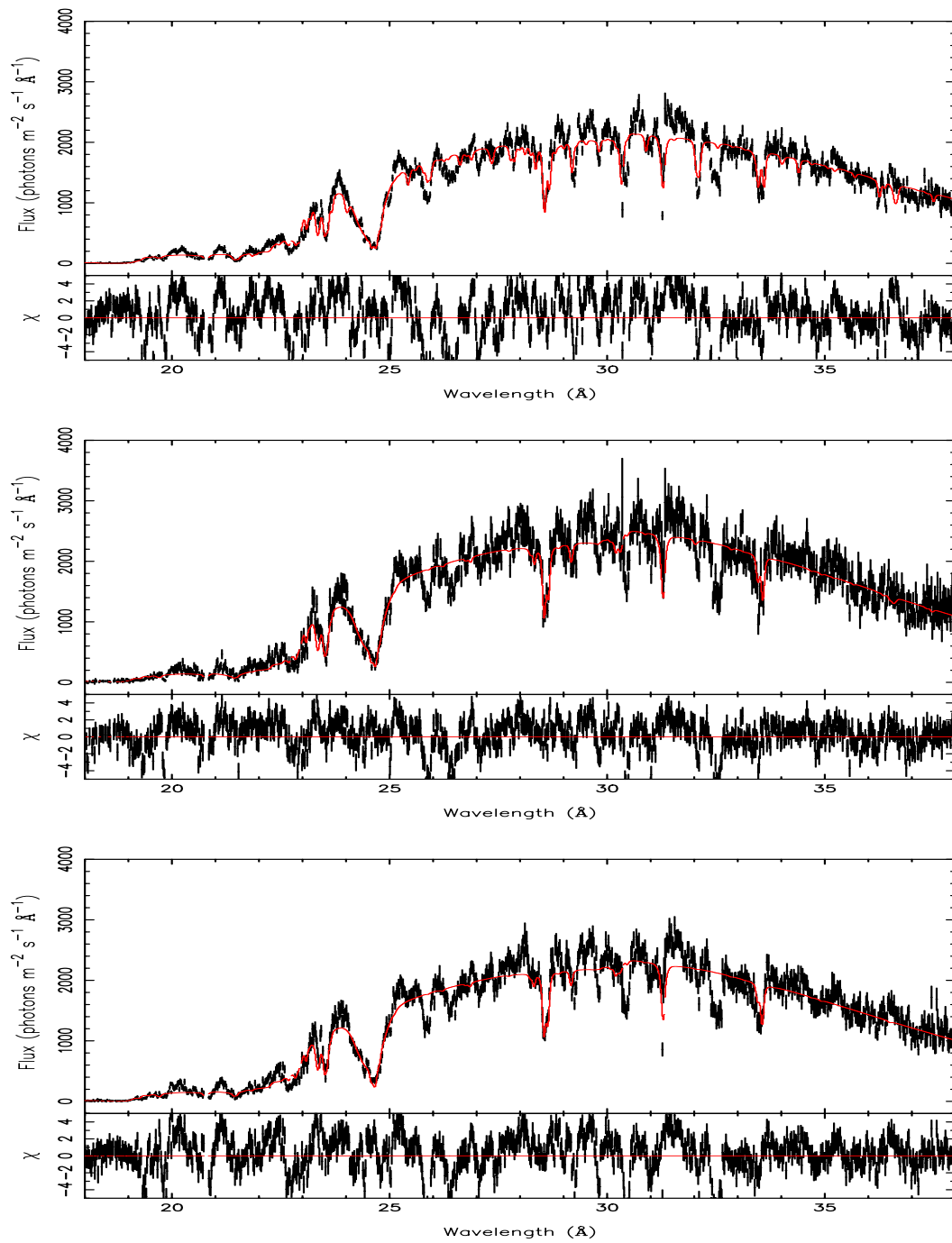


Figure 5.5: RGS1 flux spectra of V4743 Sgr valley and high region fitted with the composite model. The top panel shows the valley while the high-peak is in the middle and high-bottom is at the bottom.

271-814 eV except for the high region where the N_H becomes $\simeq 594.2-794.1 \times 10^{21}$ cm^{-2} while effective temperature goes to 879-1390 eV. However, the rms velocities $\simeq 40 \text{ km s}^{-1}$ and blueshifts 974-2190 km s^{-1} are consistent among the spectra.

V4743 Sgr shows a typical signature of H-burning with under-abundant carbon $C=0.2-0.9$, and enhanced nitrogen $N=48-71$ and oxygen $O=1.2-14$ (all ratios to solar abundances). However, The nitrogen abundance in the valley goes up to 125 and oxygen to 46. The abundances of the other elements are kept between 0.01 to 3 and the results can be seen in Table 5.2. Total molecular density of the O_2 drops from $3.8-5.7 \times 10^{17}$ cm^{-2} (in the first region) to $2.8-4.5 \times 10^{17}$ cm^{-2} (low and high regions).

The χ^2 values differ from region to region and ranges between 2.1-7.5. The composite model consists of two warm absorbers with different temperatures, column densities and corresponding rms velocities, and one hot absorber. It indicates that there are three different absorption regions. When we investigate the spectra throughout the observation one of the warm absorbers $xabs_2$ stays consistent. In the other, the parameters N_H and $\text{Log}(\xi)$ seem to change from the first region to others. Similarly, a change in the hot model hydrogen column density and in the effective temperature can be seen in the high region. The long term variability can be explained with these instabilities in the absorbers. Periodic variability has yet to be concluded.

Table 5.2: Spectral parameters obtained from best fitted composite model of V4743 Sgr RGS spectra from the blue region. The errors are calculated with 90% confidence level for one degree of freedom. The below spectra are given in ascending time order.

Model	Parameter	b1	p1	b2	p2	b3	p3
bb	Norm (10^{20} cm^{-2})	$1.05^{+2.7}_{-0.2}$	$1.09^{+1.02}_{-0.01}$	$1.19^{+2.6}_{-0.02}$	$1.21^{+1.17}_{-0.22}$	$1.12^{+1.19}_{-0.05}$	$1.10^{+0.82}_{-0.06}$
	kT (eV)	44^{+1}_{-4}	$45^{+0.1}_{-2}$	$44^{+0.1}_{-3}$	45^{+1}_{-2}	44^{+1}_{-2}	$45^{+0.1}_{-1.8}$
	L ($10^{38} \text{ erg s}^{-1}$)	1.3	1.6	1.4	1.9	1.4	1.6
xabs ₁	N_H (10^{21} cm^{-2})	$0.73^{+27.15}_{-0.28}$	$1.31^{+7.16}_{-0.50}$	$0.70^{+9.91}_{-0.10}$	$0.62^{+16.57}_{-0.10}$	$0.79^{+5.12}_{-0.25}$	$0.82^{+4.37}_{-0.33}$
	Log(ξ) (erg cm s^{-1})	$3.5^{+0.5}_{-0.1}$	$3.5^{+0.3}_{-0.1}$	$3.5^{+0.5}_{-0.1}$	$3.5^{+0.5}_{-0.1}$	$3.5^{+0.3}_{-0.1}$	$3.6^{+0.3}_{-0.1}$
	σ_v (km s^{-1})	3090^{+196}_{-179}	3190^{+180}_{-163}	3070^{+258}_{-206}	2965^{+182}_{-166}	3071^{+152}_{-143}	3043^{+154}_{-145}
	zV (km s^{-1})	-3116^{+197}_{-207}	-2965^{+182}_{-187}	-3050^{+243}_{-251}	-2864^{+193}_{-191}	-3030^{+162}_{-168}	-2829^{+163}_{-166}
xabs ₂	N_H (10^{21} cm^{-2})	$0.33^{+0.08}_{-0.05}$	$0.23^{+0.08}_{-0.06}$	$0.23^{+0.08}_{-0.19}$	$0.24^{+0.09}_{-0.06}$	$0.22^{+0.08}_{-0.05}$	$0.20^{+0.08}_{-0.05}$
	Log(ξ) (erg cm s^{-1})	$1.8^{+0.2}_{-0.1}$	$1.8^{+0.2}_{-0.2}$	$1.8^{+0.3}_{-0.2}$	$1.8^{+0.2}_{-0.2}$	$1.8^{+0.2}_{-0.2}$	$1.7^{+0.2}_{-0.2}$
	σ_v (km s^{-1})	104^{+17}_{-16}	147^{+19}_{-34}	89^{+19}_{-16}	88^{+18}_{-15}	74^{+13}_{-12}	89^{+13}_{-13}
	zV (km s^{-1})	-2593^{+76}_{-85}	-2398^{+58}_{-122}	-2415^{+84}_{-97}	-2442^{+82}_{-101}	-2419^{+62}_{-83}	-2470^{+67}_{-85}
hot	N_H (10^{21} cm^{-2})	$10.9^{+12.0}_{-9.9}$	$71.3^{+12.5}_{-13.2}$	$24.9^{+10.3}_{-21.1}$	$31.4^{+9.8}_{-8.8}$	$32.0^{+9.9}_{-8.7}$	$55.3^{+9.9}_{-10.4}$
	kT (eV)	596^{+296}_{-258}	410^{+24}_{-24}	653^{+161}_{-358}	382^{+25}_{-28}	367^{+23}_{-27}	401^{+19}_{-21}
	σ_v (km s^{-1})	< 63	< 46	< 41	< 36	< 33	< 34
	zV (km s^{-1})	-1523^{+171}_{-335}	-2187^{+115}_{-98}	-1643^{+119}_{-116}	-1570^{+100}_{-91}	-1557^{+86}_{-62}	-1483^{+95}_{-89}
hot-ism	N_H (10^{21} cm^{-2})	$1.42^{+0.54}_{-0.01}$	$1.49^{+0.20}_{-0.01}$	$1.43^{+0.28}_{-0.01}$	$1.54^{+0.17}_{-0.09}$	$1.45^{+0.16}_{-0.02}$	$1.51^{+0.14}_{-0.01}$
	kT (eV)	$0.83^{+0.58}_{-0.33}$	$0.86^{+0.42}_{-0.36}$	$0.83^{+0.47}_{-0.33}$	$1.17^{+0.12}_{-0.67}$	$0.95^{+0.25}_{-0.45}$	0.85^{\pm}
amol	O_2 (10^{17} cm^{-2})	$4.3^{+0.4}_{-0.5}$	$5.1^{+0.6}_{-0.5}$	$5.1^{+1.1}_{-0.4}$	$4.8^{+0.4}_{-0.5}$	$5.2^{+0.4}_{-0.4}$	$4.5^{+0.4}_{-0.4}$
	χ^2_ν	2.1	2.1	2.3	2.3	2.3	2.4
	(d.o.f.)	942	960	947	948	973	974

Table 5.3: Spectral parameters obtained from best fitted composite model of V4743 Sgr RGS spectra from the red, green and yellow region. The errors are calculated with 90% confidence level for one degree of freedom. The below spectra are given in ascending time order.

Model	Parameter	bl1	pl	bl2	valley	hp	hb
bb	Norm (10^{20} cm^{-2})	$1.27_{-0.07}^{+0.38}$	$0.54_{-0.03}^{+0.56}$	$1.09_{-0.07}^{+0.22}$	$0.59_{-0.01}^{+0.26}$	$3.59_{-0.50}^{+1.03}$	$3.47_{-0.02}^{+0.06}$
	kT (eV)	$44_{-1}^{+0.1}$	$48_{-2.6}^{+0.2}$	$45_{-1}^{+0.3}$	$48_{-1}^{+0.1}$	$43_{-1}^{+0.2}$	$44_{-0.2}^{+0.1}$
	L ($10^{38} \text{ erg s}^{-1}$)	1.6	1.1	1.5	1.2	3.9	4.1
xabs ₁	N_H (10^{21} cm^{-2})	$3.33_{-0.4}^{+3.7}$	$17.3_{-3.6}^{+8.1}$	$74.1_{-6.8}^{+9.2}$	$27.0_{-2.5}^{+3.9}$	$1.33_{-0.27}^{+13}$	$5.5_{-0.4}^{+4.6}$
	Log(ξ) (erg cm s^{-1})	$3.8_{-0.1}^{+0.1}$	$4.0_{-0.1}^{+0.1}$	$4.3_{-0.1}^{+0.1}$	$4.2_{-0.1}^{+0.1}$	$3.6_{-0.1}^{+0.3}$	$3.9_{-0.1}^{+0.1}$
	σ_v (km s^{-1})	2754_{-124}^{+172}	2773_{-125}^{+132}	2307_{-89}^{+94}	2865_{-66}^{+67}	2877_{-379}^{+467}	2880_{-151}^{+149}
	zv (km s^{-1})	-3170_{-152}^{+192}	-3065_{-150}^{+147}	-3372_{-126}^{+114}	-3198_{-80}^{+78}	-2907_{-539}^{+439}	-2920_{-169}^{+170}
xabs ₂	N_H (10^{21} cm^{-2})	$0.25_{-0.06}^{+0.08}$	$0.48_{-0.06}^{+0.08}$	$0.27_{-0.07}^{+0.08}$	$0.19_{-0.09}^{+0.07}$	$0.37_{-0.09}^{+0.56}$	$0.25_{-0.06}^{+0.07}$
	Log(ξ) (erg cm s^{-1})	$1.4_{-0.1}^{+0.1}$	$1.7_{-0.1}^{+0.1}$	$1.4_{-0.1}^{+0.1}$	$1.7_{-0.1}^{+0.1}$	$1.7_{-0.4}^{+0.6}$	$1.8_{-0.1}^{+0.2}$
	σ_v (km s^{-1})	105_{-14}^{+13}	93_{-9}^{+9}	109_{-9}^{+9}	100_{-5}^{+5}	88_{-30}^{+34}	76_{-11}^{+10}
	zv (km s^{-1})	-2280_{-57}^{+55}	-2251_{-52}^{+43}	-2227_{-37}^{+27}	-2353_{-39}^{+24}	-2455_{-170}^{+161}	-2503_{-70}^{+57}
hot	N_H (10^{21} cm^{-2})	$21.8_{-3.0}^{+3.8}$	$60.5_{-8.7}^{+8.9}$	$21.79_{-2.6}^{+3.2}$	$40.5_{-3.2}^{+3.1}$	$603.2_{-9.0}^{+8.8}$	$788.4_{-5.9}^{+5.7}$
	kT (eV)	291_{-12}^{+15}	381_{-19}^{+17}	281_{-10}^{+11}	361_{-8}^{+9}	980_{-101}^{+128}	1285_{-93}^{+105}
	σ_v (km s^{-1})	37_{-4}^{+4}	40_{-6}^{+6}	54_{-5}^{+5}	20_{-4}^{+4}	< 38	< 28
	zv (km s^{-1})	-1108_{-40}^{+30}	-1075_{-26}^{+29}	-1000_{-26}^{+17}	-1168_{-13}^{+16}	1424_{-55}^{+57}	1559_{-45}^{+51}
hot-ism	N_H (10^{21} cm^{-2})	$1.53_{-0.01}^{+0.07}$	$1.36_{-0.01}^{+0.19}$	$1.49_{-0.01}^{+0.05}$	$1.38_{-0.01}^{+0.08}$	$1.64_{-0.02}^{+0.08}$	$1.63_{-0.01}^{+0.02}$
	kT (eV)	$0.76_{-0.26}^{+0.22}$	$0.5_{-0.75}^{+0.75}$	$0.79_{-0.29}^{+0.17}$	$0.83_{-0.33}^{+0.19}$	$0.5_{-0.5}^{+0.5}$	$0.83_{-0.18}^{+0.10}$
amol	O_2 (10^{17} cm^{-2})	$3.2_{-0.3}^{+0.3}$	$4.1_{-0.4}^{+0.4}$	$3.1_{-0.3}^{+0.3}$	$3.5_{-0.2}^{+0.2}$	$3.1_{-0.30}^{+0.32}$	$3.0_{-0.2}^{+0.2}$
	χ^2_ν	3.4	2.7	3.9	7.5	3.2	4.8
	(d.o.f.)	958	956	964	966	950	965

CHAPTER 6

KT ERIDANI

KT Eridani was discovered by Itagaki K. with a visual magnitude 8.1 mag on November 25, 2009, after its maximum-light [61]. The study on the earlier observations revealed that it was in outburst on November 14, 2009, with a visual magnitude 5.4 mag. Hence, November 14 was taken as the $t=0$ day [62, 63, 64]. Similar to our previous classical novae discussed in Chapter 4 and Chapter 5, the corresponding nova is fast with $t_2=6.6$ and $t_3=13.6$ days [65]. The optical spectroscopy of KT Eri revealed broad Balmer series with some other significant emission lines (e.g.; HeI, NIII), and the FWHM of H_α emission was ~ 3400 km s [66]. The nova is classified as He/N nova [66, 67].

Jurdana-Šepić et al.[68] identified the progenitor of the KT Eri by studying the historical light curves. The progenitor has been considered to be a hot star with circumstellar material. The magnitude of the progenitor system was measured as $\langle B \rangle = 14.2 \pm 0.4$ in its quiescent phase, and two periods were measured as 737 and 376 days. 737 days variability is considered to be the orbital period of the binary system. The long periodicity implies that the system has a high inclination angle ($l = 207.986, b = -32.02$), and the companion is an evolved star [68, 69]. The mass of the white dwarf is estimated between $1.1 M_\odot < M_{WD} < 1.3 M_\odot$ [68, 70]. The nova is considered as a recurrent nova candidate, but no outburst was observed previously [68, 71, 72].

There are several observations of KT Eri in X-ray from *Swift* to *Chandra* [63, 73, 74]. The rise in X-ray emission can be seen in the *Swift* observations. The hard X-ray emission started around 39.9 days after t_0 . It softened around day 60 (BB kT ~ 33 eV). The count rate was highly variable until X-ray emission reaches its maximum. Then, the variability became smaller, but the count rate resided above $100 \text{ counts s}^{-1}$

Table 6.1: *Chandra* HRC-S+LETG observations of KT Eridani

Target	Instrument	Date (UT)	ObsID	Day ^a	Exp. time ^b ks	C.R. ^c cts s ⁻¹
KT Eri	HRC-S+LETG	2010-01-23	12097	71.3	14.95	13.1
		2010-01-31	12100	79.3	2.75	72.5
		2010-02-06	12101	84.6	3.52	50
		2010-04-21	12203	158.8	3.21	96.5

Notes: ^a After the optical-maximum, t_0 ; ^b Dead time corrected exposure time; ^c Mean count rate per second.

[63, 75]. Meanwhile, *Chandra* observed KT Eri firstly 71.3 days after the optical-maximum with an average count rate around 13 counts s⁻¹ [73, 76]. Three other observations were held on 79.3, 84.6 and 158.8 days after the initial outburst [76]. The X-ray spectrum of KT Eri corresponds to a bright super soft source (SSS) and resembles V4743 Sgr with its deep absorption features. In the timing analysis of the *Swift* data, 35 s periodicity is detected [74], and *Chandra* confirmed the periodicity [76]. The similar short-term oscillation is also found in the RS Oph during its SSS phase [77]. The modulation is considered to be caused by the white dwarf pulsation rather than the rotation [74].

The reddening was estimated as $E(B-V) \sim 0.08$ from the equivalent width of the NaI D1 line of the interstellar medium [78]. The initial distance estimations yield 6.5 kpc [78]. However, recent distance studies by GAIA indicate that actual value might be smaller, ~ 3.7 kpc [43]. The column density for the interstellar matter is given as $N_H = 6.13 \times 10^{20}$ cm⁻² by NASA's heasarc N(H) tool and $N_H = 5.25 \times 10^{20}$ cm⁻² by *nhtot*. Ness et. al X-ray studies of KT Eri indicate twice as a higher value [73].

6.1 Observations and data

The information on KT Eri observations by *Chandra* HRS-C+LETG is given in Table-6.1. The on times were rather short, 15.2 ks for the first and 5.1 ks for the other observations. It is reported that the count rates for day 79.3 and 158.8 were high, saturating telemetry. All events could not be telemetered. As a result, the dead time

corrected exposures are even shorter.

The high-resolution spectra are extracted from *Chandra* HRC-S+LETG by using its X-ray analysis software CIAO (version 4.11) and its main analysis tasks, e.g. *chandra-repro*. The calibration package CALDB 4.8.2 is used. The first order ancillary response files (arf) and grating redistribution matrix files (rmf) are obtained. HRC-S does not differentiate higher spectral orders, only gives positive and negative order spectra. We combined the +1 and -1 order spectra by using *combine-grating-spectra*. The data are binned to match the instrumental resolution, 0.05 Å.

6.2 Analysis and Results

The background subtracted light curves are extracted from the event files by using *dmextract*. The data for all the observations are binned by 50 s for visual purposes, Figure-6.1. The count rate highly varies during all the observations in short time scale, even in between the subsequent observations. The mean count rate on day 71.3 is 13.1 counts s⁻¹ and it varies between 5-25 counts s⁻¹. On day 79.3, the mean count rate rises to 72.5 counts s⁻¹, and on day 84.3, it drops to 50 counts s⁻¹. In these three light curves, there are no indication for a periodic variability. In the timing analysis done by Ness et al., the periodic variability is not detected except for the day 158.8 [76]. There is 35 s variability in the last observation. The mean count rate is also the highest with the value around 96.5 counts s⁻¹.

The spectra are that of a bright SSS. The continuum emission is produced by the WD atmosphere, and in all four spectra it is in the wavelength range between 19Å and 60Å with varying fluxes. The spectral evolution is given in Figure-6.2. The change in the line profiles and the continuum is clear. On the days 71.3 and 84.6, the emission starts around 22Å, and the flux is relatively lower than the other observations. The fluxes are 0.87×10^{-9} erg s⁻¹ cm⁻², 5.5×10^{-9} erg s⁻¹ cm⁻², 3.6×10^{-9} erg s⁻¹ cm⁻² and 7.7×10^{-9} erg s⁻¹ cm⁻² from the first to last observation respectively.

Especially, the observed spectra revealed a strong emission line between 28.5-29.2Å in two observations 12097 and 12101. It is considered as redshifted NVI emission line by a factor of 1500 km/s for the observation on day 71.3[73]. The NVI emission

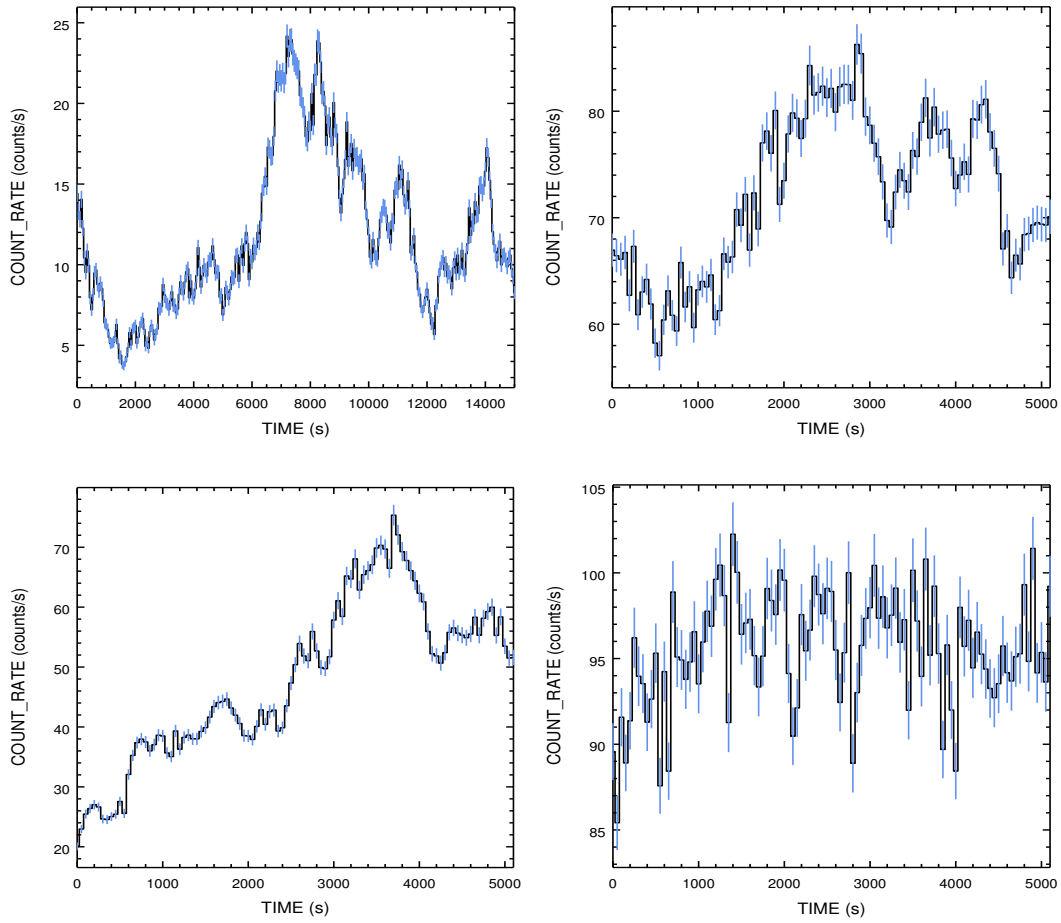


Figure 6.1: The background subtracted light curves of KT Eri on days 71.3, 79.3, 84.6 and 158.8. The data are measured with HRC-S camera as zero-order and are binned with 50 s in all observations. The x-axis shows the on time of the detector.

line is seen in all observations but it is weaker on days 79.3 and 158.8. On days 79.3 and 158.8 while the emission line around 29\AA subsides another emission line around 25\AA increases by a substantial amount. There are several other emission lines. Most of the observed emission lines are in the wavelength band $\sim 25\text{-}30\text{\AA}$. The origin of these emission lines are unknown but they considered to be transient in nature [79].

Our fit yields two gaussian lines for the emission profile for this observation; one is at 28.8\AA and the other is at 29.02\AA with a full width half maximum (FWHM) is around 0.15 and 0.25, broader than the instrumental line broadening function, respectively. The origin and characteristic of this emission is unknown as mentioned previously

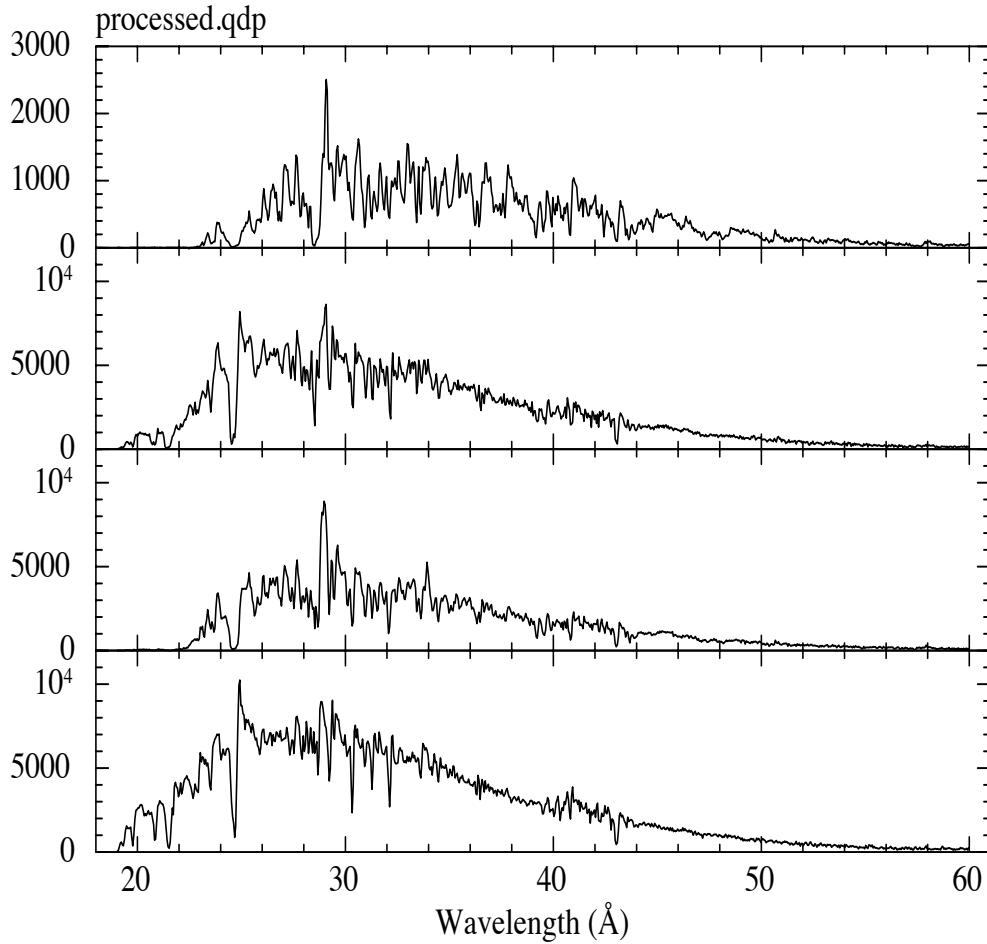


Figure 6.2: KT Eri *Chandra* HRC-S+LETG spectra of 71.3, 79.3, 84.6 and 158.8 days after the outburst from top to bottom respectively. All panels show the flux spectrum between 19\AA and 60\AA in the units of $\text{counts s}^{-1} \text{m}^{-2} \text{\AA}^{-1}$. The flux in day 71.3 is lower than the other three observations, hence the flux range is different than the rest.

and some of the characteristics are given in [73]. The emission line of the second observation, 84.6 days after the outburst, can be modelled by one gauss line profile at 29.08 Å again with a broader line profile than the instrumental broadening.

Deep absorption lines are also present in the spectra. Nitrogen lines around 25Å, 29Å and carbon line around 34Å can be clearly seen in Figure-6.2. The broadening and the strength of the absorption lines varies along the observations. On days 79.3 and 158.8 the deep broad absorption profile around 28.2Å is less observable. The absorption line like N around 25Å kept its depth, it is probably originated in the photosphere of the WD. The estimated blueshift for the lines are -2500 km s^{-1} on day 71.3 [73].

Additionally, several absorption lines are seen at their rest wavelength in the subsequent observations of KT Eridani. The similar lines are present in most of the X-ray spectra of novae, such as our previous sources V2491 Cyg and V4743 Sgr. The features, that are seen in the *Chandra* spectra, are due to OI (23.508 Å), NI (31.28 Å) and CII - CIII around 42-43 Å . It is indicated that, whenever there is a bright X-ray source acting as a backlight these lines are observed and not typical of novae. Hence, these absorption lines are considered to be produced in the interstellar medium (ISM). The O K-edge presented in the 22.8 Å is also observed in all spectra.

The spectrum on day 84.6 resembles the spectrum of nova SMC 2016 39 days after its outburst and almost matches the spectrum of V4743 Sgr on day 180 [80, 79]. The later observations of SMC 2016 again almost have the similar spectral shapes with the spectra of days 79.3 and 158.8, which gives us some clues about the observed lines and their blueshifts.

We constructed the composite model by using one warm plasma absorber *xabs* and one *hot* absorber upon *bb* continuum. One cold plasma component *hot* with low temperature and one dust component *amol* are added to the composite model to include ISM effects. In summary, the best results are obtained with [Amol x ISM x hot x xabs x bb]. We tried several other combination of the models, but fits did not yield any conclusive results. In most of the cases, the oxygen abundances yielded very high values. We could not able to model any emission profile, the available models are limited. As we discussed previously, we are also missing some photospheric absorption profiles but we could able to see the affects of the absorbers on the observed

Table 6.2: *Chandra* HRC-S+LETG KT Eri best model fit parameters. The errors are calculated with %90 confidence level for one degree of freedom.

Model	Parameters	12097	12100	12101	12203
BB	Norm (10^{20}cm^2)	$0.34^{+0.01}_{-0.01}$	$0.42^{+17.4}_{-0.01}$	$0.14^{+0.04}_{-0.03}$	$0.19^{+0.26}_{-0.01}$
	kT (eV)	$60.2^{+0.3}_{-0.3}$	$80.4^{+0.6}_{-16.2}$	$81.2^{+2.1}_{-0.9}$	78.6^{+1}_{-8}
	L(10^{38}erg s^{-1})	2.4	12.9	4.6	5.4
XABS	N_H (10^{24}cm^{-2})	$0.21^{+0.03}_{-0.02}$	$1.40^{+4.5}_{-1.36}$	$0.16^{+0.01}_{-0.01}$	$0.65^{+0.02}_{-0.61}$
	Log ξ (erg cm s^{-1})	$3.03^{+0.01}_{-0.02}$	$3.14^{+0.01}_{-0.01}$	$2.8^{+0.01}_{-0.01}$	$3.04^{+0.01}_{-0.01}$
	σ_v (km s^{-1})	1402^{+82}_{-29}	703^{+14}_{-16}	1089^{+21}_{-21}	387^{+9}_{-9}
	z_v (km s^{-1})	-2285^{+144}_{-109}	-2372^{+30}_{-531}	-1814^{+39}_{-49}	-1383^{+21}_{-21}
HOT	N_H (10^{24}cm^{-2})	$2.43^{+0.02}_{-0.02}$	$2.14^{+2.6}_{-2.1}$	$2.33^{+0.19}_{-0.43}$	$1.74^{+0.03}_{-1.03}$
	kT (keV)	$0.23^{+0.01}_{-0.01}$	$0.29^{+0.05}_{-0.06}$	$0.25^{+0.01}_{-0.01}$	$0.43^{+0.03}_{-0.01}$
	σ_v (km s^{-1})	32^{+6}_{-7}	< 10	< 10	< 10
	z_v (km s^{-1})	-863^{+11}_{-29}	-677^{+1}_{-1}	-778^{+7}_{-5}	-793^{+11}_{-11}
ISM	N_H (10^{20}cm^{-2})	$2^{+4.5}_{-1.3}$	$5.2^{+3.7}_{-1.8}$	$2.0^{+0.1}_{-0.1}$	$6.8^{+2.1}_{-0.1}$
AMOL	O_2 (10^{17}cm^{-2})	$37.2^{+1.6}_{-6.2}$	$3.4^{+0.1}_{-0.1}$	$21.6^{+0.5}_{-0.8}$	$0.8^{+0.1}_{-0.1}$
	χ^2_ν	32.1	16.8	13.6	11.9
	(d.o.f.)	(732)	(791)	(807)	(796)

spectra. The spectra and the best fit model are given in Figure-6.3 and Figure-6.4.

We first tried to fit the first and the last observation in which the count rates are the lowest and the highest respectively. We coupled the abundances of the warm and hot absorbers, and we kept them fixed during all observations. We assumed the elemental abundances should be the same within 15 days and on day 158.6 since the spectral shape did not change dramatically. We also searched for the elemental abundances of C, N and O in the cold gas and kept them fixed for all other observations. The best fit model parameters are given in Table-6.2, and the elemental abundances in Table-6.3.

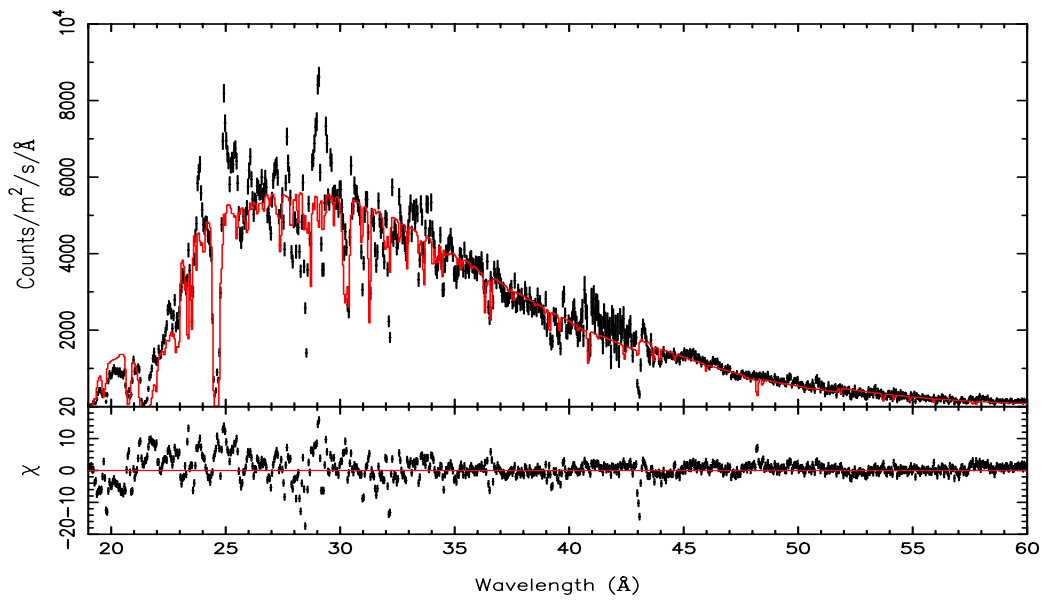
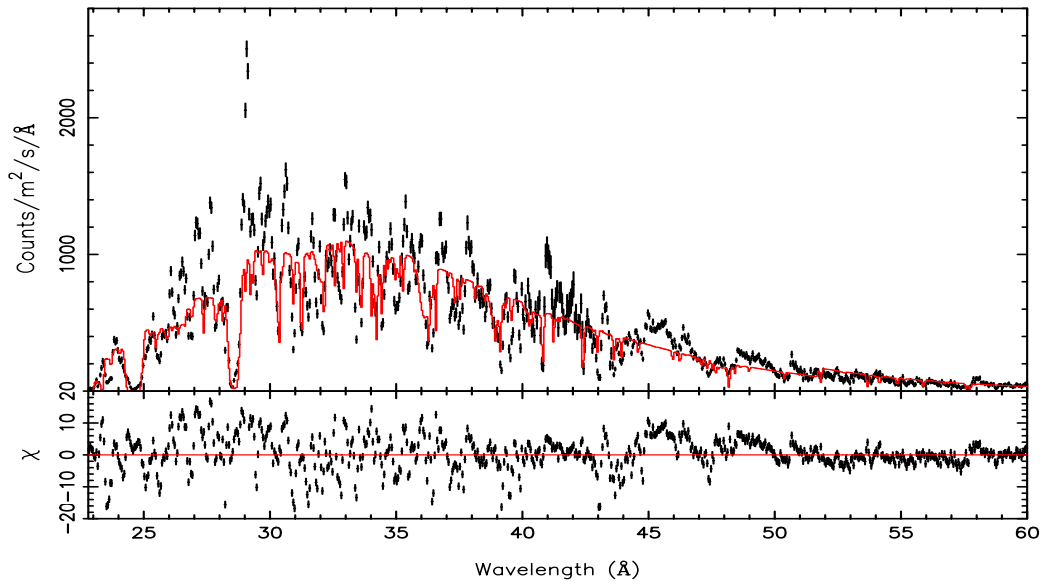


Figure 6.3: The HRC-S+LETG flux spectra of KT Eri on 71.3 and 79.3 days. The best fit model is indicated with the red line.

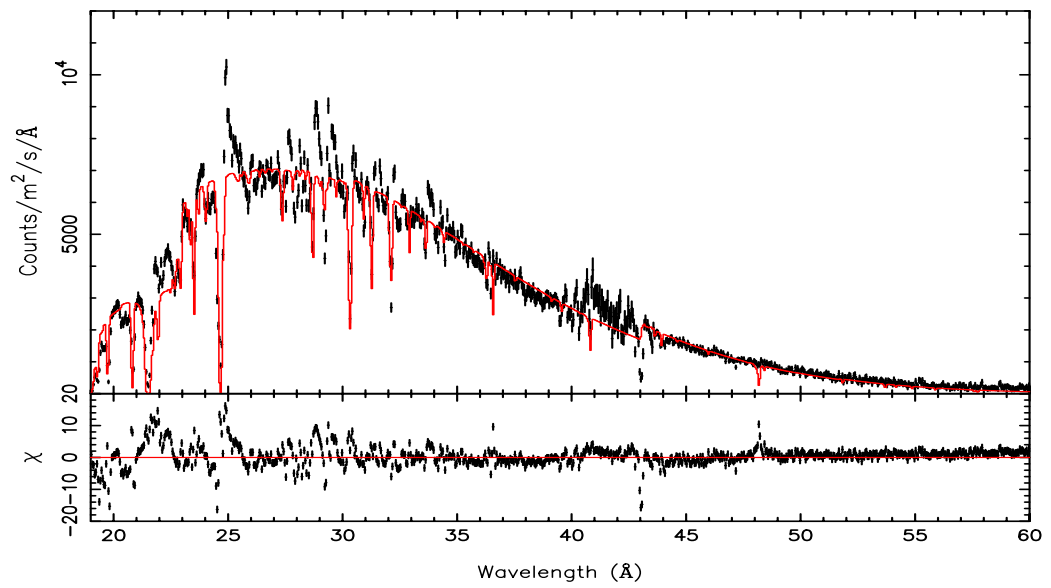
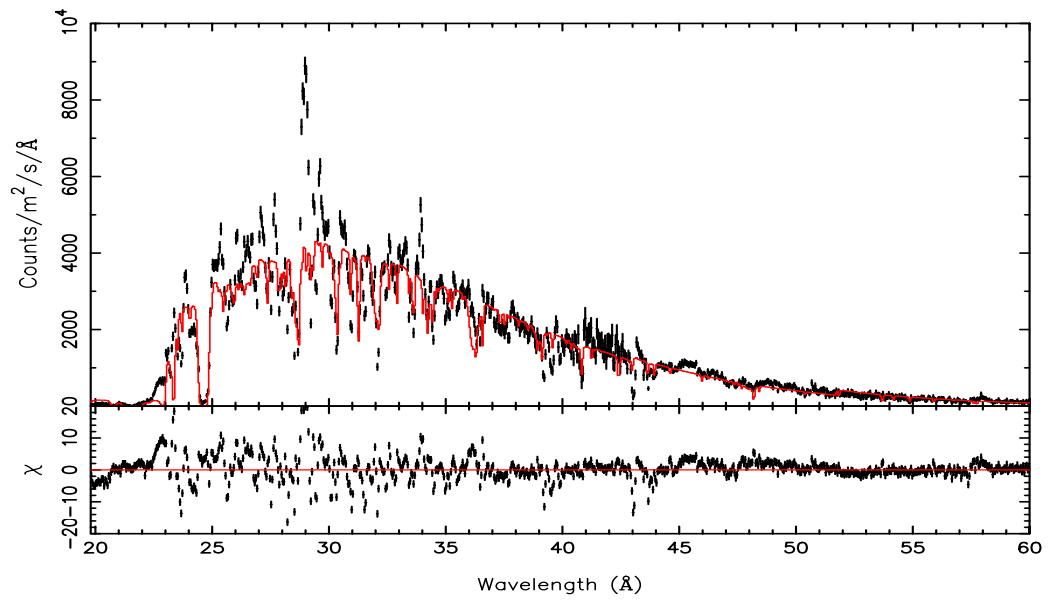


Figure 6.4: The HRC-S+LETG flux spectra of KT Eri on 84.6 and 158.8 days. The best fit model is indicated with the red line.

Table 6.3: Elemental abundances obtained with a composite model includes one hot and one warm absorber. The values are given relative to the solar abundances that are explained in the text.

Abundances	KT Eri
C	$0.01^{+0.001}_{-0.006}$
N	$0.8^{+0.1}_{-0.1}$
O	$29.8^{+227}_{-1.2}$
Mg	$0.02^{+0.01}_{-0.01}$
S	$0.04^{+0.01}_{-0.01}$

6.3 Discussion

We expected that the change in the observed spectrum will manifest itself in the differences in the spectral parameters either in the absorber component or in the stellar emission. The normalisation factor for the blackbody ranges from $0.14 \times 10^{20} \text{ cm}^2$ to $0.42 \times 10^{20} \text{ cm}^2$. The corresponding WD radius can be estimated to be between $1.1 \times 10^9 \text{ cm}$ and $1.8 \times 10^9 \text{ cm}$. The calculated white dwarf radii are high when one considers the bloated WD radius to be around $1 \times 10^9 \text{ cm}$. The one probable cause for this can be the fact that we could not able to model the emission profile. It may be originated in a plasma far away from the stellar emission and may affect the overall spectrum. Other probable cause is that we are using a simple blackbody model that overestimates the radius and luminosities.

The effective temperature of the blackbody is 59.9-60.5 eV on day 71.3 which is higher than the earlier estimated value $\sim 37.9 \text{ eV}$ for the same observation [73]. The blackbody temperatures are estimated as 64.2-81 eV on day 79.3, 80.3-83.3 eV on day 84.6 and 70.6-79.6 eV on day 158.8. The increase in the temperature and a possible shrinking of the WD atmosphere surface may explain the increase in fluxes relative to the first observation. In the case of observation 12100, we obtained the highest normalisation value probably due to compensate a higher absorption within the warm plasma. They are highly coupled. Orio et al. estimated the effective temperature to be around 60 eV in their primitive analysis of KT Eri on day 84.6[80]. The value is

lower than the one in our calculations on the same day, but close to the temperature of the first observation.

The emission lines can either be originated in the collisionally ionized plasma or photoionized plasma. We tried to model the emission profiles with the collisionally ionized plasma model, however it did not give any reasonable results. The inconclusive results are either due to the incapability of the complex model we used or the difference in the origin of the emissions. The emissions can be originated from the photoionized plasma rather than the collisionally ionized plasma as discussed in the case of Nova SMC 2016 [80].

We experimented with an interstellar matter absorption model *ismabs* [81]. The authors who created the model worked with all *Chandra* HRC-S+LETG spectra of KT Eri to improve their models. In the mean time, they provided well fitted ISM CII-CIII lines around 42-43 Å. The model is constructed for the XSPEC analysis package but it can be included as a user defined model in the SPEX version 3.03.0. We considered that the use of this ISM model can improve our model fits. We could successfully implemented the model, but the complexity of our composite model makes it impossible to work with *ismabs*. We could not get any conclusive results.

The best fit model yielded two plasma component, one photoionized warm absorber and one collisionally ionized hot absorber. The column densities for the warm absorber are estimated in the range $0.16-1.40 \times 10^{24} \text{ cm}^{-2}$. The ionization parameter $\text{Log}\xi$ changes between 2.7 to 3.15. The absorber velocities are calculated as $\sim -2300 \text{ km s}^{-1}$, $\sim -2400 \text{ km s}^{-1}$, $\sim -1800 \text{ km s}^{-1}$ and $\sim -1400 \text{ km s}^{-1}$ from first to last observation. The absorbers are slowing down in time. The velocity of the warm absorber in the first observation is in good agreement with the earlier blueshift estimations of the absorber lines [73]. When we consider the resembles of the spectrum of KT Eri on day 84.6 and Nova SMC 2016 on day 39, -1800 km s^{-1} velocity of the photoionized absorber is also in good agreement [80]. We can conclude that the blueshifts in the absorber lines are correlated with the velocity of the warm plasma within the binary system.

The collisionally hot plasma column density is $(2.43 \pm 0.02) \times 10^{24} \text{ cm}^{-2}$ in first observation. It drops to $2.14_{-2.1}^{+2.6} \times 10^{24} \text{ cm}^{-2}$ on day 79.3 and increases to $2.33_{-0.43}^{+0.19} \times 10^{24}$

cm^{-2} on day 84.6. Finally, the column density becomes $1.74_{-1.03}^{+0.03} \times 10^{24} \text{ cm}^{-2}$ in the last observation. The plasma temperature is in the range 230-430 eV, and velocities are between 676 km s^{-1} and 874 km s^{-1} .

We used cold gas+dust model assumption for the ISM similarly to our previous works. The hydrogen column density of the ISM fluctuates between $2 \times 10^{20} \text{ cm}^{-2}$ to $6.8 \times 10^{20} \text{ cm}^{-2}$ along the observations. We also tried to obtain the elemental abundances of N, O and C as the corresponding lines are seen in the spectra. The elemental abundance of nitrogen is close to the solar abundance while we found carbon $C/C_{\odot}=1.32-1.41$ and oxygen $O/O_{\odot}=2.22-2.41$ overabundant. The real difference lies in the column density of O_2 of the dust component where we model the O K-edge. On the day 71.3 and 84.6 the column density of O_2 are $36-38.8 \times 10^{17} \text{ cm}^{-2}$ and $20.8-22.1 \times 10^{17} \text{ cm}^{-2}$. On the higher count rate observations on day 79.3 and 158.8 the column density drops to $3.3-3.5 \times 10^{17} \text{ cm}^{-2}$ and $0.7-0.9 \times 10^{17} \text{ cm}^{-2}$.

We determined that the heavier elements like Si, Ar, Ca and Fe are underabundant in general ~ 0.01 . The magnesium and sulfur is also underabundant $\text{Mg}/\text{Mg}_{\odot}=0.01-0.03$, $\text{S}/\text{S}_{\odot}=0.03-0.05$. The carbon abundance is estimated as $C/C_{\odot} \approx 0.01$. The nitrogen abundance from the best fit resulted as $\text{N}/\text{N}_{\odot}=0.6-0.9$. We found oxygen to be $O/O_{\odot}=28.6-256.8$. We mentioned that the abundances were obtained from the best fit model of one of the observations (12203) and were kept fixed in all other spectral analysis. Actually, the abundances slightly change within the observations. In some cases during the search for the parameter extensions, the oxygen abundance increase substantially. The high upper limit for the oxygen abundance may be caused by the absence of the photospheric absorptions.

The ξ_{ν}^2 values obtained from the best fits are rather high, Table-6.2. Especially in the first region where the emission profiles are comparably more dominant. The change in the stellar remnant source hence the blackbody model parameters could be the result of variation in the count rates between the observations. However, the particular change is seen in the absorber components. The column densities and the temperatures fluctuates between the observations. These could be correlated with the relative strength of the emission profiles but it is hard to make any conclusions without explicit emission models. We considered that the origin of the warm plasma could be

wind/ejecta. It is striking to see the other particular change that is in the velocity of the warm plasma, it is decreasing in time.

CHAPTER 7

V407 LUPI

A classical nova in Lupus is observed during the ongoing All Sky Automated Survey for SuperNovae (ASAS-SN), Chile, on September 24, 2016. The nova V407 Lupi (ASASSN-16kt) was very bright and close to the galactic plane with a probable main sequence secondary. The visual magnitude was around 9.1 mag, and there had not been any previously observed outbursts in its location [82]. V407 Lupi is one of the fastest nova known with $t_2 \leq 2.9$ days, such that it is an indication for the high mass WD, $M_{WD} = 1.1-1.3 M_{\odot}$ [83].

Swift observations are held two days after the visual maximum, but the optical brightness was very high for the UV/Optical Telescope (UVOT), and there was not any X-ray source detection [84, 83]. The closeness of the sun to the field of view to the source prevented any further observation on October 14, 2016. Hence, X-ray observations started on February 21, 2017, 150 days after, during the super soft source phase. The count rate was around 56 counts s^{-1} on day 150, peaked on February 22, 2017, with 61 counts s^{-1} and varied until day 270, the start of the slow decaying phase, but remained above 20 counts s^{-1} [84].

One *XMM-Newton* and one *Chandra* observations are held 168 days and 275 days after visual maximum, respectively [85, 86]. Two periodicities are discovered on day 168 565 s and 3.57 h [87]. The periodicities are considered to be due to the rotation of the WD (565 s) and the orbital period of the binary (3.57 h). The difference of V407 Lupi from the previous sources discussed in earlier chapters is that the spectrum shows weak absorption lines over the SSS continuum between $14-38 \text{ \AA}$. There is also an edge corresponding to the NVI line at 18.6 \AA . Several NLTE and wind-type models are considered for the spectral modeling, but it is argued that the fit obtained by the

blackbody model+edge combination also gives a good approximation [85, 83]. Aydi et al. argued that to be able to observe such a deep absorption edge of NVI, a hot and highly ionized plasma should reside in the binary. They estimated the temperature of the plasma to be around 667 eV [83]. In the same study, it was shown that the absorption lines yield two distinct velocity blue shifts. One was -3200 km s^{-1} and the other one was -400 km s^{-1} . All these arguments suggest that there is a mixture of hot ionized plasma that may be originated from the wind/ejecta. Therefore, V407 Lupi is a good candidate for our model approach.

The distance for V407 Lupi has not been estimated yet. Several possible distance values are considered in the earlier analyses [83], we assumed 10 kpc. The interstellar matter hydrogen column density is given as $n_H=1.56 \times 10^{21} \text{ cm}^{-2}$ by NASA's *heasarc* tool and $n_H=2.62 \times 10^{21} \text{ cm}^{-2}$ by *nhtot*.

7.1 Observations and the data

V407 Lupi observations of *XMM-Newton* were held on March 11, 2017, 168.5 days after the outburst. The total exposure was around 22 ks. The light curves and the spectra were obtained from the archival RGS data. The data were processed with XMM-SAS version 17.0.0 *rgsproc* routine along with the latest calibration files. RGS1 and RGS2 first and second order source and related background spectra were extracted. We obtained flux spectra by using the XMM-SAS *rgsfluxer* routine. RGS2 has a broken chip hence a gap in the data and a low count region during the observation between $24.1\text{-}28.1 \text{ \AA}$ corresponding to the chips3. To eliminate the problem, we combined the spectra with SPEX *rgsfluxcombine*. The first order RGS1 and RGS2 combination could not solve the problem. We tried to apply a filter and finally combined the second orders from both instruments with RGS1 first order. The wavelength range for the extraction was between $4\text{-}40 \text{ \AA}$ with 3600 bins, as it is required by the SPEX version 3.03.00 *rgsfluxcombine* and *rgsfmt*. A binning factor of 2 was used to obtain a statistically correct analysis.

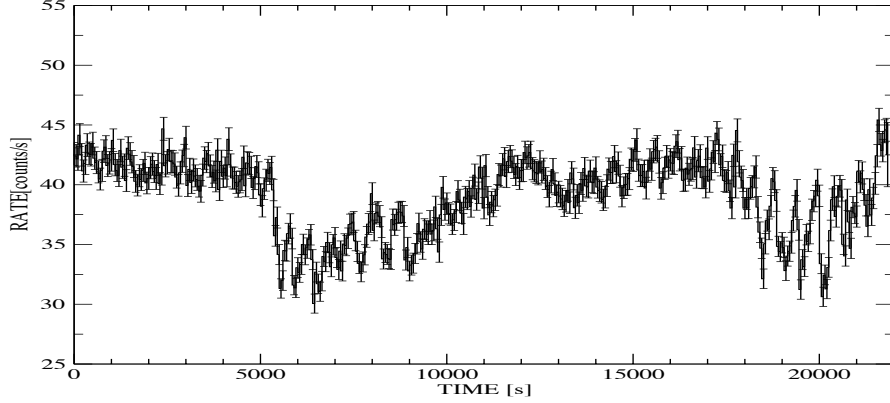


Figure 7.1: *XMM-Newton* RGS1 background subtracted light curve of V407 Lupi 168 days after the outburst. The time bin size is 50 s.

7.2 Analysis and Results

XMM-Newton RGS1 light curve of V407 Lupi is given in figure-7.1. The background subtracted light curve is binned with 50 s. The large 12.6 ks variation, probably due to the orbital period of the binary, is clearly visible in addition to short term periodicity. The mean count rate is around 39 counts s^{-1} .

The continuum spectrum is that of a super soft source between $14\text{-}38 \text{ \AA}$, see Figure-7.2. The emission peak is around 24 \AA . Different than the previous novae, V407 Lup has weak and comparatively narrow absorption lines. The main characteristic is the NVI edge seen at 18.6 \AA . The O K-edge, affected by the dust grain in the region, is present at 22.8 \AA . The lines at 23.5 \AA and 31.3 \AA are OI 1s-2p and NI 1s-2p in their rest wavelengths respectively. These lines are interstellar absorption lines. Ness et al. determined the other observable absorption lines NVII, OVII, NVI that are shifted by -400 km s^{-1} and OVII and NVII 1s-2p lines shifted by -3200 km s^{-1} , details can be found in the reference [85].

We constructed a composite model that includes two hot absorbers. The presence of the NVI edge implies the existence of a probable hot plasma within the binary system as we discussed earlier. The two different velocity shifts can be originated from two

different plasmas. The temperature of the one component should be around or greater than the 667 eV, as suggested by Aydi et al. [83]. Similar to our previous sources, we based our model on the blackbody emission (*bb*) for the continuum. Then, we used two collisionally ionized hot plasma absorber model (*hot*). Finally, we added the interstellar medium absorption by using one *hot* model with low temperature (1eV) for the cold gas and one *amol* for the dust (O K-edge). The final form of the model we used can be summarized as [amol x ISM x hot₂ x hot₁ x bb]. The model fit can be seen in Figure-7.2.

The complexity of the composite model requires some of the parameters to be fixed. We coupled the elemental abundances of the hot plasma components during the analysis. The best fit parameters and the abundances can be seen in Table-7.1. We also analyzed several composite models that are including a different combination of *xabs* model (photoionized warm plasma) and *hot* model. None of the models yielded proper physical results. Additionally, we investigated the presence of the second blackbody component based on the discussions and best fit results of the Aydi et al. [83]. They constructed a model including two plane-parallel, static, NLTE atmosphere model TMAP. The main idea was to use two models is that the atmosphere may not be homogeneous due to the presence of the two hotter emitting regions near the poles, as can be seen in IPs. The analysis of V2491 Cyg yielded a second black body component, and V2491 Cyg is considered to be an IP. V407 Lupi is also an IP candidate, but we could not able to get any conclusive results with the second blackbody component.

7.3 Discussion

In the wavelength range 14-38 Å, the measured absorbed flux by the *XMM-Newton* RGS detector is 1.2×10^{-9} erg cm⁻² s⁻¹. We assumed the distance to the nova is 10 kpc. Hence, we obtained the luminosity as 1.9×10^{39} erg s⁻¹. We discussed the cause of Super-Eddington luminosity in our earlier analysis. The blackbody model assumption gives higher luminosity value and a bloated WD radius. It is also affected by the distance which is currently unknown for this nova. The simple continuum blackbody model has a temperature around 56-58.1 eV ($6.5-6.7 \times 10^5$ K). The normalization is

Table 7.1: *XMM-Newton* RGS best fit parameters of V407 Lupi are in the left. Elemental abundances obtained with a composite model includes two hot absorber are on the right. The abundances are given according to the solar abundances. The errors are calculated with %90 confidence level for one degree of freedom.

Model	Parameters		Abundances	Two hot model
BB	Norm (10^{20}cm^2)	$3.6_{-0.8}^{+10}$		
	kT (eV)	$56.7_{-0.7}^{+1.4}$		
	L (10^{39}erg s^{-1})	1.2		
HOT-1	N_H (10^{22}cm^{-2})	$0.7_{-0.4}^{+0.3}$		
	kT (eV)	483_{-10}^{+205}		
	σ_v (km s^{-1})	13_{-10}^{+10}		
	z_v (km s^{-1})	-3135_{-40}^{+98}		
HOT-2	N_H (10^{22}cm^{-2})	$49.8_{-0.02}^{+0.05}$	C	$0.10_{-0.03}^{+0.07}$
	kT (eV)	1087_{-30}^{+30}	N	$46.72_{-22.45}^{+1.62}$
	σ_v (km s^{-1})	82_{-9}^{+8}	O	$69.88_{-14.69}^{+9.62}$
	z_v (km s^{-1})	-513_{-58}^{+71}	S	$0.15_{-0.02}^{+0.02}$
ISM	N_H (10^{21}cm^{-2})	$2.8_{-0.1}^{+0.2}$	Ar	< 0.02
	kT (eV)	$0.8_{-0.1}^{+0.1}$	Ca	$0.06_{-0.03}^{+0.1}$
	N	$1.3_{-0.2}^{+0.1}$		
	O	$0.6_{-0.1}^{+0.1}$		
AMOL	O_2 (10^{17}cm^{-2})	$1.4_{-0.1}^{+0.1}$		
	χ^2_ν	7.3		
	(d.o.f.)	(1138)		

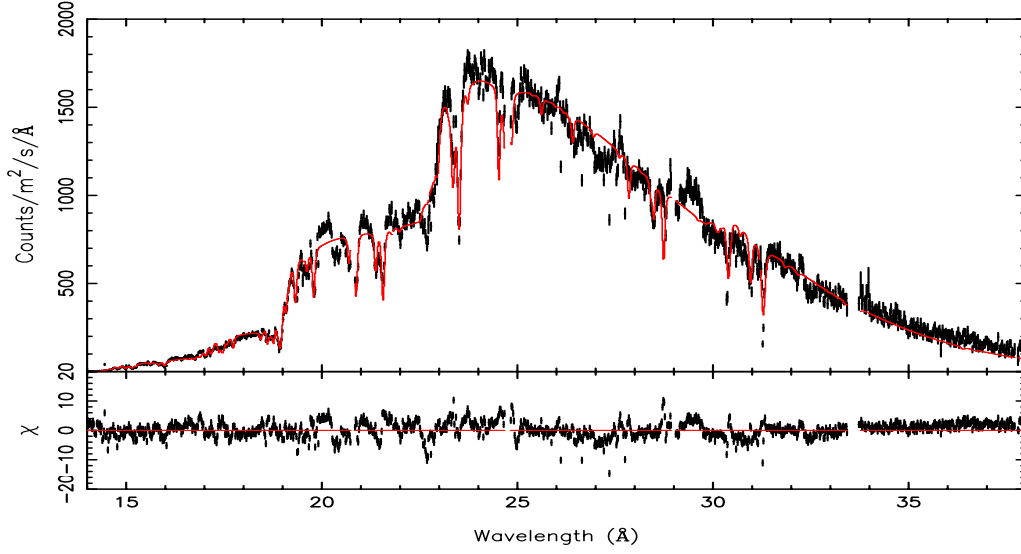


Figure 7.2: V407 Lupi *XMM-Newton* RGS high-resolution spectrum 168 days after the outburst. The red line show the best fitted composite model. The bottom panel shows the deviations from the model.

given as $4\pi R^2$, which yields the effective radius of the blackbody emitting region. The effective radius is then derived as around 5.3×10^9 cm.

The absorber components consist of two collisionally hot plasma models. The hydrogen column densities are in the range $0.03\text{-}0.1 \times 10^{23} \text{ cm}^{-2}$ for the first hot component and $4.93\text{-}5 \times 10^{23} \text{ cm}^{-2}$ for the second hot model. The plasma temperatures are 478-688 eV for the first and 1057-1117 eV for the second hot model. The temperatures of the plasma components are consistent with the expected value for the observation of the NVI line. The values also hint that the shocked ejecta may be the origin of the X-ray emission. The average velocities of the absorbers, z_v , are determined as $3095\text{-}3233 \text{ km s}^{-1}$ and $455\text{-}584 \text{ km s}^{-1}$ for the first and the second hot model respectively. The velocities are in good agreement with the absorption line blueshifts. The velocity of the first hot absorber resembles the wind/ejecta expansion velocities. The absorption lines present in the spectrum are narrower relative to our previous classical nova observed by *XMM-Newton* such as V2491 Cyg and V4743 Sgr. As expected the turbulent velocity broadenings of the absorbers are low, $3\text{-}23 \text{ km s}^{-1}$ for the first hot

model and $73\text{-}90 \text{ km s}^{-1}$ for the second hot model. The differences in the velocities of the absorbers indicate that the locations of these plasmas are different.

We also estimated the elemental abundances of the nova. $C/C_{\odot}=0.07\text{-}0.17$, $N/N_{\odot}=24.27\text{-}43.44$, $O/O_{\odot}=55.19\text{-}79.5$. The carbon is subsolar, N and O are overabundant consistent with the H-burning effects. We also estimated the S, Ar and Ca abundances which are subsolar and affected the overall fitting. The values are given in Table-7.1.

The interstellar matter absorption was modelled by the hot model with low temperature and turbulent velocity values. We can estimate the column density of the interstellar matter, and it is given as $2.7\text{-}3 \times 10^{21} \text{ cm}^{-2}$. The estimation is close to the value given by *nhtot* that is $2.6 \times 10^{21} \text{ cm}^{-2}$. The *XMM-Newton* RGS wavelength range covers the interstellar absorption lines of O and N. Hence, we also estimated the abundances of these elements. We found the ratio as $N/N_{\odot}=1.1\text{-}1.4$, $O/O_{\odot}=0.5\text{-}0.7$. The ISM oxygen abundance is in good agreement with the value obtained by Ness et al. [85] but N is close to the solar abundance. Finally, we estimated the column density of the oxygen molecule O_2 from amol model. The best fits yielded $1.4 \times 10^{17} \text{ cm}^{-2}$.

The best fitted composite model yielded two different plasma models. The χ^2_{ν} is 7.3 for 1138 degrees of freedom. It gives a reasonably good fit for the observed spectrum. We know that the blackbody emission for the continuum is not a well-suited assumption since we are missing some of the photospheric absorption lines. We could not able to model some of the absorption lines seen in the spectrum with a couple of weak emission profiles. This affects the goodness of the overall fitting. However, we could easily model the edge seen in the spectrum and the ISM absorption lines. The results suggest the existence of a complex, highly ionized and hot plasma. The difference in temperatures, column densities, and velocities suggest that the plasma within the system is inhomogenous.

CHAPTER 8

SUMMARY AND COMMENTS

The X-ray observations of cataclysmic variables provide a wide range of information on the physical properties of the binary system. In this work we focused on X-ray sources that are classical nova in outburst. The X-ray phase can last from weeks to years and provides a wealth of information on the effects of nuclear burning near the stellar surface. The X-ray emission can be originated from the photosphere of the WD or from the shocks within the ejecta/winds. Hence, it gives an opportunity to investigate the surrounding plasma and the accretion process of the binary system. The X-ray flux of WD can also easily be absorbed. The ejecta/wind and the interstellar matter absorption leave the imprints of their properties.

The high-resolution X-ray spectrum observations during the outbursts offer the detailed features of all the physical processes of this phase. In this thesis, we have worked on the various *XMM-Newton* and *Chandra* high resolution X-ray archival data of CVs in outburst. We reanalyse the *XMM-Newton* RGS data of V2491 Cyg, V4743 Sgr and V407 Lupi, and *Chandra* HRC-S+LETG spectra of KT Eri. All four of these classical novae are observed during their super soft source phases. Their spectra have complex absorption features. The emission lines are thought to exist but in some cases they are difficult to identified. Especially the spectra of the V4743 Sgr and KT Eri resembled each other, but in the case of KT Eri emission lines are more prominent.

In all analyses, as an alternative to the static or expanding stellar atmospheric models used in the modeling of the X-ray data, composite models including warm and hot absorbers are constructed and investigated in detail. We based our continuum model on a blackbody emission with an addition of collisionally ionized plasma model for

the V2491 Cyg. We discussed the insufficiencies of this model like overestimations of the luminosity parameters or missing photospheric absorptions. We are aware that a better physical approach can be done by using atmospheric models instead of a simple blackbody model. But, we also expressed that to be able to construct the absorption lines from the warm/hot plasma and to see their effects on the spectra we need to make this assumption. The capabilities of the available software packages and models are not sufficient to work with atm models and the plasma components together.

In this thesis, we could able to show the affects of the photoionized or collisionally ionized plasma in motion which can be attributed to wind/ejecta. The absorber components are varied depending on the source but the composite models yielded at least two warm/hot plasma absorbers. The particular change of the column densities and the temperatures of these plasma is seen. The change in such parameters can be caused by rekindled irregular accretion onto the surface of the H-burning WD. They may also be caused by the inhomogenous environment of within the binary system.

The inclusion of the absorption effects of the interstellar matter is crucial. All of the sources we discussed throughout this thesis had have absorption lines in their rest wavelengths. The lines we observed are almost identical in all of them. We know that these lines have interstellar matter origin. Non of the atmospheric models take care of the effect of interstellar matter absorption. Therefore, a proper modelling of the ISM take us closer to the observed spectra.

We have presented the high-resolution X-ray spectral analysis of V2491 Cyg by using the warm and hot absorbers. We investigated two grating observations from *XMM-Newton*. We consider the change in the absorbers in addition to the change in the central emitting source cause the large scale variations seen in the first observation. Therefore, we worked with a selected time intervals corresponding to different count rate regions to investigate the variations. We derived the best fitted composite model for the classical nova V2491 Cyg as [amol x ISM x (cie + (hot₂ x hot₁ x xabs) x bb)]. We also investigated other possible composite models, such as the composite model without the warm absorber.

We obtained the blackbody temperature of 62-85 eV and 78-82 eV from the first and second observation. The *bb* temperatures yield WD mass as 1.15-1.3 M_⊙ consis-

tent with the fast nature of the nova. The effective radii of the emitting region are calculated as $32\text{-}39 \times 10^8$ cm for the era1, $12\text{-}29 \times 10^8$ cm for the era2, era3 and $(2.8\text{-}7.5) \times 10^8$ cm for second observation. The hard X-ray part of the spectra is modeled with collisional equilibrium emission model *cie* for the derivation of the Ne and Mg abundances. The temperature derived from the best fits is around 0.2 keV consistent with shock temperatures for stellar winds.

The composite model consists of two collisionally ionized hot absorber components and one warm absorber. The first hot component hot_1 show equivalent column density of hydrogen in a range $0.5\text{-}3.9 \times 10^{23}$ cm^{-2} for first and $1.4\text{-}8.5 \times 10^{23}$ cm^{-2} for second observation. The absorption drops successively from era1 to era3. In the meanwhile, hot_2 component is $2.0\text{-}16.2 \times 10^{23}$ cm^{-2} and $5.7\text{-}7.2 \times 10^{23}$ cm^{-2} for first and second observation. There does not seem to be a strong variation in the H column density parameters over the four time intervals, only hot_2 components have higher values than hot_1 . The temperatures we obtained, 1.1-3.6 keV (1st obs.), 1.3-2.0 keV (2nd obs.) for hot_1 and 0.5-1.0 keV (1st obs.), 0.4-0.9 keV (2nd obs.) for hot_2 , resemble the temperatures of shocked ejecta. Several selected elemental abundances are $\text{C}/\text{C}_\odot=0.3\text{-}0.5$, $\text{N}/\text{N}_\odot=5\text{-}7$ and $\text{O}/\text{O}_\odot=15\text{-}17$. The overabundance of oxygen implies the existence of an WD with CO core.

The hydrogen column density of the photoionized absorption is $1.3\text{-}4.3 \times 10^{20}$ cm^{-2} for the first and $0.5\text{-}0.7 \times 10^{20}$ cm^{-2} for the second observation. The absorption due to interstellar material is imitated by using the hot model with low temperature, 1 eV and the neutral hydrogen column density derived as about $3.2\text{-}4.2 \times 10^{21}$ cm^{-2} for first and $2.2\text{-}2.7 \times 10^{21}$ cm^{-2} for second observations from the best fits. To be able to fit the lines corresponding to the dust absorption we use *amol* model including the oxygen molecule, carbon monoxide and water ice. We derived the blueshifts seen in the absorbed lines from absorber velocities. The values are in a range, hot_1 , 3097-3812 km s^{-1} and, hot_2 , 2845-3250 km s^{-1} for the first observation. Second observation fits yield velocities, hot_1 , 3517-3586 km s^{-1} and, hot_2 , 2590-2683 km s^{-1} . The warm absorber velocities are initially in a range 750-3113 km s^{-1} , then 10 days after in the range 3009-3254 km s^{-1} . The achieved χ^2_ν values are improved compared to the previous studies in the literature.

We reanalyzed the high-resolution X-ray spectra of V4743 Sgr similar to V2491 Cyg. We investigated one RGS observations from *XMM-Newton*. Besides the large scale variations seen in the spectrum we also investigated if the small scale variations are affected by the changes in the plasma absorbers. Therefore, we worked with twelve selected time intervals corresponding to different count rate regions and peaks and dips from the regions. We derived the best fitted composite model for the classical nova V4743 Sgr as [amol x ISM x hot x xabs₁ x xabs₂ x bb)]. The normalizations for the blackbody in the first time interval are in the range $0.99-1.92 \times 10^{20}$ cm, while in the high-region it is $3.09-4.62 \times 10^{20}$ cm. These give an effective radius of $R=28-39 \times 10^8$ cm and $R=49-60 \times 10^8$ cm. The effective temperatures are in a range of 40-46 eV. Low count rate spectra show similar results with an exception of peak spectra that resembles the valley spectra. The normalization lower bound drops to 0.51×10^{20} cm that gives $R=20 \times 10^8$ cm with an effective temperature 48-45 eV.

The composite model consists of two warm absorbers and one hot absorber. The first resulting warm absorption model has various hydrogen column density N_H values among the spectra. It ranges from $N_{H1} \simeq 0.45-27.88 \times 10^{21}$ cm⁻² in one time interval to $83.3-67.3 \times 10^{21}$ cm⁻² in another. Ionization parameter is $\text{Log}(\xi_1) \simeq 3.4-4.4$ erg cm s⁻¹ and it tends to increase after the first region. The blueshifts are 2727-3486 km s⁻¹. Second warm absorber shows more consistent results and has $N_{H2} \simeq 0.12-0.42 \times 10^{20}$ cm⁻² with ionization parameter $\text{Log}(\xi_2) \simeq 1.3-2.3$ erg cm s⁻¹. The blueshifts are 2190-2669 km s⁻¹. The hot component has $N_H \simeq 1.0-73.8 \times 10^{21}$ cm⁻² and temperature deviating between 271-814 eV except for the high region where the N_H becomes $\simeq 594.2-794.1 \times 10^{21}$ cm⁻² while effective temperature goes to 879-1390 eV. However, the blueshifts 974-2190 km s⁻¹ are consistent among the spectra.

V4743 Sgr shows a typical signature of H-burning with under-abundant carbon $C=0.2-0.9$, and enhanced nitrogen $N=48-71$ and oxygen $O=1.2-14$. Total molecular density of the O₂ drops from $3.8-5.7 \times 10^{17}$ cm⁻² to $2.8-4.5 \times 10^{17}$ cm⁻² in time. When we investigate the spectra throughout the observation one of the warm absorbers $xabs_2$ stays consistent. In the other, the parameters N_H and $\text{Log}(\xi)$ seem to change from the first region to others. Similarly, a change in the hot model hydrogen column density and in the effective temperature can be seen in the high region. The long term variability can be explained with these instabilities in the absorbers.

All of the four *Chandra* HRC-S+LETG observations of KT Eridani is investigated in details for the first time in this thesis. The best obtained model can be given by [amol x ISM x hot x xabs x bb]. The normalisation factor for the blackbody ranges from $0.14 \times 10^{20} \text{ cm}^2$ to $0.42 \times 10^{20} \text{ cm}^2$. The corresponding WD radius can be estimated to be between $1.1 \times 10^9 \text{ cm}$ and $1.8 \times 10^9 \text{ cm}$. The effective temperature of the blackbody is 59.9-60.5 eV on day 71.3, 64.2-81 eV on day 79.3, 80.3-83.3 eV on day 84.6 and 70.6-79.6 eV on day 158.8. The increase in the temperature and a possible shrinking of the WD atmosphere surface may explain the increase in fluxes relative to the first observation.

The best fit model yielded one photoionized warm absorber and one collisionally ionized hot absorber. The column densities for the warm absorber are estimated in the range $0.16\text{-}1.40 \times 10^{24} \text{ cm}^{-2}$. The ionization parameter $\text{Log}\xi$ changes between 2.7 to 3.15. The absorber velocities are calculated as around -2300 km s^{-1} , -2400 km s^{-1} , -1800 km s^{-1} and -1400 km s^{-1} from first to last observation. The absorbers are slowing down in time. The collisionally hot plasma column density is $(2.43 \pm 0.02) \times 10^{24} \text{ cm}^{-2}$ in first observation. It drops to $2.14_{-2.1}^{+2.6} \times 10^{24} \text{ cm}^{-2}$ on day 79.3 and increases to $2.33_{-0.43}^{+0.19} \times 10^{24} \text{ cm}^{-2}$ on day 84.6. Finally, the column density becomes $1.74_{-1.03}^{+0.03} \times 10^{24} \text{ cm}^{-2}$ in the last observation. The plasma temperature is in the range 230-430 eV, and velocities are between 676 km s^{-1} and 874 km s^{-1} .

The hydrogen column density of the ISM fluctuates between $2 \times 10^{20} \text{ cm}^{-2}$ to $6.8 \times 10^{20} \text{ cm}^{-2}$ along the observations. The real difference lies in the column density of O_2 of the dust component where we model the O K-edge. On the day 71.3 and 84.6 the column density of O_2 are $36\text{-}38.8 \times 10^{17} \text{ cm}^{-2}$ and $20.8\text{-}22.1 \times 10^{17} \text{ cm}^{-2}$. On the higher count rate observations on day 79.3 and 158.8 the column density drops to $3.3\text{-}3.5 \times 10^{17} \text{ cm}^{-2}$ and $0.7\text{-}0.9 \times 10^{17} \text{ cm}^{-2}$

The elemental abundance are derived as $\text{C}/\text{C}_\odot \approx 0.01$, $\text{N}/\text{N}_\odot = 0.6\text{-}0.9$ and $\text{O}/\text{O}_\odot = 28.6\text{-}256.8$. The change in the stellar remnant source hence the blackbody model parameters could be the result of variation in the count rates between the observations. However, the particular change is seen in the absorber components. The column densities and the temperatures fluctuates between the observations. These could be correlated with the relative strength of the emission profiles but it is hard to make any conclu-

sions without explicit emission models. We considered that the origin of the warm plasma could be wind/ejecta.

We reanalyzed *XMM-Newton* RGS spectrum of V407 Lupi by using hot plasma absorbers. The NVI absorption edge is observable in the spectrum. The presence of this edge implies the presence of a highly-ionized hot plasma in the system. The analysis provided the best fitted model as [amol x ISM x hot₂ x hot₁ x bb]. The absorber components consist of two collisionally hot plasma models. The simple continuum blackbody model has a temperature around 56-58.1 eV ($6.5-6.7 \times 10^5$ K) and gives the effective radius as around 5.3×10^9 cm. The hydrogen column densities for the hot absorbers are in the range $0.03-0.1 \times 10^{23}$ cm⁻² for the first hot component and $4.93-5 \times 10^{23}$ cm⁻² for the second hot component. The plasma temperatures are 478-688 eV for the first and 1057-1117 eV for the second hot model. The temperatures of the plasma components are consistent with the expected value for the observation of the NVI line. The average velocities of the absorbers, z_v , are determined as 3095-3233 km s⁻¹ and 455-584 km s⁻¹ for the first and the second hot model respectively. The velocity of the first hot absorber resembles the wind/ejecta expansion velocities. We also estimated the elemental abundances of the nova, the carbon is subsolar, N and O are overabundant consistent with the H-burning effects. The interstellar matter column density is derived as $2.7-3 \times 10^{21}$ cm⁻². We provided a reasonably good fit for the observed spectrum. We could easily model the edge seen in the spectrum and the ISM absorption lines. The results suggest the existence of two complex, highly ionized and hot plasmas.

In conclusion, this thesis brings some contribution in understanding of classical novae in the X-ray regime, extensive high-resolution spectral analysis of CNs and provides the detailed analysis of the absorption components in CVs. Most importantly, it reveals the necessity of the consideration of the absorption components, the wind/ejecta, in the spectral modelling.

REFERENCES

- [1] R. C. Smith, “Cataclysmic variables,” *Contemporary Physics*, vol. 47, pp. 363–386, Nov. 2006.
- [2] T. Rauch, M. Orio, R. Gonzales-Riestra, T. Nelson, M. Still, K. Werner, and J. Wilms, “Non-local Thermal Equilibrium Model Atmospheres for the Hottest White Dwarfs: Spectral Analysis of the Compact Component in Nova V4743 Sgr,” *ApJ*, vol. 717, pp. 363–371, July 2010.
- [3] D. R. van Rossum, “A Public Set of Synthetic Spectra from Expanding Atmospheres for X-Ray Novae. I. Solar Abundances,” *ApJ*, vol. 756, p. 43, Sept. 2012.
- [4] P. Szkody and B. T. Gaensicke, “Cataclysmic Variables,” *Journal of the American Association of Variable Star Observers (JAAVSO)*, vol. 40, p. 563, June 2012.
- [5] C. Hellier, *Cataclysmic Variable Stars*. Jan. 2001.
- [6] B. Warner, *Cataclysmic Variable Stars*. Sept. 2003.
- [7] M. F. Bode and A. Evans, *Classical Novae*, vol. 43. 2008.
- [8] F. Jansen, D. Lumb, B. Altieri, J. Clavel, M. Ehle, C. Erd, C. Gabriel, M. Guainazzi, P. Gondoin, R. Much, R. Munoz, M. Santos, N. Schartel, D. Textier, and G. Vacanti, “XMM-Newton observatory. I. The spacecraft and operations,” *A&A*, vol. 365, pp. L1–L6, Jan. 2001.
- [9] A. Talavera, “Optical and UV monitor (OM) on-board XMM-Newton,” *Ap&SS*, vol. 320, pp. 177–180, Apr 2009.
- [10] M. J. L. Turner, A. Abbey, M. Arnaud, M. Balasini, M. Barbera, E. Belsole, P. J. Bennie, J. P. Bernard, G. F. Bignami, M. Boer, U. Briel, I. Butler, C. Cara, C. Chabaud, R. Cole, A. Collura, M. Conte, A. Cros, M. Denby, P. Dhez,

- G. Di Coco, J. Dowson, P. Ferrando, S. Ghizzardi, F. Gianotti, C. V. Goodall, L. Gretton, R. G. Griffiths, O. Hainaut, J. F. Hochedez, A. D. Holland, E. Jourdain, E. Kendziorra, A. Lagostina, R. Laine, N. La Palombara, M. Lortholary, D. Lumb, P. Marty, S. Molendi, C. Pigot, E. Poindron, K. A. Pounds, J. N. Reeves, C. Reppin, R. Rothenflug, P. Salvetat, J. L. Sauvageot, D. Schmitt, S. Sembay, A. D. T. Short, J. Spragg, J. Stephen, L. Strüder, A. Tiengo, M. Trifoglio, J. Trümper, S. Vercellone, L. Vigroux, G. Villa, M. J. Ward, S. Whitehead, and E. Zonca, “The European Photon Imaging Camera on XMM-Newton: The MOS cameras : The MOS cameras,” *A&A*, vol. 365, pp. L27–L35, Jan. 2001.
- [11] L. Strüder, U. Briel, K. Dennerl, R. Hartmann, E. Kendziorra, N. Meidinger, E. Pfeffermann, C. Reppin, B. Aschenbach, W. Bornemann, H. Bräuninger, W. Burkert, M. Elender, M. Freyberg, F. Haberl, G. Hartner, F. Heuschmann, H. Hippmann, E. Kastelic, S. Kemmer, G. Kettenring, W. Kink, N. Krause, S. Müller, A. Oppitz, W. Pietsch, M. Popp, P. Predehl, A. Read, K. H. Stephan, D. Stötter, J. Trümper, P. Holl, J. Kemmer, H. Soltau, R. Stötter, U. Weber, U. Weichert, C. von Zanthier, D. Carathanassis, G. Lutz, R. H. Richter, P. Solc, H. Böttcher, M. Kuster, R. Staubert, A. Abbey, A. Holland, M. Turner, M. Balasini, G. F. Bignami, N. La Palombara, G. Villa, W. Buttler, F. Gianini, R. Lainé, D. Lumb, and P. Dhez, “The European Photon Imaging Camera on XMM-Newton: The pn-CCD camera,” *A&A*, vol. 365, pp. L18–L26, Jan. 2001.
- [12] J. W. den Herder, A. C. Brinkman, S. M. Kahn, G. Branduardi-Raymont, K. Thomsen, H. Aarts, M. Audard, J. V. Bixler, A. J. den Boggende, J. Cottam, T. Decker, L. Dubbeldam, C. Erd, H. Goulooze, M. Güdel, P. Guttridge, C. J. Hailey, K. A. Janabi, J. S. Kaastra, P. A. J. de Korte, B. J. van Leeuwen, C. Mauche, A. J. McCalden, R. Mewe, A. Naber, F. B. Paerels, J. R. Peterson, A. P. Rasmussen, K. Rees, I. Sakelliou, M. Sako, J. Spodek, M. Stern, T. Tamura, J. Tandy, C. P. de Vries, S. Welch, and A. Zehnder, “The Reflection Grating Spectrometer on board XMM-Newton,” *A&A*, vol. 365, pp. L7–L17, Jan. 2001.
- [13] J.-U. Ness, J. P. Osborne, A. Dobrotka, K. L. Page, J. J. Drake, C. Pinto, R. G. Detmers, G. Schwarz, M. F. Bode, A. P. Beardmore, S. Starrfield, M. Hernanz,

- G. Sala, J. Krautter, and C. E. Woodward, “XMM-Newton X-ray and Ultraviolet Observations of the Fast Nova V2491 Cyg during the Supersoft Source Phase,” *ApJ*, vol. 733, p. 70, May 2011.
- [14] M. C. Weisskopf, H. D. Tananbaum, L. P. Van Speybroeck, and S. L. O’Dell, “Chandra X-ray Observatory (CXO): overview,” in *Proc. SPIE (J. E. Truemper and B. Aschenbach, eds.)*, vol. 4012 of *Society of Photo-Optical Instrumentation Engineers (SPIE) Conference Series*, pp. 2–16, Jul 2000.
- [15] S. S. Murray, J. H. Chappell, A. T. Kenter, K. Kobayashi, R. P. Kraft, G. R. Meehan, M. V. Zombeck, G. W. Fraser, J. F. Pearson, J. E. Lees, A. N. Brunton, S. E. Pearce, M. Barbera, A. Collura, and S. Serio, “AXAF High-Resolution Camera (HRC): calibration and recalibration at XRCF and beyond,” in *Proc. SPIE (O. H. Siegmund and M. A. Gummin, eds.)*, vol. 3114 of *Society of Photo-Optical Instrumentation Engineers (SPIE) Conference Series*, pp. 11–25, Oct 1997.
- [16] B. C. Brinkman, T. Gunsing, J. S. Kaastra, R. van der Meer, R. Mewe, F. B. Paerels, T. Raassen, J. van Rooijen, H. W. Braeuninger, V. Burwitz, G. D. Hartner, G. Kettenring, P. Predehl, J. J. Drake, C. O. Johnson, A. T. Kenter, R. P. Kraft, S. S. Murray, P. W. Ratzlaff, and B. J. Wargelin, “Description and performance of the low-energy transmission grating spectrometer on board Chandra,” in *Proc. SPIE (J. E. Truemper and B. Aschenbach, eds.)*, vol. 4012 of *Society of Photo-Optical Instrumentation Engineers (SPIE) Conference Series*, pp. 81–90, Jul 2000.
- [17] A. Fruscione, J. C. McDowell, G. E. Allen, N. S. Brickhouse, D. J. Burke, J. E. Davis, N. Durham, M. Elvis, E. C. Galle, D. E. Harris, D. P. Huenemoerder, J. C. Houck, B. Ishibashi, M. Karovska, F. Nicastro, M. S. Noble, M. A. Nowak, F. A. Primini, A. Siemiginowska, R. K. Smith, and M. Wise, “CIAO: Chandra’s data analysis system,” in *Proc. SPIE*, vol. 6270 of *Society of Photo-Optical Instrumentation Engineers (SPIE) Conference Series*, p. 62701V, Jun 2006.
- [18] J. S. Kaastra, R. Mewe, and H. Nieuwenhuijzen, “SPEX: a new code for spectral analysis of X & UV spectra.,” in *UV and X-ray Spectroscopy of Astrophysical and Laboratory Plasmas (K. Yamashita and T. Watanabe, eds.)*, pp. 411–414, 1996.

- [19] K. Lodders, H. Palme, and H.-P. Gail, “Abundances of the Elements in the Solar System,” *Landolt Börnstein*, p. 712, 2009.
- [20] D. A. Verner and D. G. Yakovlev, “Analytic FITS for partial photoionization cross sections.,” *A&AS*, vol. 109, pp. 125–133, Jan. 1995.
- [21] D. A. Verner, E. M. Verner, and G. J. Ferland, “Atomic Data for Permitted Resonance Lines of Atoms and Ions from H to Si, and S, Ar, Ca, and Fe,” *Atomic Data and Nuclear Data Tables*, vol. 64, p. 1, 1996.
- [22] G. J. Ferland, “Quantitative Spectroscopy of Photoionized Clouds,” *ARA&A*, vol. 41, pp. 517–554, 2003.
- [23] K. A. Arnaud, “XSPEC: The First Ten Years,” in *Astronomical Data Analysis Software and Systems V* (G. H. Jacoby and J. Barnes, eds.), vol. 101 of *Astronomical Society of the Pacific Conference Series*, p. 17, 1996.
- [24] S. Nakano, J. Beize, Z.-W. Jin, X. Gao, H. Yamaoka, K. Haseda, E. Guido, G. Sostero, G. Klingenberg, and K. Kadota, “V2491 Cygni,” *IAU Circ.*, vol. 8934, Apr. 2008.
- [25] N. N. Samus, “V2491 Cygni,” *IAU Circ.*, vol. 8934, Apr. 2008.
- [26] T. Tomov, M. Mikolajewski, E. Ragan, E. Swierczynski, and P. Wychudzki, “Optical observations of the fast nova V2491 Cyg,” *The Astronomer’s Telegram*, vol. 1475, Apr. 2008.
- [27] D. K. Lynch, R. W. Russell, R. J. Rudy, C. E. Woodward, and G. J. Schwarz, “V2491 Cygni,” *IAU Circ.*, vol. 8935, Apr. 2008.
- [28] T. Tomov, M. Mikolajewski, T. Brozek, E. Ragan, E. Swierczynski, P. Wychudzki, and C. Galan, “V2491 Cyg - a possible recurrent nova?,” *The Astronomer’s Telegram*, vol. 1485, Apr. 2008.
- [29] L. A. Helton, C. E. Woodward, K. Vanlandingham, and G. J. Schwarz, “V2491 Cygni,” *Central Bureau Electronic Telegrams*, vol. 1379, May 2008.
- [30] J.-U. Ness, S. Starrfield, R. Gonzalez, E. Kuulkers, J. P. Osborne, K. Page, G. Schwarz, K. M. Vanlandingham, J. J. Drake, M. Hernanz, A. Evans,

- N. Gehrels, J. Krautter, R. D. Gehrz, and C. Woodward, “XMM-Newton RGS observation of V2491 Cyg,” *The Astronomer’s Telegram*, vol. 1561, June 2008.
- [31] Ş. Balman and Ç. Gamsızkan, “Reanalysis of high-resolution XMM-Newton data of V2491 Cygni using models of collisionally ionized hot absorbers,” *A&A*, vol. 598, p. A129, Feb. 2017.
- [32] K. L. Page, J. P. Osborne, P. A. Evans, G. A. Wynn, A. P. Beardmore, R. L. C. Starling, M. F. Bode, A. Ibarra, E. Kuulkers, J.-U. Ness, and G. J. Schwarz, “Swift observations of the X-ray and UV evolution of V2491 Cyg (Nova Cyg 2008 No. 2),” *MNRAS*, vol. 401, pp. 121–130, Jan. 2010.
- [33] U. Munari, A. Siviero, S. Dallaporta, G. Cherini, P. Valisa, and L. Tomasella, “An extensive optical study of V2491 Cyg (Nova Cyg 2008 N.2), from maximum brightness to return to quiescence,” *New A*, vol. 16, pp. 209–219, Apr. 2011.
- [34] A. Ibarra, E. Kuulkers, J. P. Osborne, K. Page, J. U. Ness, R. D. Saxton, W. Baumgartner, V. Beckmann, M. F. Bode, M. Hernanz, K. Mukai, M. Orio, G. Sala, S. Starrfield, and G. A. Wynn, “Pre-nova X-ray observations of V2491 Cygni (Nova Cyg 2008b),” *A&A*, vol. 497, pp. L5–L8, Apr. 2009.
- [35] A. Ibarra, E. Kuulkers, A. Beardmore, P. Evans, K. Mukai, J.-U. Ness, M. Orio, J. P. Osborne, K. L. Page, R. Saxton, S. Starrfield, and J. Tueller, “The persistent, spectral variable pre-nova X-ray source in V2491 Cyg: Swift J194302.1+321913,” *The Astronomer’s Telegram*, vol. 1478, Apr. 2008.
- [36] J.-U. Ness, S. Starrfield, R. Gonzalez, E. Kuulkers, J. P. Osborne, K. Page, G. Schwarz, K. M. Vanlandingham, J. J. Drake, M. Hernanz, G. Sala, A. Evans, N. Gehrels, P. Hauschildt, J. Krautter, R. D. Gehrz, and C. E. Woodward, “Second XMM/RGS spectrum of V2491 Cyg,” *The Astronomer’s Telegram*, vol. 1573, June 2008.
- [37] K. L. Page, J. P. Osborne, P. A. Evans, E. Kuulkers, A. Ibarra, J. J. Drake, J.-U. Ness, A. Beardmore, M. Bode, M. Orio, and G. Schwarz, “Swift X-ray and UV evolution of nova V2491 Cyg 7-34 days after eruption,” *The Astronomer’s Telegram*, vol. 1523, May 2008.

- [38] P. Zemko, K. Mukai, and M. Orio, “Suzaku Observation of the Classical Nova V2491 Cyg in Quiescence.,” *ApJ*, vol. 807, p. 61, July 2015.
- [39] I. Hachisu and M. Kato, “Optical and Supersoft X-Ray Light-Curve Models of Classical Nova V2491 Cygni: A New Clue to the Secondary Maximum,” *ApJ*, vol. 694, pp. L103–L106, Apr. 2009.
- [40] D. Takei, M. Tsujimoto, S. Kitamoto, J.-U. Ness, J. J. Drake, H. Takahashi, and K. Mukai, “Suzaku Detection of Superhard X-Ray Emission from the Classical Nova V2491 Cygni,” *ApJ*, vol. 697, pp. L54–L57, May 2009.
- [41] R. J. Rudy, D. K. Lynch, R. W. Russell, C. E. Woodward, and K. Covey, “V2491 Cygni,” *IAU Circ.*, vol. 8938, Apr. 2008.
- [42] A. Özdönmez, T. Güver, A. Cabrera-Lavers, and T. Ak, “The distances of the Galactic novae,” *MNRAS*, vol. 461, pp. 1177–1201, Sept. 2016.
- [43] B. E. Schaefer, “The distances to Novae as seen by Gaia,” *MNRAS*, vol. 481, pp. 3033–3051, Dec 2018.
- [44] M. J. Darnley, V. A. R. M. Ribeiro, M. F. Bode, and U. Munari, “On the progenitor system of Nova V2491 Cygni,” *A&A*, vol. 530, p. A70, June 2011.
- [45] C. Pinto, J.-U. Ness, F. Verbunt, J. S. Kaastra, E. Costantini, and R. G. Detmers, “A phenomenological model for the X-ray spectrum of nova V2491 Cygni,” *A&A*, vol. 543, p. A134, July 2012.
- [46] R. Willingale, R. L. C. Starling, A. P. Beardmore, N. R. Tanvir, and P. T. O’Brien, “Calibration of X-ray absorption in our Galaxy,” *MNRAS*, vol. 431, pp. 394–404, May 2013.
- [47] K. Werner, S. Dreizler, and T. Rauch, “TMAP: Tübingen NLTE Model-Atmosphere Package,” Dec 2012.
- [48] Ş. Balman, J. Krautter, and H. Ögelman, “The X-Ray Spectral Evolution of Classical Nova V1974 Cygni 1992: A Reanalysis of the ROSAT Data,” *ApJ*, vol. 499, pp. 395–406, May 1998.
- [49] K. Haseda, D. West, H. Yamaoka, and G. Masi, “Another nova in Sagittarius.,” *IAU Circ.*, vol. 7975, Sept. 2002.

- [50] N. N. Samus, “V4743 Sagittarii = Another Nova in Sagittarius,” *IAU Circ.*, vol. 7976, Sept. 2002.
- [51] M. Nielbock and L. Schmidtobreick, “Looking for dust and molecules in Nova V4743 Sagittarii,” *A&A*, vol. 400, pp. L5–L8, Mar. 2003.
- [52] J. U. Ness, S. Starrfield, V. Burwitz, R. Wichmann, P. Hauschildt, J. J. Drake, R. M. Wagner, H. E. Bond, J. Krautter, M. Orio, M. Hernanz, R. D. Gehrz, C. E. Woodward, Y. Butt, K. Mukai, S. Balman, and J. W. Truran, “A Chandra Low Energy Transmission Grating Spectrometer Observation of V4743 Sagittarii: A Supersoft X-Ray Source and a Violently Variable Light Curve,” *ApJ*, vol. 594, pp. L127–L130, Sep 2003.
- [53] T. Kato, M. Fujii, and K. Ayani, “Another Nova in Sagittarius,” *IAU Circ.*, vol. 7975, Sept. 2002.
- [54] T. W. Kang, A. Retter, A. Liu, and M. Richards, “Nova V4743 Sagittarii 2002: An Intermediate Polar Candidate,” *AJ*, vol. 132, pp. 608–613, Aug. 2006.
- [55] J.-U. Ness, S. Starrfield, V. Burwitz, R. Wichmann, P. Hauschildt, J. J. Drake, R. M. Wagner, H. E. Bond, J. Krautter, M. Orio, M. Hernanz, R. D. Gehrz, C. E. Woodward, Y. Butt, K. Mukai, S. Balman, and J. W. Truran, “A Chandra Low Energy Transmission Grating Spectrometer Observation of V4743 Sagittarii: A Supersoft X-Ray Source and a Violently Variable Light Curve,” *ApJ*, vol. 594, pp. L127–L130, Sept. 2003.
- [56] A. Dobrotka and J.-U. Ness, “Counter-evidence against multiple frequency nature of 0.75 mHz oscillation in V4743 Sgr,” *MNRAS*, vol. 467, pp. 4865–4871, June 2017.
- [57] P. Zemko, M. Orio, K. Mukai, A. Bianchini, S. Ciroi, and V. Cracco, “V4743 Sgr, a magnetic nova?,” *MNRAS*, vol. 460, pp. 2744–2751, Aug. 2016.
- [58] E. Leibowitz, M. Orio, R. Gonzalez-Riestra, Y. Lipkin, J.-U. Ness, S. Starrfield, M. Still, and E. Tepedelenlioglu, “Variability and multiperiodic oscillations in the X-ray light curve of the classical nova V4743 Sgr,” *MNRAS*, vol. 371, pp. 424–430, Sept. 2006.

- [59] A. Dobrotka and J.-U. Ness, “Multifrequency nature of the 0.75 mHz feature in the X-ray light curves of the nova V4743 Sgr,” *MNRAS*, vol. 405, pp. 2668–2682, July 2010.
- [60] Ş. Balman and Y. Pekön, “High Resolution XMM-Newton Data of Nova Outbursts using Warm & Hot Absorber Models,” in *Binary Paths to Type Ia Supernovae Explosions* (R. Di Stefano, M. Orío, and M. Moe, eds.), vol. 281 of *IAU Symposium*, pp. 124–125, Jan. 2013.
- [61] K. Itagaki, “Possible Nova in Eridanus,” *Central Bureau Electronic Telegrams*, vol. 2050, Nov. 2009.
- [62] H. Yamaoka, K. Itagaki, E. Guido, G. Sostero, H. Maehara, M. Fujii, A. Arai, M. Isogai, K. Imamura, R. J. Rudy, T. R. Prater, R. W. Russell, R. C. Puetter, R. B. Perry, and E. V. Kazarovets, “KT Eridani = Nova Eridani 2009,” *IAU Circ.*, vol. 9098, Dec. 2009.
- [63] M. F. Bode, J. P. Osborne, K. L. Page, A. P. Beardmore, F. M. Walter, J.-U. Ness, G. Schwarz, S. Starrfield, E. Kuulkers, T. J. O’Brien, S. Balman, M. J. Darnley, A. Evans, P. Evans, S. P. S. Eyres, and J. Krautter, “Emergence of a Bright and Highly Variable Super-soft Source Phase in Nova KT Eri (2009),” *The Astronomer’s Telegram*, vol. 2392, Jan. 2010.
- [64] L. W. Hung, W. P. Chen, and F. M. Walter, “Optical and X-ray Observations of the Nova KT Eridani 2009,” in *9th Pacific Rim Conference on Stellar Astrophysics* (S. Qain, K. Leung, L. Zhu, and S. Kwok, eds.), vol. 451 of *Astronomical Society of the Pacific Conference Series*, p. 271, Dec. 2011.
- [65] R. Hounsell, M. F. Bode, P. Hick, A. Buffington, B. Jackson, J. Clover, A. W. Shafter, M. J. Darnley, A. Evans, and T. J. O’Brien, “The outburst light curve of Nova KT Eridani from Solar Mass Ejection Imager (SMEI) observations,” *The Astronomer’s Telegram*, vol. 2558, p. 1, Apr 2010.
- [66] H. Maehara, “Nova eridani 2009.” *Central Bureau Electronic Telegrams*, vol. 2053, p. 2, Nov 2009.
- [67] R. J. Rudy, T. R. Prater, R. W. Russell, R. C. Puetter, and R. B. Perry, “Nova Eridani 2009,” *Central Bureau Electronic Telegrams*, vol. 2055, p. 1, Nov 2009.

- [68] R. Jurdana-Šepić, V. A. R. M. Ribeiro, M. J. Darnley, U. Munari, and M. F. Bode, “Historical light curve and search for previous outbursts of Nova KT Eridani (2009),” *A&A*, vol. 537, p. A34, Jan 2012.
- [69] A. Özdönmez, E. Ege, T. Güver, and T. Ak, “A new catalogue of Galactic novae: investigation of the MMRD relation and spatial distribution,” *MNRAS*, vol. 476, pp. 4162–4186, May 2018.
- [70] W. M. Wolf, R. H. D. Townsend, and L. Bildsten, “Nonradial Pulsations in Post-outburst Novae,” *ApJ*, vol. 855, p. 127, Mar 2018.
- [71] A. Pagnotta and B. E. Schaefer, “Identifying and Quantifying Recurrent Novae Masquerading as Classical Novae,” *ApJ*, vol. 788, p. 164, Jun 2014.
- [72] P. Zemko, S. Ciroi, M. Orio, A. Odendaal, S. Shugarov, E. Barsukova, A. Bianchini, V. Cracco, M. Gabdeev, and V. Goranskij, “Optical observations of ‘hot’ novae returning to quiescence,” *MNRAS*, vol. 480, pp. 4489–4504, Nov 2018.
- [73] J.-U. Ness, J. J. Drake, S. Starrfield, M. Bode, K. Page, A. Beardmore, J. P. Osborne, and G. Schwarz, “A Chandra High-Resolution X-ray spectrum of KT Eri,” *The Astronomer’s Telegram*, vol. 2418, Feb. 2010.
- [74] A. P. Beardmore, S. Balman, J. P. Osborne, K. L. Page, M. F. Bode, J. J. Drake, J. U. Ness, M. Orio, and S. Starrfield, “Large amplitude variability and detection of a 35 sec modulation of the soft X-ray flux of nova KT Eri by Swift,” *The Astronomer’s Telegram*, vol. 2423, p. 1, Feb 2010.
- [75] G. J. Schwarz, J.-U. Ness, J. P. Osborne, K. L. Page, P. A. Evans, A. P. Beardmore, F. M. Walter, L. A. Helton, C. E. Woodward, and M. Bode, “Swift X-Ray Observations of Classical Novae. II. The Super Soft Source Sample,” *ApJS*, vol. 197, p. 31, Dec 2011.
- [76] J. U. Ness, A. P. Beardmore, J. P. Osborne, E. Kuulkers, M. Henze, A. L. Piro, J. J. Drake, A. Dobrotka, G. Schwarz, and S. Starrfield, “Short-period X-ray oscillations in super-soft novae and persistent super-soft sources,” *A&A*, vol. 578, p. A39, Jun 2015.
- [77] J. Osborne, K. Page, A. Beardmore, M. Goad, M. Bode, T. O’Brien, G. Schwarz, S. Starrfield, J.-U. Ness, J. Krautter, J. Drake, A. Evans, and S. P. S. Eyres, “RS

Oph: Swift X-ray observations find short period modulation and highly variable low energy flux,” *The Astronomer’s Telegram*, vol. 770, Mar. 2006.

- [78] E. Ragan, T. Brozek, K. Suchomska, A. Skalbania, P. Konorski, C. Galan, E. Swierczynski, T. Tomov, M. Mikolajewski, and P. Wychudzki, “Optical observations of KT Eri = Nova Eridani 2009,” *The Astronomer’s Telegram*, vol. 2327, Dec. 2009.
- [79] J. U. Ness, J. P. Osborne, M. Henze, A. Dobrotka, J. J. Drake, V. A. R. M. Ribeiro, S. Starrfield, E. Kuulkers, E. Behar, M. Hernanz, G. Schwarz, K. L. Page, A. P. Beardmore, and M. F. Bode, “Obscuration effects in super-soft-source X-ray spectra,” *A&A*, vol. 559, p. A50, Nov 2013.
- [80] M. Orío, J. U. Ness, A. Dobrotka, E. Gatzuz, N. Ospina, E. Aydi, E. Behar, D. A. H. Buckley, S. Ciroi, M. Della Valle, M. Hernanz, M. Henze, J. P. Osborne, K. L. Page, T. Rauch, G. Sala, S. Starrfield, R. E. Williams, C. E. Woodward, and P. Zemko, “What We Learn from the X-Ray Grating Spectra of Nova SMC 2016,” *ApJ*, vol. 862, p. 164, Aug 2018.
- [81] E. Gatzuz, J. García, T. R. Kallman, C. Mendoza, and T. W. Gorczyca, “ISMabs: A Comprehensive X-Ray Absorption Model for the Interstellar Medium,” *ApJ*, vol. 800, p. 29, Feb 2015.
- [82] K. Z. Stanek, C. S. Kochanek, J. S. Brown, T. W. S. Holoién, J. Shields, B. J. Shappee, J. L. Prieto, D. Bersier, S. Dong, and S. Bose, “ASAS-SN Discovery of A Likely Galactic Nova ASASSN-16kt at $V=9.1$,” *The Astronomer’s Telegram*, vol. 9538, p. 1, Sep 2016.
- [83] E. Aydi, M. Orío, A. P. Beardmore, J. U. Ness, K. L. Page, N. P. M. Kuin, F. M. Walter, D. A. H. Buckley, S. Mohamed, and P. Whitelock, “Multiwavelength observations of V407 Lupi (ASASSN-16kt) - a very fast nova erupting in an intermediate polar,” *MNRAS*, vol. 480, pp. 572–609, Oct 2018.
- [84] A. P. Beardmore, K. L. Page, J. P. Osborne, and M. Orío, “Swift observations of nova V407 Lup: detection of a UV period at 1.1 or 3.6 hours,” *The Astronomer’s Telegram*, vol. 10632, p. 1, Aug 2017.

- [85] J.-U. Ness, S. Starrfield, C. E. Woodward, P. Kuin, K. Page, A. Beardmore, J. Osborne, G. Sala, M. Hernanz, and M. Orio, “XMM-Newton X-ray spectra of V407 Lup (Nova Lup 2016),” *The Astronomer’s Telegram*, vol. 10756, p. 1, Sep 2017.
- [86] M. Orio, A. Beardmore, K. Page, and J. Osborne, “Nova Lup 2016 during the X-ray decay phase,” *The Astronomer’s Telegram*, vol. 10722, p. 1, Sep 2017.
- [87] A. Beardmore, A. Dobrotka, J.-U. Ness, M. Orio, J. Osborne, and K. Page, “Detection of a 9.4 min periodicity in the XMM-Newton and Chandra X-ray light curves of V407 Lup (Nova Lup 2016),” *The Astronomer’s Telegram*, vol. 10749, p. 1, Sep 2017.

CURRICULUM VITAE

PERSONAL INFORMATION

Surname, Name: Gamsızkan, Çiğdem

Nationality: Turkish (TC)

Date and Place of Birth: 09.08.1987, İstanbul

Marital Status: Married

EDUCATION

Degree	Institution	Year of Graduation
Ph.D.	METU, Physics	2019
M.S.	University of Innsbruck, Astromundus	2012
B.S.	METU, Physics	2010
High School	Vefa Anadolu Lisesi	2005

PROFESSIONAL EXPERIENCE

Year	Place	Enrollment
Duration 1	Institute/Company 1	Role/Position/Experience 1
2009-2010	METU	Student Assistant

PUBLICATIONS

Balman, Ş., & Gamsızkan, Ç. 2017, A&A, 598, A129